The Development and Analysis of Model Systems to Probe Proton-Coupled Electron Transfer in Ribonucleotide Reductase Ia of E. Coli

The Development and Analysis of Model Systems to Probe Proton-Coupled Electron Transfer in Ribonucleotide Reductase Ia of *E. coli*

A dissertation presented

by

Bon Jun Koo

to

The Department of Chemistry and Chemical Biology

in partial fulfillment of the requirements

for the degree of

Doctor of Philosophy

in the subject of

Chemistry

Harvard University

Cambridge, Massachusetts

May 2016

Dissertation Advisor: Professor Daniel G. Nocera Bon Jun Koo

The Development and Analysis of Model Systems to Probe Proton-Coupled Electron Transfer in Ribonucleotide Reductase Ia of *E. Coli*

Abstract

Proton-coupled electron transfer (PCET) combines proton transfer with electron transfer to bypass high-energy intermediates. The ribonucleotide reductase (RNR) family of enzymes catalyzes the conversion of ribonucleotides to deoxynucleotides using amino acid radicals. The enzyme contains an efficient PCET pathway that transfers an electron and proton over a 35 Å distance across two subunits, the longest PCET pathway known in biology. The enzyme functions with very high fidelity, performing $>10^5$ turnovers before radical loss.

This thesis explores PCET in model systems to understand the radical transport pathway in *E. coli* RNR type Ia. First, amino acid radical generation was explored by laser spectroscopy. Small molecule systems, where photooxidants were appended with amino acids, provide a platform for probing both the pH and driving force dependence of PCET. Analysis of the emission kinetics of these systems indicate that amino acid radicals were generated by sequential electron and proton transfers as a result of the strong driving force of the photooxidant. Next, the dyad model with cofacial aromatic units was developed to investigate the PCET radical transport mechanism between two adjacent amino acids. Inspired by the unique redox cooperativity observed in Y_{730}-Y_{731} tyrosine dyads at the $\alpha_2\beta_2$ interface of RNR, electrochemical and computational approaches were used to probe the correlation between the structural and redox properties of the dyad model. Using electrochemical and computational analysis, it was determined that the presence of two phenol units in the dyad lowered the reduction potential by ~ 60 mV. This result

demonstrates that the tyrosine dyad behaves as a discrete redox unit, consistent with the observed radical transport pathway observed in RNR. Finally, the bidirectional PCET pathway in the β_2 subunit of RNR (Y_{122}-W_{48}-Y_{356}) was modeled using a polyproline-based peptide. The long-distance electron transfer between tyrosine analogs and tryptophan was investigated by pulse radiolysis to determine the radical transfer rate in these peptide models. Since efficient electron transfer was observed between tetrafluorotyrosine and tryptophan at a 10 Å distance in the model system, Y_{122} and W_{48} at a 7.4 Å distance in RNR likely serve as the radical transport pathway in a bidirectional, sequential electron and proton transfer mechanism.

Table of Contents

List of Figures

List of Schemes

List of Tables

Acknowledgements

First of all, I thank my advisor, **professor Daniel Nocera** for all the opportunities you have given me. The 6 years in Nocera Group will remain as the most memorable experience of my life. “Make an island of your chemistry and keep it as a refuge from all other STUFFs of your life.” I shall apply this piece of advice you gave me to the other aspects of my life.

I express my gratitude to **professor JoAnne Stubbe**. In the challenging turns of my research, you helped me connected with other collaborators. I appreciate your continued interest in my development as a person and a scientist. **Professor Daniel Kahne** helped me to contextualize my works in meaningful way. I also enjoyed learning from you during my independent proposals. I thank **Dr. James F. Wishart** from the Brookhaven National Laboratory for his kind mentorship.

Hyangsoo and **Grace**, you are my sisters. You know my ups and downs and I know yours. Hyangsoo, you are a regular victim of my mischiefs. I loved your sincere surprises and friendship. Grace, I feel that you have a scanner for my emotions and thoughts. I can write a few hundred pages in honor of our memories here in Cambridge: Yeal-nyou-moon, “Bon Jun alphabet achievement list”, “One Naan for me”, and etc. I am so happy that I met friends I shall cherish for my entire life. Hyangsoo and Grace, thank you and thank you.

Mike, I thank you for helping me in both science and life issues. I respect your integrity so when you need to get some investment for your start-up, shut up and take my money. **Chris**, we should continue our friendship beyond graduate school. I still have so much Korean phrases to teach you and you have so much English to teach my mom and me. **Dilek**. I thank you for taking care of me. You provided me more than I could ever imagine receiving from colleagues or friends. **Nancy**, you are an endearing friend who brightened my daily life in the lab. **Pat** and **Arturo** helped me to get settled in and get started with my research. **Bryce**, and **Andrew M**. thank you for all scientific discussions and all weekend hangouts. You two are my favorite white American Pchemists. I appreciate **Casandra**, **Graham**, **Kwabena**, **Lisa**, **Guillaume**, **Manos**, **Andrew U**., and **Changhoon** for being wonderful colleagues and friends.

Woonju, **Doori**, **Soyean**, **Chiheon**, **Seungwoo**, **Seungjun**, **Sarah**, **Jee Soo**, **Nicole**, and **Uhi Rinn** were kind friends who made Cambridge feel like home for me. **Janine**, **Kathleen**, and **Annie** supported me from close and far.

Travis, I thank you for always accommodating me, my schedule, my whims, my ups and downs, my tantrum and even my nonsenses. Your kindness and calmness helped me get through challenges and made me happy. My little sister **Bon Yoon**, your stay with me during the first year of MIT was my favorite time. I spent last 10 years in USA but my heart was always with you. I am so happy that we both achieved important milestones in the same year. **My grandma**, I always wanted to show you that your first granddaughter is worthy of your love. I will continue to try to be that person. **Dad**. I will continue my journey to be a strong, happy and kind person as you wish. Thank you for believing in me. **Mom**. I can do no wrong in your eyes. I cannot imagine being here without your unconditional support and love. I want to be strong and happy so that we can share more happy moments. I love you.

Chapter 1 –

Introduction: Proton-Coupled Electron Transfer

1.1 Proton-Coupled Electron Transfer

Proton-coupled electron transfer combines proton transfer (PT) with electron transfer (ET) to effect numerous charge transfer and bond-making/breaking reactions. In the absence of this coupling, highly unfavorable intermediates and transition states are confronted.[1,2] The resting mass of a proton is ~ 2000 times heavier than the resting mass of electron, and thus these two constituents exhibit remarkably different quantum character in chemical reactions. The clearest example of this dichotomy lies in the predicted (and observable) proton tunneling wavelength, which is ~ 40 times shorter than that of the electron at fixed energy. For this reason, PT is confined to a much shorter distance as compared to ET. The extent of coupling between these two vastly different entities is influenced by various parameters: driving force of the redox couple, the donor-acceptor distance, solvent polarization, tunneling matrix element among other factors. However, a complete understanding of the mechanisms of coupling via these parameters and the ubiquity of these coupled processes in chemistry is still not understood. As a result, the fundamental process of proton-coupled electron transfer (PCET) has been and continues to be investigated with diverse approaches and methods.

1.1.1 Classification of PCET Mechanisms

PCET as a mechanism encompasses a series of "sub-mechanisms" for coupling ET and PT. Figure 1.1 displays a commonly used mechanistic formulation of PCET, termed a "square scheme". The initial and final states of PCET are represented on top left and bottom right, respectively. PCET involving intermediates on the bottom left and top right corners of each square represent a stepwise mechanism, either proton transfer followed by electron transfer (PTET) or electron transfer followed by proton transfer (ETPT). In certain cases, no intermediates are in-

volved and a single transition state describes the PCET event. This mechanism is represented as the diagonal of the square scheme and is termed concerted proton-electron transfer (CPET).

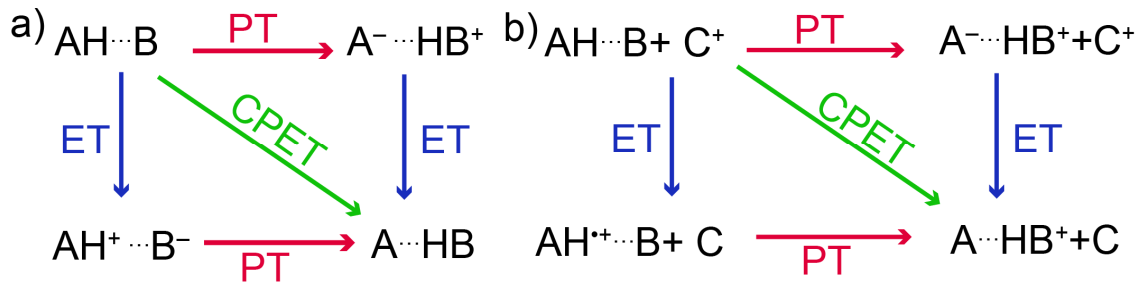

Figure 1.1 PCET. The sides of each square represent the stepwise mechanism of ETPT (down then right) or PTET (right then down) where proton and electron transfer steps occur sequentially. The concerted pathway is CPET and depicted along the diagonal by the green arrow. a) Unidirectional or collinear PCET: proton and electron transfer occur between a single donor-acceptor pair. CPET is equivalent to hydrogen atom transfer. b) Orthogonal or bidirectional PCET: proton and electron transfer via distinct donor-acceptor pairs.[1,3]

The directionality of PCET is defined by the identity of proton and/or electron acceptor and can be categorized as unidirectional (collinear) and bidirectional (orthogonal) PCET. Unidirectional PCET occurs when both proton and electron transfer are involved with the same donor-acceptor pair. Bidirectional PCET involves electron and protons originating from different donor-acceptor pairs. As stated above, the significantly different masses of the proton and electron affect the distance over which the electron and proton can tunnel: proton tunneling is restricted to very short distance (< 0.5 Å) whereas electrons can tunnel in excess of 10 – 20 Å. Therefore, PCET processes over long distances are most easily accomplished by bidirectional PCET. PCET events over short distances can proceed by either bidirectional or unidirectional PCET.

1.1.2 PCET Theory

The theory of electron transfer (ET) by Marcus[4,5] and others[6,7] has equipped chemists with the ability to relate the change in reaction Gibbs free energy to the kinetic rate of ET. Equa-

tion 1.1 represents the modified Marcus-Levich equation for ET reactions with weak electronic coupling:

$$k_{ET} = H_{AB}^2 \sqrt{\frac{\pi}{\hbar^2 \lambda k_B T}} \exp\left(\frac{-(\lambda+\Delta G^0)^2}{4\lambda k_B T}\right) \quad \text{(Eq. 1.1)}$$

where H_{AB} is the donor-acceptor electronic coupling, ΔG^0 is the free energy of the ET reaction, and λ is the reorganization energy with contributions from both the reactant/product molecules (inner sphere) and solvent (outer sphere).

Marcus theory of ET establishes a platform for treating the more complicated chemical phenomenon PCET.[8,9] Nocera, Cukier, Hammes-Schiffer and others have developed PCET theories.[2,8,9,10] Equation 1.2 represents the kinetic description of PCET in the limit of electronically adiabatic PT and electronically nonadiabatic ET:

$$k_{ET} = \frac{2\pi}{\hbar} \sum_\mu P_{I\mu} \sum_\nu V_{\mu\nu}^2 \, (4\pi\lambda_{\mu\nu} k_B T)^{-1/2} \exp\left(\frac{-(\lambda_{\mu\nu}+\Delta G_{\mu\nu}^0)^2}{4\lambda k_B T}\right) \quad \text{(Eq. 1.2)}$$

where Σ_μ and Σ_ν indicate a sum over vibrational states associated with the two states (before PCET and after PCET) and the other terms are similar to those in Eq. 1.1 but include the contributions arising from both the proton and electron. $V_{\mu\nu}$ is vibronic electronic coupling that is different for each coupled-vibrational mode of the reactant state and of the product state. $P_{1\mu}$ is the Boltzmann factor for the reactant state. As with ET, the reaction coordinate is defined by potential energy surfaces as a pair of paraboloids but they are functions of the solvent response to changes in both electron and proton positions. The detailed derivation of PCET theory is available in multiple reviews.[8–10]

1.1.3 Application of PCET

The mechanistic understanding of PCET is crucial for a variety of applications ranging from solar fuels production and storage by artificial photosynthesis to radical enzymology. For

the former, PCET is the core process of capturing sunlight to drive fuel formation as shown in the following equations (Eq. 1.3–1.5).[11]

(Eq. 1.3) $2H_2O \rightarrow O_2 + 4H^+ + 4e^-$

(Eq. 1.4) $2H^+ + 2e^- \rightarrow H_2$

(Eq. 1.5) $CO_2 + 2H^+ + 2e^- \rightarrow HCOOH$

Photosystem II (PSII) uses sunlight and water to drive NADPH and ATP production with O_2 released as by-product. NADPH and ATP are later used to capture CO_2 and fix it into carbohydrates.[12] The so-called Y_Z (tyrosine) radical of PSII is a paradigmatic example of an amino acid managing bidirectional PCET in biology. Y_Z donates an electron to the primary electron donor ($P680^+$) and is postulated to release its phenolic proton upon oxidation to a nearby base H_{190} (histidine). In this regard, PSII exemplifies the importance of PCET in bioenergy conversion.

PCET is also a critical component of amino acid radical generation and transport through various protein matrices[3,13] and in the activation of numerous substrate bonds at enzyme active sites. Figure 1.2 lists some of the many enzymes that operate by mechanisms involving radicals. Most of these enzymes utilize PCET to manage radicals.

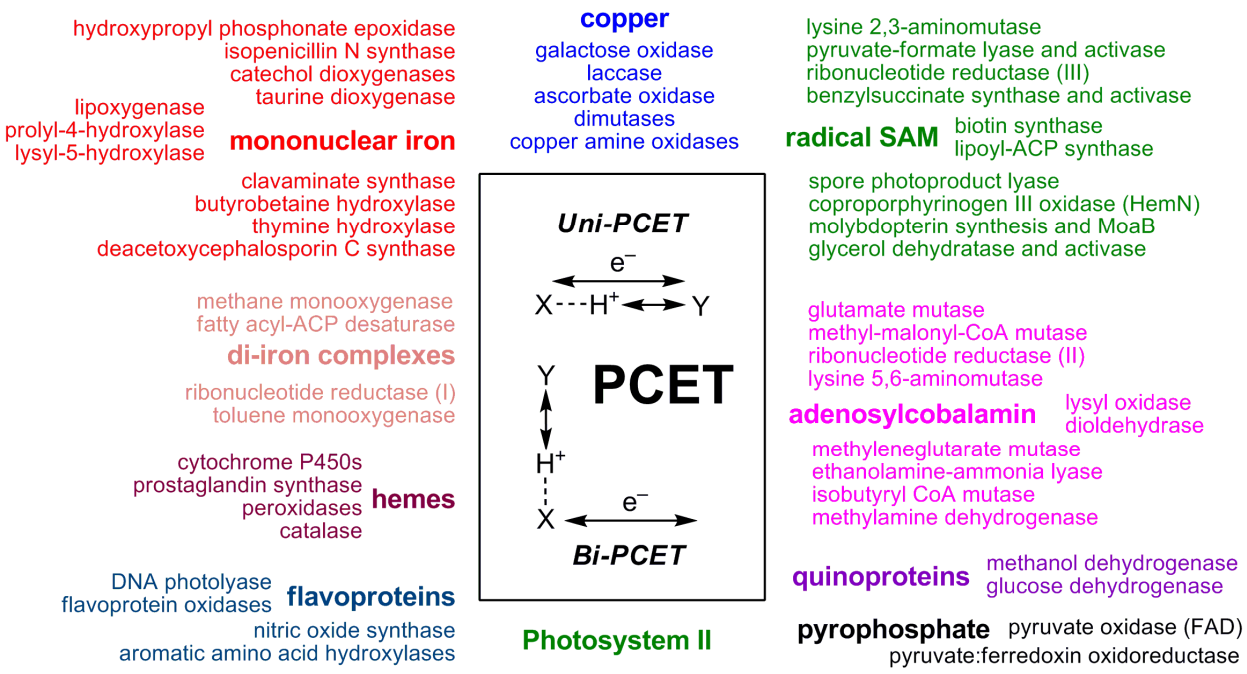

Figure 1.2 PCET in biology occurs by unidirectional or bidirectional transfer of the proton and electron. Various enzymes that utilize radical mechanisms to activate substrate and/or transport radicals are shown above. The figure is adapted from reference 13.

There are a wide variety of enzymes that utilize PCET for their catalysis. Heme oxidases,[14,15] copper-based oxidases,[16,17] reductases,[18,19,20] flavin and pyrroloquinoline-dependent enzyme,[21,22] and non-heme iron proteins[23,24] are understood to utilize PCET for their substrate activation. A mechanistic understanding of biological PCET has significance in therapeutic context as many essential metabolic steps rely on enzymes that utilize PCET to perform primary catalytic reactions.[13]

1.1.4 Biological PCET and Amino Acids Radicals

The generation and transport of amino acid radicals often occurs by utilizing PCET. Glycine, tyrosine, tryptophan and cysteine are the most prevalent amino acid radicals in enzymes (Figure 1.3b).[26]

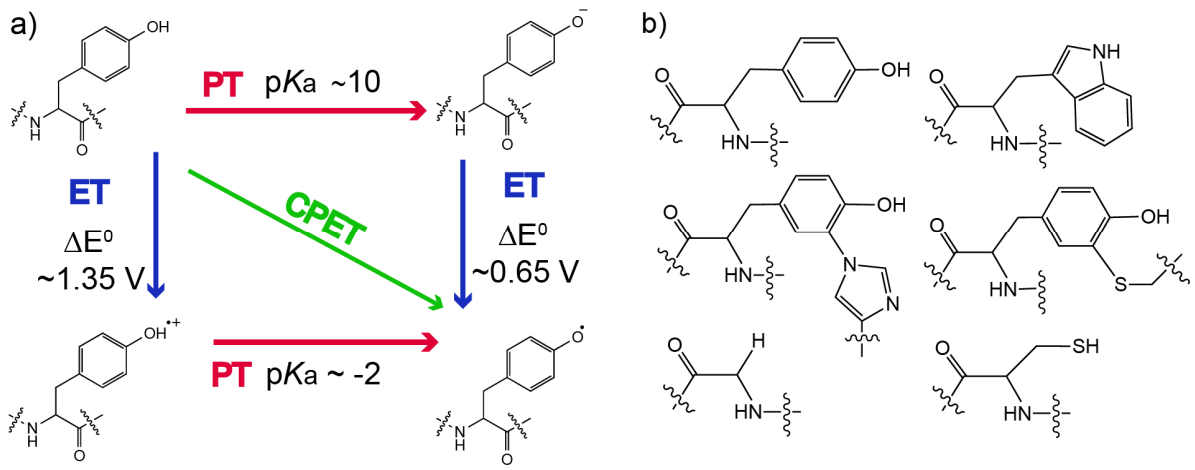

Figure 1.3 a) Square scheme of tyrosine in aqueous solutions.[25] b) Common amino acid radicals[26] : tyrosine, tryptophan, glycine, cysteine, and cross-linked amino acids.

At physiological pH and temperature, the stepwise removal of a proton or an electron from redox active amino acids produces higher energy intermediates as opposed to when both electron and proton are removed (Figure 1.3a). Tyrosyl radical generation via PTET requires the generation of tyrosinate. The pK_a of tyrosine (~10) is outside the biologically relevant pH range of 6 ~ 8; therefore PTET is not a competent pathway except in special cases where fast ET follows slow PT (at pH 8, ~1 % of tyrosine exists as tyrosinate at steady state) or where protein environment perturbs the pK_a significantly. Conversely, the ETPT stepwise pathway generates the tyrosyl radical cation in a highly endergonic process as the E^0 ($YOH^{+\bullet}$/YOH) reduction potential is ~1.35 V vs. NHE. Direct tyrosyl radical generation proceeds via CPET pathway by utilizing a proton acceptor to modulate the reduction potential of tyrosine. In many enzymes, catalysis is facilitated by stabilizing the charges in the transition state through the use of acid or base to donate or accept protons, respectively.[26]

Table 1.1 The characteristics of tyrosyl and tryptophanyl radicals. Data were collected from references 26–30.

Amino Acid		E^0	λ_{max}(nm)	ε_{max}($M^{-1}cm^{-1}$)	pK_a	g_x
Tyrosine	($Y^\bullet$)	0.94[a]	410	2750 ± 200	9.9	2.0067
2,3,5,6-F_4Y	($F_4Y^\bullet$)	E_p (pH 7) 0.97[c]	420		7.8	note[f]
2,3-F_2Y	($F_2Y^\bullet$)	E_p (pH 7) 0.81[c]	412		5.6	note[f]
Tryptophan	($W^\bullet$)	1.05 [c]	510	1800 ± 50	17	2.0041[e]
	($WH^{+\bullet}$)	1.15 (pH 3)[a,b]	580	3000 ± 150	4.3	
Cysteine	($C^\bullet$)	1.33[a]	300-330	400-1200	8.5	2.2441
Glycine	($G^\bullet$)	1.22 [a,d]			-	2.0042

[a] E^0 standard reduction potential measured by pulse radiolysis, [b] pH 3 [c] E_p electrochemical peak potential. [d] pH 10.5 [e] reference 30: in RNR [f] high-field EPR resolves fluorotyrosyl radicals from tyrosyl radical, reference 31.

The physical characteristics of common amino acid radicals are summarized in Table 1.1. The chemical properties (redox potentials and pK_a) of amino acid radicals have been characterized both within and outside of the protein matrix and some properties are expected to differ significantly. Optical absorption and electron paramagnetic resonance features are useful handles for monitoring the kinetics of amino acid radicals. However, it is difficult to identify the specific residues of a radical signal since proteins often contain multiple numbers of an amino acid. For this reason, unnatural amino acids can provide a good tool to identify the location of the radical within the protein. For example, the site-specific incorporation of fluorotyrosines minimally perturbs the protein structure and subunit interactions and accordingly is useful to distinguish the tyrosyl radical of interest from other tyrosines and from the off-pathway radicals. Also, unnatural amino acids can be used to tune parameters important to PCET (pK_a, driving force, hydrogen bonding) thus allowing the PCET kinetics of radical generation, transport and catalysis to be uncovered.

1.2 *Escherichia coli* Class Ia Ribonucleotide Reductase

1.2.1 Structure and Function of Ribonucleotide Reductases

Ribonucleotide reductases (RNRs) catalyze the substitution of the 2′-hydroxyl group of a ribonucleotide (RNR building blocks: NDPs) to a hydrogen to make a deoxynucleotide (DNA building blocks: dNDPs) by utilizing amino acid radicals (Figure 1.4).[20] RNRs play an essential role in maintaining an appropriate balance of all four substituents of DNA (A, T, G and C) in cells and thus are necessarily found in all living organisms. The identity of radical cofactor divides RNRs into three classes: Class III RNRs contain an O_2-sensitive glycyl radical cofactor, class II RNRs use an adenosylcobalamin metallocofactor. And class I RNRs are subdivided into classes Ia, b and c, where a and b contain $Fe^{III}_2(\mu\text{–}O)$ and $Mn^{III}_2(\mu\text{–}O)$ metallocofactors along with a tyrosyl radical and class Ic RNRs contain Mn^{IV}/Fe^{III} cofactor without a tyrosyl radical [3,26]

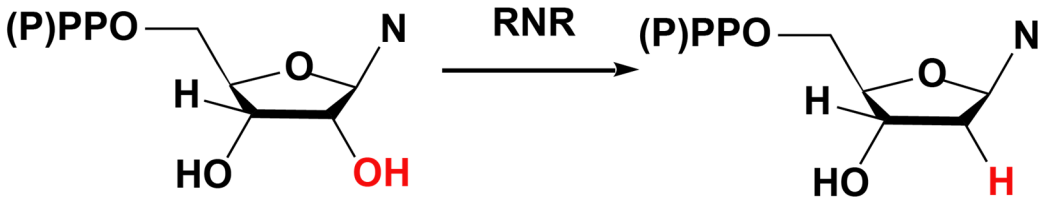

Figure 1.4 Catalysis by RNR. The reduction of NDP (NTP) to dNDP (dNTP) is initiated by the 3′–H abstraction by the cysteine (C_{439}) thiyl radical. The irreversible release of the water is proposed to drive the thermodynamically uphill RNR catalysis.[3]

All three RNR classes share basic structural features and similar catalytic mechanisms. Thus, they are considered to share a common evolutionary origin though the amino acid sequences of three classes are vastly different. The distinct catalytic feature shared by all RNRs is the abstraction of the 3′-hydrogen atom of the ribose by a transient thiyl radical to activate the ribonucleotide (substrate). The radical transfer from cofactor to active site cysteine in all class Ia

RNRs is energetically uphill but driven forward by irreversible dehydration of the ribose ring.[26,31]

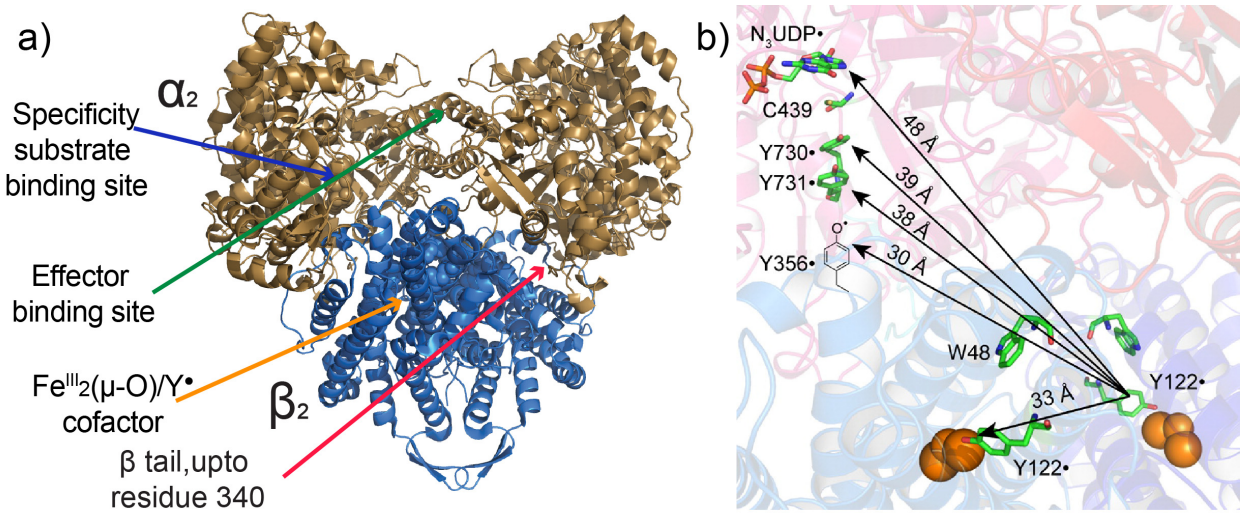

Figure 1.5 a) Docking model of the *E. coli* class Ia RNR. The figure is drawn by assembling the crystal structures of each subunit protein: 1RLR (α_2)[32], 1RIB (β_2)[33] b) Validating the docking model by PELDOR spectroscopy. By exploiting the half-sites reactivity of RNR, diagonal distances between Y_{122}• on one α/β pair and $DOPA_{356}$•, NH_2Y_{731}•, NH_2Y_{730}•, and an active-site N• generated from N_3-UDP on the second α/β pair have been measured. The pathway residues and S were built in from the docking model, in which Y_{356} is invisible (reproduced from reference 31).

The *E. coli* class Ia RNR is composed of two homo-dimeric subunits: α2 and β2 (Figure 1.5a). The crystallographic structure for each subunit protein is refined but the crystal structure of active α2β2 complex has not been obtained yet. The catalytic cysteine radical of *E. coli* class Ia RNR is C_{439} in the active site, which is housed in the α2 subunit. Two allosteric sites that control both the substrate specificity and turnover rate are also located in the α2 subunit. The diiron-tyrosyl radical cofactor (Fe_2–•Y122) is located in β2. The current model for the active oligomeric state has been developed from a docking model and is corroborated by pulsed electron-electron double resonance (PELDOR) spectroscopy (Figure 1.5b),[34] small-angle x-ray scattering (SAXS),[35] and transient spectroscopy of radical transport. The docking model predicts the distance between the active site C_{439} residue to the radical cofactor Y_{122} is ~35 Å.

1.2.2 Long-Range Radical Transport Pathway of RNR

Each catalytic cycle of RNR starts with the radical transfer from the Y_{122}• cofactor to the C_{439} active site and ends with the restoring of the Y_{122}•, thus completing the round trip across two subunits. This long 35 Å radical transport pathway across the subunit interface excludes single step superexchange[3] as a viable mechanism. A single step superexchange at 35 Å is estimated to be k_{cat} 10^{-4}–10^{-9} s^{-1} for $\beta = 1.2$ $Å^{-1}$ (β: the exponential distance decay constant, $k_{ET} = k^0_{ET}\, e^{-\beta(r-r_0)}$ in protein matrices[36]). This rate is inconsistent with the observed catalytic turnover rate constant of RNR (k_{cat} 2 –10 s^{-1}).[3] Thus, the sequential radical transport pathway has been proposed: long distance radical transport is achieved by several stepwise shorter distance radical transports (Figure 1.6).

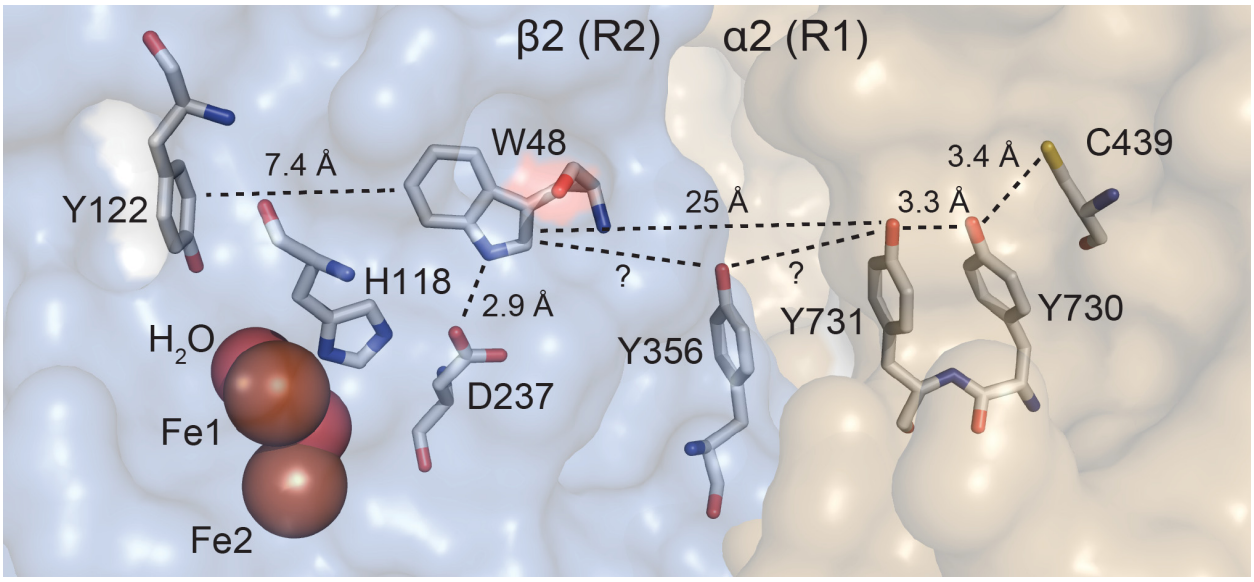

Figure 1.6 Proposed pathway of RNR radical transfer.[37] The same pathway is utilized for both forward and backward radical transport. Y_{356} location is not characterized by crystallography. The W_{48} radical cation was observed during cofactor assembly but not during catalysis.

Amino acids Y_{122}, W_{48}, Y_{356} in β subunit and Y_{731}, Y_{730} and C_{439} in α are essential residues in RNR catalysis. Some of these residues were suggested by point mutation experiments and conserved across many RNRs,[31,37] and thus are thought to be crucial to the radical transport pathway. Radical generation of some residues, observed by PELDOR in the last few years, provide direct support for some of the amino acid residues of the proposed pathway of radical transport.[34]

1.3 Approaches to Study PCET of Amino Acid Radicals

Understanding RNR is important from a human health since the therapeutic treatment of many diseases and cancers (leukemia,[38] myeloproliferative diseases,[39] and caners[40]) target the catalysis of RNRs. In addition to its clinical relevance, RNR is intriguing from a basic science perspective because RNR contains the consummate PCET pathway in biology; the equivalent of an electron and proton is transferred across two subunits over 35 Å, the longest PCET pathway in biology with very high fidelity for turnover ($>10^5$) before the radical loss.

The investigation on PCET kinetics is challenging in RNR because conformational steps precede radical transfer, preventing direct analysis by conventional methodologies. To investigate the PCET process, our research group has developed *photochemical RNRs* (photoRNRs). The rapid generation of an on-pathway radical using site specifically inserted photo-oxidants allows monitoring of radical species otherwise unresolvable (Figure 1.7a,b, d)[41−44] by steady-state spectroscopies.

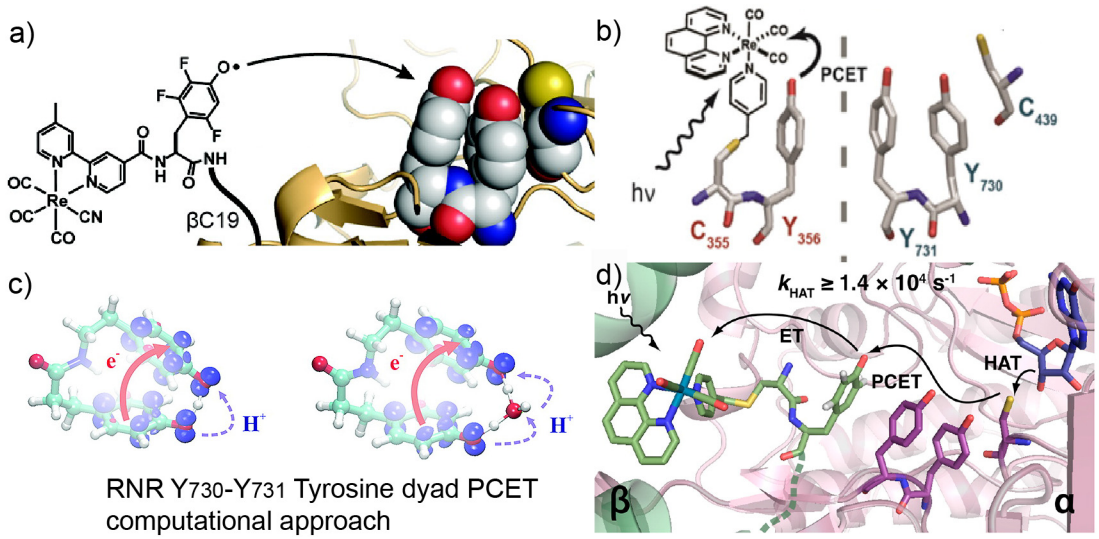

Figure 1.7 PhotoRNR studies suggest the unique redox cooperativity of the Y_{731}-Y_{730} dyad. a) Point mutations that disrupt the Y_{731}–Y_{730} dyad shut down radical transport.[41] b) The rate of Y_{356} oxidation depends on the presence of Y_{731} across the interface. c) Computational method on Y_{731}-Y_{730} dyad radical self-exchange mediated with/without a water molecule.[45] d) Hydrogen atom abstraction from substrate kinetics measurement was performed with photoRNR with a rhenium photo-oxidant.[44]

The study of photoRNRs has provided crucial insights into the radical transport management by RNR. An important discovery to the content of this thesis is the unique redox cooperativity of the Y_{731}-Y_{730} dyad. Corroborated by computation (Figure 1.7c)[45], the kinetics of radical transport of the dyad with photoRNR showed that the structural motif is closely tied to the catalysis.[41–44] These observations provide an imperative to analyze the correlation between the structure and the redox property in a model system, affording the de-convolution of the dyad structure from ancillary amino acids of the protein. While protein matrices provide a unique environment for chemistry, they have a very narrow range of tolerance for temperature, pH and structural modification. On top of the complex preparation, the conformational gating or other biochemical process pose complications.

The "reductionist" model system approach can provide a practical and simplified analysis platform for chemistry catalyzed by proteins. The model system can range from a small molecu-

lar model to modified proteins model. Tommos and co-workers have measured the reduction potentials of tyrosine and tryptophan amino acids in an ordered protein milieu within a small trifold α-helical synthetic protein (7.4 kDa) structure (Figure 1.8a).[46] Among numerous synthetic molecular mimics for enzymatic active sites,[47] many models of cytochrome *c* (Figure 1.8b) establish the validity of synthesis to faithfully emulate biological system. The model system provided an insight that the phenol of the Y_{244} residue serves as a H^+/e^- donor involved in the O–O bond cleavage.[48] Cytochrome *c* oxidase mimic **1** binds with dioxygen to form Fe^{III}-superoxo-Cu^{I} species at –60 °C. Upon warming up the complex to –40 °C, the O–O bond ruptures heterolytically resulting in Fe^{IV} oxoferryl and Cu^{II} hydroxo. Concurrently, the phenol (Tyr 244 mimic, colored red, Figure 1.8b) is oxidized to a phenoxy radical.

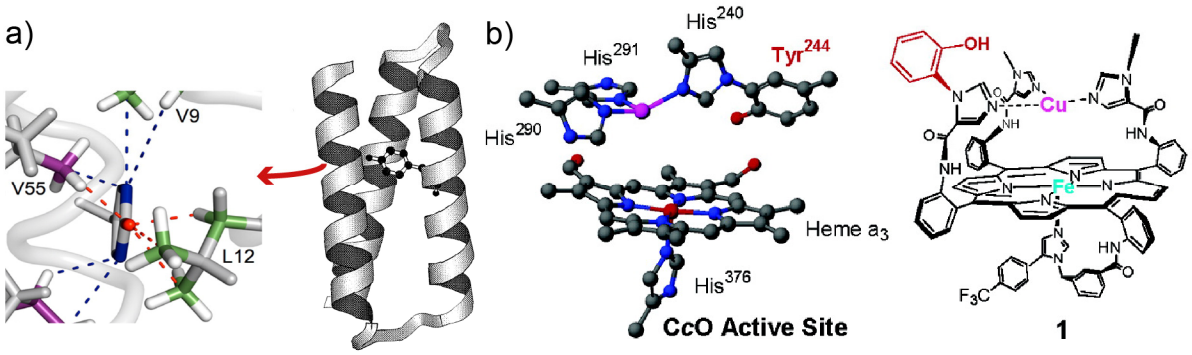

Figure 1.8 Model approach using peptides. a) Structural models of the tryptophan and tyrosine radical maquettes, denoted α_3W^1 and α_3Y^1. Figure is reproduced from reference 46. b) Active site model of cytochrome *c* oxidase bearing a Y_{244} mimic **1**. Figure is reproduced from reference 48.

1.4 Scope of Thesis

This thesis explores PCET in model systems to probe the mechanism of RNRs. Figure 1.9 – Figure 1.12 provides the thematic summaries of each chapter.

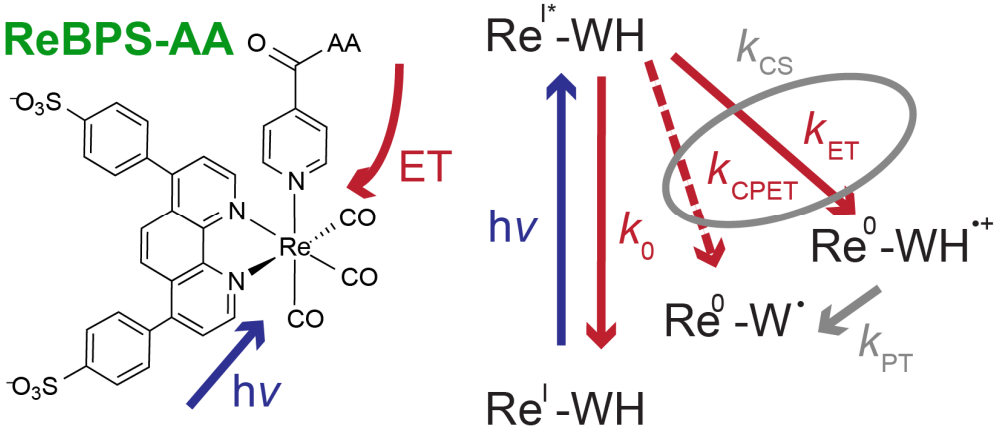

Figure 1.9 Summary of Chapter 2: The PCET oxidation kinetics of tryptophan and tyrosine in water using rhenium based photo-oxidants. Both intramolecular oxidation and bimolecular quenching studies were investigated. **ReBPS** refers to *fac*-[rhenium 1,10-bathophenenthroline sulphonate tricarbonyl pyridyl] complex.

Chapter 2 explores the fundamental understanding of amino acid radical generation mechanism (Figure 1.9). We designed an improved small molecule system (amino-acid appended photooxidants) to obtain water solubility, strong driving force, and no need for a flash quencher. With the new system, we aimed to provide a more comparable platform for the numerous reported photo-oxidant systems and augment our understanding of tryptophan PCET kinetics. The PCET kinetic mechanism was investigated using nanosecond laser spectroscopy over a pH range of 2–12. The oxidations of the amino acids were shown to follow an ETPT pathway.

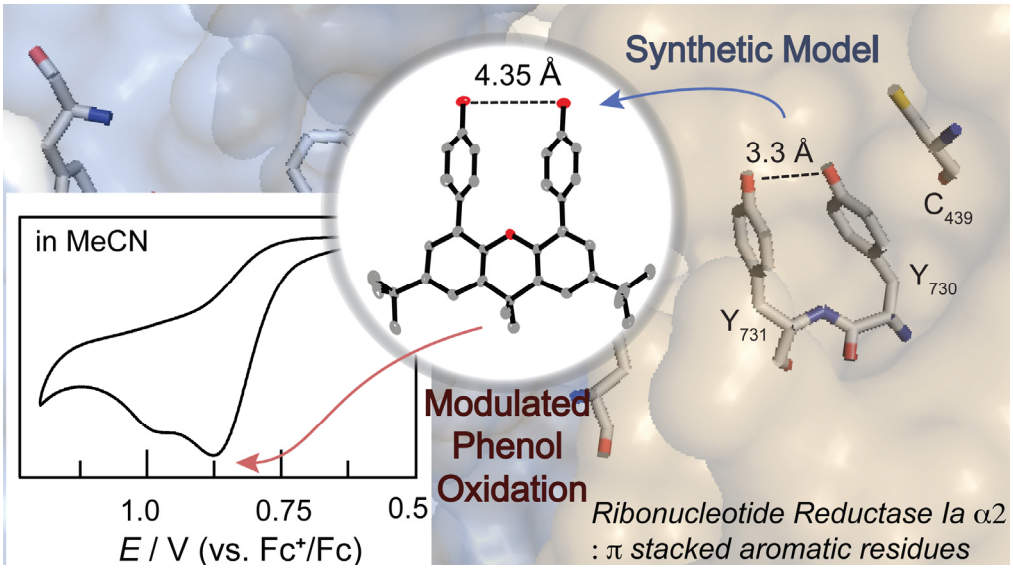

Figure 1.10 Summary of Chapter 3: The electrochemical analysis of the RNR tyrosine dyad synthetic model. The cofacial dyad phenol system was synthesized to emulate the tyrosine dyad Y_{730}-Y_{731} in RNR. Electrochemical and computational analysis were performed to probe the unique redox activity rendered from the dyad structure.

Chapter 3 delves into the unique properties of the Y_{730}-Y_{731} tyrosine dyad in α_2 subunit of RNR (Figure 1.10). Electrochemical and computational approaches were utilized to probe the correlation between the cofacial structure and redox properties. The cyclic voltammetry (CV) of cofacial phenol moieties placed on a xanthene backbone structure reveals that phenol oxidation is modulated within the dyad. The CV of cofacial phenol dyad in acetonitrile exhibits a splitting of one-electron waves with the first oxidation of the phenol dyad occurring at a lower positive potential (easier to oxidize) than that of a typical phenol. In contrast, a single phenol appended to a xanthene exhibits a two-electron process, consistent with reported oxidation pathways of phenols in acetonitrile. Computation captures the perturbed reduction potential resulting from the structural variation among dyad models and the electronic characteristics of generated phenol radicals.

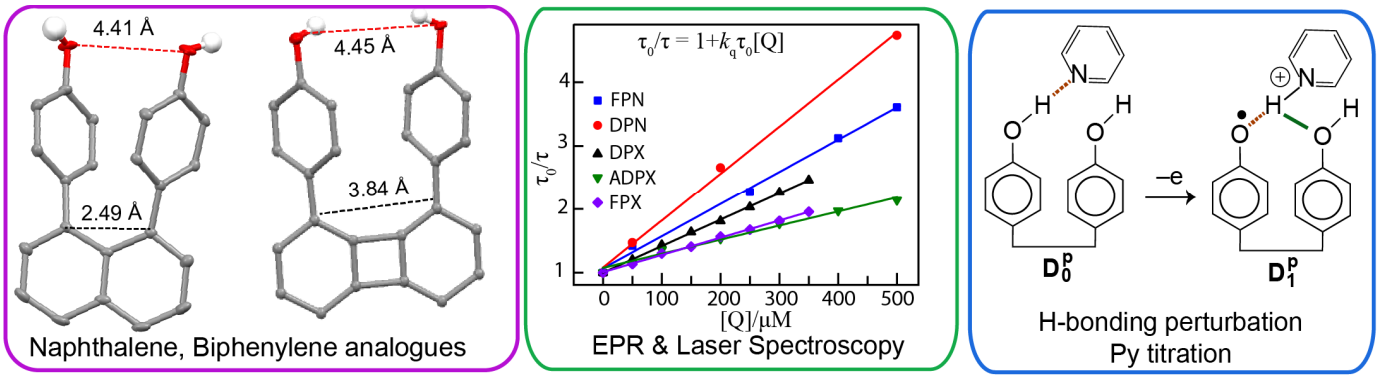

Figure 1.11 Summary of Chapter 4: Building upon the cofacial dyad system in Chapter 3, the effect of cofacial unit distance variation using different backbones (left), employing laser spectroscopy for bimolecular quenching kinetics and electron paramagnetic resonance spectroscopy (ENDOR and electron-spin-echo) (middle), and hydrogen bonding perturbation with external base pyridine titration (right) were tried.

Chapter 4 builds upon the discovery of Chapter 3 and investigates a larger parameter space: hydrogen-bonding perturbation, distance and electronic structure (Figure 1.11). Detailed thermodynamic and kinetic analysis resulting from electronic and π-distance perturbations are presented. The variation on the distance of phenol moieties was achieved by utilizing naphthalene and biphenylene backbone. The variation on the hydrogen-bonding network was produced by external base pyridine titration and regiomers of phenol moiety. In addition to the electrochemical analysis, laser spectroscopy and EPR were also performed to characterize the dyad system.

In Chapter 5, the polyproline peptide model systems of the bidirectional PCET pathway in the β2 subunit of RNR (Y_{122}-W_{48}-Y_{356}) was investigated by pulse radiolysis (Figure 1.12). The kinetics of radical transport between fluorotyrosines and tryptophan was measured to be comparable to the system of similar driving force (Figure 1.12). The data obtained from pulse radiolysis provide a method to reasonably approximate the total radical transport rate across the triad system, F_4Y-P_3-W-P_3-Y, analogous to $Y_{122} \rightarrow W_{48} \rightarrow Y_{356}$ in RNR.

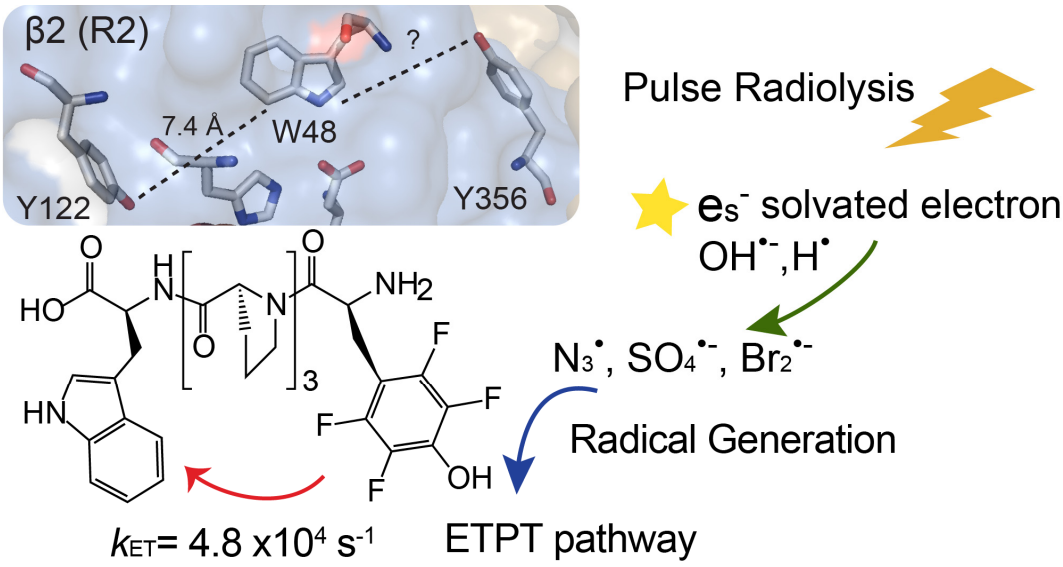

Figure 1.12 Summary of Chapter 5: Polyproline peptide model systems were built to emulate bidirectional long distance radical transport in the β2 subunit of RNR (Y_{122}-W_{48}-Y_{356}). Pulse radiolysis was employed to effectively generate radicals in the model system and to characterize fluorotyrosines (2,3-F_2Y and 2,3,5,6-F_4Y).

1.5 References

(1) Dempsey, J. L.; Winkler, J. R.; Gray, H. B. *Chem. Rev.* **2010**, *110*, 7024.

(2) Cukier, R. I.; Nocera, D. G. *Annu. Rev. Phys. Chem.* **1998**, *49*, 337.

(3) Stubbe, J.; Nocera, D. G.; Yee, C. S.; Chang, M. C. Y. *Chem. Rev.* **2003**, *103*, 2167.

(4) Marcus, R. A.; Sutin, N. *Biochim. Biophys. Acta - Rev. Bioenerg.* **1985**, *811*, 265.

(5) Marcus, R. A. *Angew. Chem. Int. Ed. Engl.* **1993**, *32*, 1111.

(6) Levich, V. G.; Dogonadze, R. R. *Dokl. Akad. Nauk SSSR* **1959**, *124*, 123.

(7) Closs, G. L.; Miller, J. R. *Science*, **1988**, *240*, 440.

(8) Hammes-Schiffer, S. *Acc. Chem. Res.* **2009**, *42*, 1881.

(9) Hammes-Schiffer, S. *Energy Environ. Sci.* **2012**, *5*, 7696.

(10) Hammes-Schiffer, S.; Soudackov, A. V. *J. Phys. Chem. B* **2008**, *112*, 14108.

(11) Cook, T. R.; Dogutan, D. K.; Reece, S. Y.; Surendranath, Y.; Teets, T. S.; Nocera, D. G. *Chem. Rev.* **2010**, *110*, 6474.

(12) Huynh, M. H. V; Meyer, T. J. *Chem. Rev.* **2007**, *107*, 5004.

(13) Frey, P. A.; Hegeman, A. D.; Reed, G. H. *Chem. Rev.*, **2006**, *106*, 3302.

(14) Derat, E.; Shaik, S. *J. Am. Chem. Soc.* **2006**, *128*, 13940.

(15) Meunier, B.; de Visser, S. P.; Shaik, S. *Chem. Rev.* **2004**, *104*, 3947.

(16) Whittaker, J. W. *Chem. Rev.* **2003**, *103*, 2347.

(17) Solomon, E. I.; Sundaram, U. M.; Machonkin, T. E. *Chem. Rev.* **1996**, *96*, 2563.

(18) Lancaster, C. R. D.; Haas, A. H.; Madej, M. G.; Mileni, M. *Biochim. Biophys. Acta, Bioenerg.* **2006**, *1757*, 988.

(19) Haas, A. *Biophys. J.* **2004**, *87*, 4298.

(20) Nordlund, P.; Reichard, P. *Annu. Rev. Biochem.* **2006**, *75*, 681.

(21) Dunn, R. V.; Munro, A. W.; Turner, N. J.; Rigby, S. E. J.; Scrutton, N. S. *ChemBioChem* **2010**, *11*, 1228.

(22) Davidson, V. L. *Adv. Protein Chem.* **2001**, *58*, 95.

(23) Tinberg, C. E.; Lippard, S. J. *Biochemistry* **2009**, *48*, 12145.

(24) Baik, M.; Newcomb, M.; Friesner, R. A.; Lippard, S. J. *Chem. Rev.* **2003**, *103*, 2385.

(25) Warren, J. J.; Winkler, J. R.; Gray, H. B. *FEBS Lett.* **2012**, *586*, 596.

(26) Stubbe, J.; van der Donk, W. A. *Chem. Rev.* **1998**, *98*, 705.

(27) Seyedsayamdost, M. R.; Reece, S. Y.; Nocera, D. G.; Stubbe, J. *J. Am. Chem. Soc.* **2006**, *128*, 1569.

(28) Reece, S. Y.; Seyedsayamdost, M. R.; Stubbe, J.; Nocera, D. G. *J. Am. Chem. Soc.* **2006**, *128*, 13654.

(29) Reece, S. Y.; Stubbe, J.; Nocera, D. G. *Biochim. Biophys. Acta* **2005**, *1706*, 232.

(30) Bleifuss, G.; Kolberg, M.; Pötsch, S.; Hofbauer, W.; Bittl, R.; Lubitz, W.; Gräslund, A.; Lassmann, G.; Lendzian, F. *Biochemistry* **2001**, *40*, 15362.

(31) Minnihan, E. C.; Nocera, D. G.; Stubbe, J. *Acc. Chem. Res.* **2013**, *46*, 2524.

(32) Uhlin, U.; Eklund, H. *Nature* **1994**, *370*, 533.

(33) Nordlund, P.; Eklund, H. *J. Mol. Biol.* **1993**, *232,* 123.

(34) a) Bennati, M.; Robblee, J. H.; Mugnaini, V.; Stubbe, J.; Freed, J. H.; Borbat, P. *J. Am. Chem. Soc.* **2005**, *127*, 15014. b) Seyedsayamdost, M. R.; Chan, C. T. Y.; Mugnaini, V.; Stubbe, J.; Bennati, M. *J. Am. Chem. Soc.* **2007**, *129*, 15748.

(35) Ando, N.; Brignole, E. J.; Zimanyi, C. M.; Funk, M. A.; Yokoyama, K.; Asturias, F. J.; Stubbe, J.; Drennan, C. L. *Proc. Natl. Acad. Sci. U.S.A.* **2011**, *108*, 21046.

(36) Langen, R.; Chang, I. J.; Germanas, J. P.; Richards, J. H.; Winkler, J. R.; Gray, H. B. *Science* **1995**, *268*, 1733.

(37) Minnihan, E. C.; Ando, N.; Brignole, E. J.; Olshansky, L.; Chittuluru, J.; Asturias, F. J.; Drennan, C. L.; Nocera, D. G.; Stubbe, J. *Proc. Natl. Acad. Sci.* **2013**, *110*, 3835.

(38) Anand, S.; Verma, H.; Kumar, L.; Singh, N. *Cancer Lett*. **1995**, *88*, 101.

(39) Engstrom, K. G.; Lofvenberg, E. *Blood* **1998**, *91*, 3986.

(40) Zhou, B.; Su, L.; Hu, S.; Hu, W.; Yip, M. L. R.; Wu, J.; Gaur, S.; Smith, D. L.; Yuan, Y.-C.; Synold, T. W.; Horne, D.; Yen, Y. *Cancer Res.* **2013**, *73*, 6484.

(41) Holder, P. G.; Pizano, A. A.; Anderson, B. L.; Stubbe, J.; Nocera, D. G. *J. Am. Chem. Soc.* **2012**, *134*, 1172.

(42) Pizano, A. A.; Olshansky, L.; Holder, P. G.; Stubbe, J.; Nocera, D. G. *J. Am. Chem. Soc.* **2013**, *135*, 13250.

(43) Pizano, A. A.; Lutterman, D. A.; Holder, P. G.; Teets, T. S.; Stubbe, J.; Nocera, D. G. *Proc. Natl. Acad. Sci.* **2012**, *109*, 39.

(44) Olshansky, L.; Pizano, A. A.; Wei, Y.; Stubbe, J.; Nocera, D. G. *J. Am. Chem. Soc.* **2014**, *136*, 16210.

(45) a) Kaila, V. R. I.; Hummer, G. *J. Am. Chem. Soc.* **2011**, *133*, 19040. b) Mayer, J. M.; Hrovat, D. A.; Thomas, J. L.; Borden, W. T. *J. Am. Chem. Soc.* **2002**, *124*, 11142.

(46) a) Tommos, C.; Skalicky, J. J.; Pilloud, D. L.; Wand, A. J.; Dutton, P. L. *Biochemistry* **1999**, *38*, 9495. b) Ravichandran, K. R.; Liang, L.; Stubbe, J.; Tommos, C. *Biochemistry* **2013**, *52*, 8907. c) Berry, B. W.; Martinez-Rivera, M. C.; Tommos, C. *Proc. Natl. Acad. Sci.* **2012**, *109*, 9739. d) Glover, S. D.; Jorge, C.; Liang, L.; Valentine, K. G.; Hammarström, L.; Tommos, C. *J. Am. Chem. Soc.* **2014**, *136*, 14039.

(47) a) Holm, R. H.; Kennepohl, P.; Solomon, E. I. *Chem. Rev.* **1996**, *96*, 2239. b) Holm, R. H.; Solomon, E. I. *Chem. Rev.* **2004**, *104*, 347. c) Holm, R. H.; Solomon, E. I. *Chem. Rev.* **2014**, *114*, 3367.

(48) a) Collman, J. P.; Decréau, R. A.; Yan, Y.; Yoon, J.; Solomon, E. I. *J. Am. Chem. Soc.* **2007**, *129*, 5794. b) Collman, J. P.; Decréau, R. A. *Chem. Comm.* **2008**, *41*, 5065.

Page intentionally left blank

Chapter 2 –

Small Molecule Systems for PCET Kinetics Analysis on Amino Acids- Tryptophan and Tyrosine

2.1 Introduction

Proton-coupled electron transfer (PCET) has been acknowledged as a fundamental mechanism for amino acid radical generation in numerous biological systems.[1,2] The PCET mechanism encompasses a wide range of transfer modes for the electron and proton. If an electron transfer occurs first and is then followed by a proton transfer in a stepwise pathway, it is referred as ETPT, while the reverse order is referred to as PTET. The simultaneous transfer of an electron and a proton without any intermediate generation is designated as concerted electron-proton transfer (CPET). In the case of CPET, the proton and the electron may have different acceptors (bi-directional CPET) or the same acceptor (uni-directional CPET).[3] Due to its relevance to renewable energy and enzymology, the PCET oxidation of amino acids has been widely studied utilizing diverse model systems and methods.[4–9] The vast parameter spaces that influences PCET kinetics require extensive experimental and theoretical investigations.

Amino acid radicals play an essential role in the biochemistry of metabolism and catalysis.[10] In physiological conditions, the generation and transport of amino acid radicals requires the coupling of a proton and an electron. Tryptophan and tyrosine are the two amino acids that are widely involved in enzyme radical chemistry as exemplified in photosystems II (PSII),[11] ribonucleotide reductases (RNR)[12,] and DNA photolyases.[10] Tryptophan radical cation, tryptophan radical and tyrosine radical have distinct and well-known absorption features. Therefore, transient absorption laser spectroscopy is a good tool to study the kinetics of these amino acid radicals.[13] Additionally, photo-oxidants with appended amino acids provide good platforms to study intramolecular PCET oxidation kinetics. The series of tris(bipyridine)ruthenium(II) chloride ($Ru(bpy)_3$) systems with appended amino acids are very soluble in water thus allowing PCET to be examined in the aqueous environment, as opposed to the nonaqueous environment employed

in kinetics studies of amino acid model systems Their amino acid radical generation kinetics show that the PCET mechanism spans ETPT, CPET, and PTET based on the pH and the photo-oxidant strength (Scheme 2.1 Rubpy-AA[13–16]). Ru-based systems in general require additional flash-quenchers to obtain sufficiently long lifetimes and to access the potent oxidant (Ru^{III}).

Scheme 2.1 Structure of model systems: a) **ReBpy** system: modified bpy ligand is used for amino acid attachments. b) **RePhen** system: axial pyridal ligand is used to append amino acids. The complex is a PF_6 salt and insoluble in aqueous solution. c) **RuBpy** system: water soluble, requiring flash quenchers. d) **ReBPS** system: analogous to RePhen system and soluble in aqueous solution.

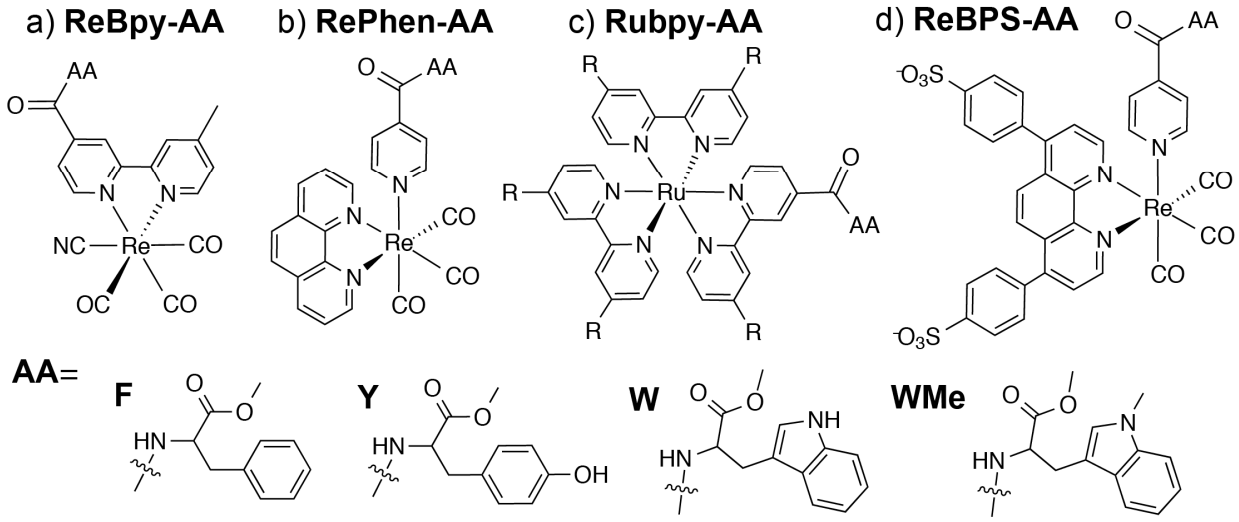

Our group has utilized rhenium-based photo-oxidants **ReBpy-AA** and **RePhen-AA** (Scheme 2.1 a, b) and studied the intramolecular PCET oxidation of tyrosine and fluorotyrosines.[5,6] The complex **ReBpy-AA** does not generate a detectable population of tyrosyl radicals via the oxidation of tyrosine, even though the $^3[Re^I]$* state (~ 1.59 V vs. NHE, all reduction potentials in this chapter are referenced to NHE) has enough driving force (~ 400 mV) to perform the oxidation. Fast charge recombination and short-lived excited states were attributed to the inability to perform the slower CPET process (protonated tyrosine oxidation pH <10). The photochemical studies enabled the development of photoRNR where photo-oxidants were used to generate an on-pathway radical with temporal control using the ReBpy complex as a phototrig-

ger.[17,18] The **RePhen-AA**[6] complexes with a phenanthroline ligand have a longer excited state lifetime and stronger oxidizing strength but these PF_6 salts are insoluble in aqueous solution. An attempt to solubilize these complexes by salt exchange with nitrate and triflate was not successful. For emission quenching studies of **RePhen-AA**, the CPET oxidation of amino acids required the addition of external base in organic solvents.[6] Since the solvent dipole and dielectric influence the energetics of charged intermediates and transient states, it is very desirable to be able to maintain a consistent solvent for systematic comparison and preferably water as it is the most pertinent to translation to biological studies.

To augment our understanding of amino acid PCET kinetics, this chapter reports an improved photooxidant shown in Scheme 2.1d with great water solubility, a strong driving force for amino acid oxidation, and no need of flash quencher. The rhenium based photooxidant system was synthesized with BPS (4,7-diphenyl-1,10-phenanthroline disulfonic acid) ligands[19] to utilize its great water solubility.[20] The tosyl acid groups' low pK_a (~2.8)[21] assures that the charge on the complex remains constant throughout the kinetic study at any pH. The constant charge of the complex across the pH range in turn assures that the dipole moment of the complex does not affect the electron transfer kinetics as shown by Lauz *et al*.[22] The strong π-acceptor ligand phenanthroline contributes to the potent oxidizing power of its MLCT excited state, $^3[Re^I]^*$. The perpendicular placement of the amino acids relative to the phenanthroline ligand, achieved via a pyridyl attachment, is designed to ensure a slower charge recombination rate.[5] The PCET kinetics of the new model system has investigated using nanosecond laser spectroscopy at the pH range 2–12, as reported below.

2.2 Results

2.2.1 Synthesis

The series of photo-oxidants (Scheme 2.1) with appended amino acids, **ReBpy-AA** (AA=W and F) and **ReBPS-AA** (AA=Y, F, W, and WMe), were successfully synthesized at a moderate yield of 30–40% by following published procedures with a small modification: amino acid appended pyridines were used instead of 1-hydroxymethyl pyridines for an axial ligand.[5,6,23] The general synthetic strategy is to substitute the BPS ligand for two carbonyl groups of the synthon ($Re(CO)_5Cl$), followed by axial ligand substitution with amino acid-appended pyridine. The products were purified by column chromatography and analyzed by NMR and ESI-MS.

2.2.2 Ground State Electronic Absorption and Steady-State Emission Spectra

Ground-state absorption and steady-state emission spectra of **ReBpy-F**, **ReBpy-W** (Figure 2.1 top), and **ReBPS-F**, **ReBPS-W** and **ReBPS-Y** (Figure 2.1 bottom) were obtained in aqueous phosphate buffer solution. Ground-state absorption spectra of **ReBPS-AA**s and **ReBpy-AA**s are almost identical regardless of the identity of appended amino acids, indicating that the UV-vis absorption features observed are mostly due to the corresponding Re complex. From the ground-state absorption spectra, we concluded that 355 nm (the 3rd harmonic of an Nd:YAG laser) is a good excitation wavelength for both **ReBpy-AA**s and **ReBPS-AA**s. The excitation at 355 nm also ensures that phenol and indole will not be directly excited to generate radical species via photolysis during laser studies owing to the higher energy absorption profiles of these those moieties.[24]

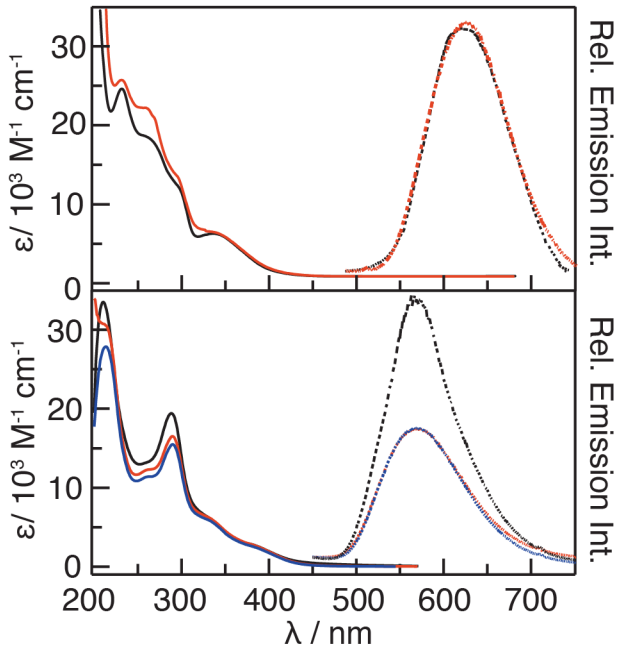

Figure 2.1 Electronic absorption (solid lines) and emission spectra (dotted line) of (top) **ReBpy-F** (black) and **ReBpy-W** (red), and (bottom) **ReBPS-F** (black), **ReBPS-W** (red), and **ReBPS-Y** (blue) at 50 μM concentration in 50 mM pH 7 phosphate buffer at room temperature. For emission spectroscopy, excitation at λ_{ex}= 355 nm was used.

In steady-state emission spectra, the difference between the **ReBpy-F** and **ReBpy-W/Y** and the difference between **ReBPS-F** and **ReBPS-AA** can be attributed to phenomena related to the nature of the appended amino acid; because F is effectively redox inactive.[25] Steady-state emission spectra at room temperature showed λ_{max}= 570 nm (17544 cm^{-1}) for **ReBPS-F** and 606 nm (16500 cm^{-1})[5] for **ReBpy-F** (Figure 2.1).

Static quenching of the emission intensity for **ReBPS-W/Y** as compared to **ReBPS-F** did not depend on changes in pH. The emission spectra of **ReBpy-W** and **ReBpy-F** were identical, indicating that no emission quenching arises from W oxidation. This is consistent with published results regarding tyrosine and fluorotyrosine oxidation by the same photo-oxidant.[5] **ReBpy-Y** cannot oxidize tyrosine into tyrosyl radicals at pH values below the pK_a of tyrosine (~ 10), while it can oxidize tyrosinate rapidly (within 10 ns). The same argument is applicable to **ReBpy-W**;

inability of the [Re] excited state to be quenched by the protonated form of the appended amino acid is consistent with the data obtained by laser spectroscopy presented below.

2.2.3 Laser Spectroscopy

2.2.3.1 ReBPS-AA

The PCET kinetics of **ReBPS-AA** complexes was investigated using nanosecond laser spectroscopy. The set-up used for the experiments follows previously published methods.[26] The transient absorption (TA) spectra and the single wavelength emission decay kinetics, monitored at the λ_{max} = 570 nm **for ReBPS-F** emission, are provided in Figure 2.2.

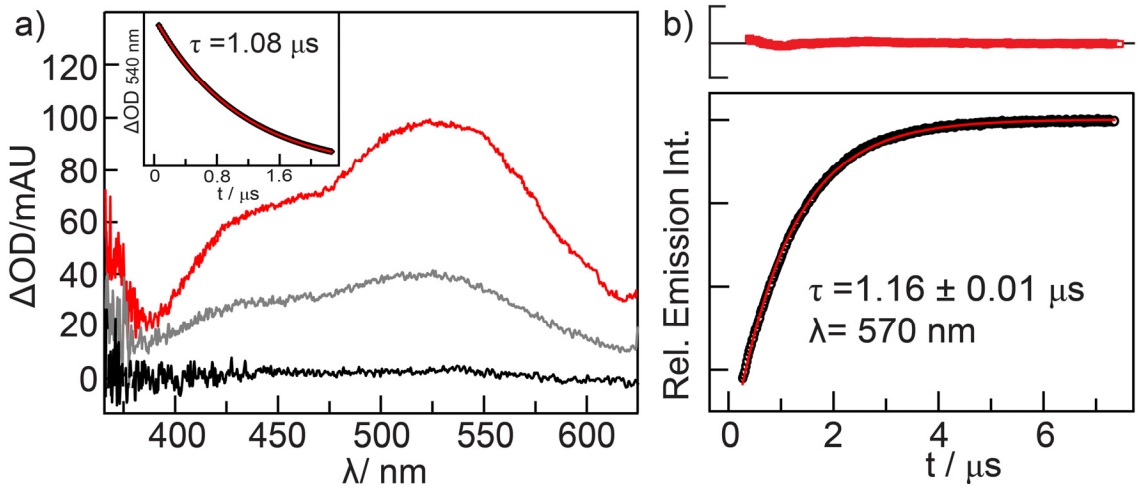

Figure 2.2 ReBPS-F: a) Transient absorption spectra taken at the time delays of: 60 ns (▬), 1460 ns (▬), and 4960 ns (▬), 50 μM in 100 mM phosphate buffer at pH 7. (Inset) Single wavelength kinetic trace and monoexponential fit for the ^{3}MLCT signal monitored at 540 nm. b) Single wavelength emission kinetics trace monitored at 570 nm (black) and the monoexponential fit (red). The residuals of the fit are plotted above the emission trace. The scale of relative emission intensity of the residuals to the emission trace is 1:10.

The mono-exponential decay of **ReBPS-F** ^{3}[Re^I]* assures that there is no photochemical complication due to BPS regioisomers[19,23] and it also indicates that the lifetime of this complex serves as a good τ_0 for the other **ReBPS-AA** complexes. The ^{3}[Re^I]* of **ReBPS-F** has broad TA

spectral feature at λ_{max} = 540 nm and a shoulder at λ_{max} = 425 nm. The decay of this transient signal agrees with the emission lifetime decay ($\lambda_{max,em}$= 570 nm) of $\tau = 1.16 \pm 0.05$ µs.

The transient absorption spectra of **ReBPS-AA** systems (AA ≠ F) are shown in Figure 2.3 (the **ReBPS-F** spectrum of Figure 2.2 is provided for reference). The absorption features of radicals $W^{\bullet}$ (λ_{max}= 510 nm), $Y^{\bullet}$ (λ_{max}= 410 nm), and $WMe^{\bullet+}$ (λ_{max}= 560 nm)[27] cannot be deconvoluted from the dominating $^3[Re^I]$* TA signal. Although the signal to noise resolution is low, the radical features can be seen after most of **ReBPS** $^3[Re^I]$* excited state decayed away (~2.8 µs) (Figure 2.3b). Notwithstanding, the significant spectral overlap makes it difficult to obtain accurate kinetics; accordingly kinetics analysis of the photogenerated amino acid radicals was performed using emission lifetime measurements rather than TA. Single wavelength emission kinetics traces (monitored at λ_{max} = 570 nm) for each **ReBPS** complex are shown in Figure 2.4. And photophysical characteristics of relevant complexes are summarized in the Table 2.1.

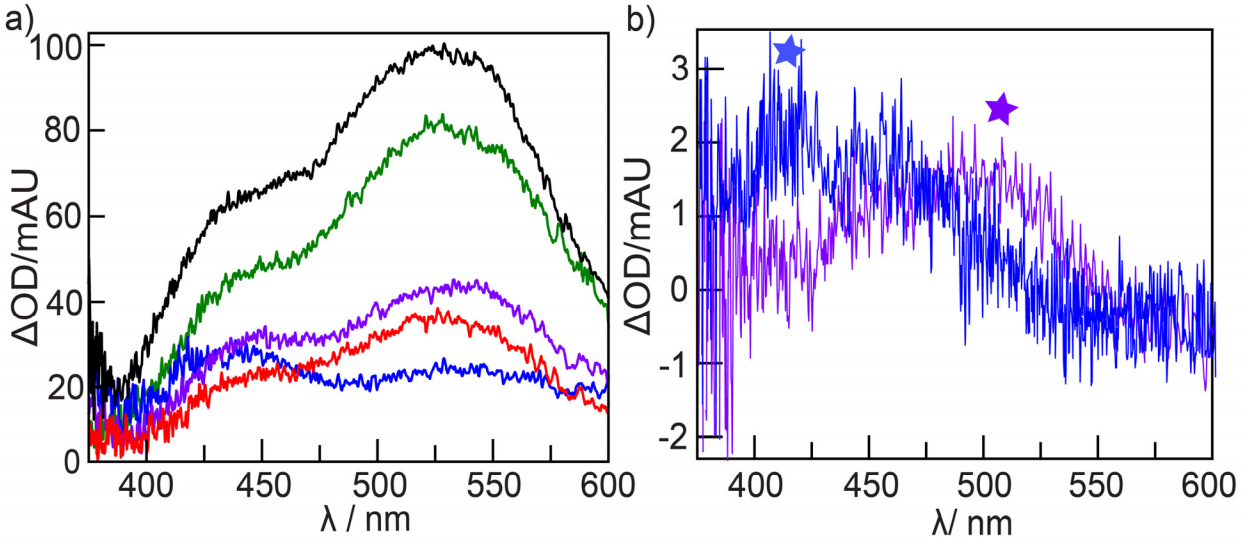

Figure 2.3 a) **ReBPS-AA: AA = F** (black, pH 7), **Y** (green, pH 7), **Y** (blue, pH 12), **WMe** (red, pH 7), **W** (violet, pH 7) 50 ns after 355 nm excitation. The sample was dissolved to 50 µM in aqueous 100 mM phosphate buffer solution. b) TA spectra of **ReBPS-Y** (blue) and **ReBPS-W** (violet) taken at 2850 ns after 355 nm excitation. The sample was dissolved to 50 µM in aqueous 100 mM phosphate buffer pH 12 solution.

Table 2.1 Thermodynamics and photophysical properties of Re-based photooxidant complexes: ^{3}MLCT energy, λ_{abs}, λ_{em}, and τ_{em}

Complex	λ_{abs}/ nm [a]	λ_{max}/ nm [b] $^3[Re^I]$*	λ_{em}/ nm	τ_{em}	ΔG°_{MLCT}
ReBpy-F [c]	358	380, 475	606	59.4 ns	1.59 V
RePhen-F [d]	335	300, 450	550	0.71 µs	1.70 V
ReBPS-F [c]	270, 330	425, 540	570	1.16 µs	1.80 V [e]

[a] ground state UV-vis spectra absorption maximum, [b] λ_{exc}= 355 nm, obtained from TA spectra, [c] obtained in aqueous solution, [d] obtained in dichloromethane[6], [e] The reduction potential of $^3[Re^I]$* ($Re^{I*/0}$ ~1.8 V vs. NHE) was estimated by constructing a Latimer diagram.[28,29]

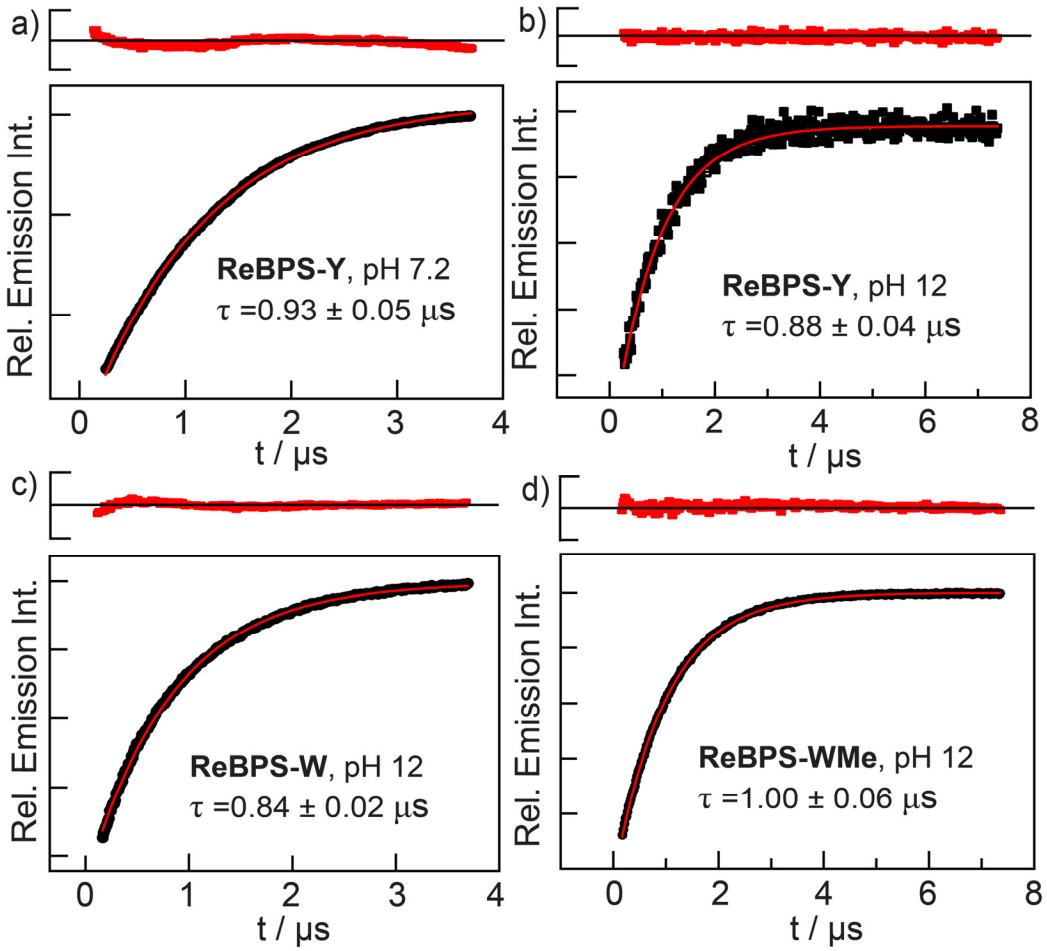

Figure 2.4 Single wavelength kinetics traces of **ReBPS-AA** (AA=W, WMe, and Y), monitored at emission λ_{max} = 570 nm. The residual of the monoexponential fit is provided above the emission trace. a) **ReBPS-Y**, pH 7.2, b) **ReBPS-Y**, pH 12, c) **ReBPS-W**, pH 7.2 d) **ReBPS-WMe**, pH 7.2. The samples were dissolved to 50 µM in 100 mM phosphate buffer and spectra were obtained in room temperature.

2.2.3.2 ReBpy-AA

For the **ReBpy** platform, the pure ET oxidation kinetics and charge recombination were reported for tyrosinate and fluorotyrosinates.[5] We decided to use this well-developed platform to investigate tryptophan, another essential amino acid radical in RNR. Synthesis of **ReBpy-W** was achieved with a reasonable yield by following the reported method.[5] Transient absorption spectra of **ReBpy-F** and **ReBpy-W** and the single wavelength emission decay kinetics (λ_{det} = 600 nm) are shown in Figure 2.5. The indolic proton has a high pK_a ~ 17 and indolic proton radical cation has a pK_a ~ 4.3 in water .[10] The overlay of **ReBpy-W** and **ReBpy-F** TA spectra 40 ns after excitation at 355 nm is provided in Figure 2.5c. The TA of **ReBpy-W** looked like an overlapped features of W radical (λ_{max} = 510 nm) and ^{3}[Re]^{I*} of **ReBpy** (λ_{max} = 475 nm). The emission lifetime of **ReBpy-W** was not quenched significantly from that of **ReBpy-F** (Figure 2.5a, b) and the observation matched the static emission data, thus the [Re]^{I*} was shown to be incompetent in W oxidation.

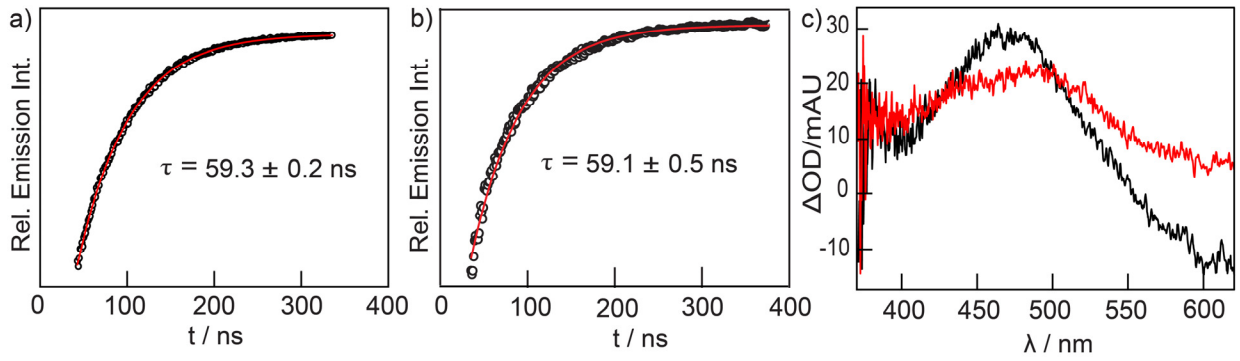

Figure 2.5 ReBpy-AA: a) Emission single wavelength kinetics trace of **ReBpy-F**. b) Emission single wavelength kinetics of **ReBpy-W**. c) Transient absorption spectra of **ReBpy-W** (red) and **ReBpy-F** (black) 40 ns after 355 nm excitation. The sample was dissolved to 50 μM in the aqueous solution in the 50 mM phosphate buffer at pH 7. The spectra were obtained in room temperature. Emission trace was monitored at 600 nm.

One possible explanation for the inability of W oxidation in **ReBpy-W** is that only certain conformations "sampled" during the tumbling of **ReBpy-W** in solution can promote PCET

oxidation, resulting in minimal quenching. To test this hypothesis, we performed the Stern-Volmer bimolecular quenching analysis using **ReBpy-F** and *N*-acetyl-tryptophan (**AcW**) (Figure 2.6).[8] In the bimolecular quenching experiment, the dependence of excited state quenching on the concentration of tryptophan was measured. In a bimolecular quenching experiment, **ReBpy-W** is free of any conformational limit but the quenching rate observed could be limited by the diffusion rate.

2.2.2.3 Bimolecular Quenching of ReBpy-F by AcW

Experiments monitoring the bimolecular quenching of **ReBpy-F** $^3[Re^I]$* emission by **AcW** were performed to investigate the kinetics of tryptophan oxidation. The quenching of **ReBpy-F** $^3[Re^I]$* showed a linear correlation to [**AcW**] and the bimolecular quenching rate constants were greater at higher pH (Figure 2.6, Table 2.2). The higher pH provides more solution species that can serve as a proton acceptor (base buffer, -OH). The dependence of bimolecular quenching rate on pH is indicative of CPET pathway contribution and will be described in the discussion section. The spectral features of tryptophan radical (pH = 7 and 12) and tryptophan radical cation (pH = 2) were observed, confirming that tryptophan was oxidized by the **ReBpy-F** excited state.

Table 2.2 The rate constants of bimolecular quenching of **ReBpy-F**, $Ru(bpy)_3$, and $Ru(dmb)_3$ by **AcW**. Bolded rate constants represent results obtained in this report.

Photo-oxidant	E^0 vs. NHE	k_q pH 2.8	k_q pH 7.2	k_q pH 12.0
ReBpy-F	1.60 V[5]	**$1.71\pm 0.23\times10^9$**	**$3.65\pm 0.23\times10^9$**	**$9.14\pm 0.13\times10^9$**
$[Ru(bpy)_3]$	1.26 V	2×10^9 (pH= 3–12) [13–15]		
$[Ru(dmb)_3]$	1.10 V	1.5×10^8 (pH= 4–11) [13–15]		

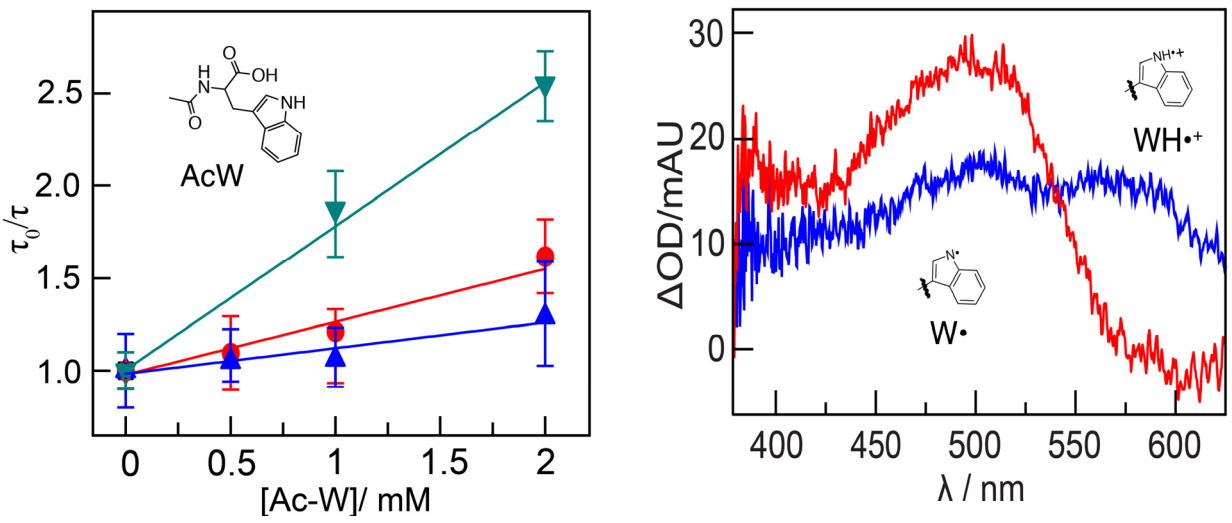

Figure 2.6 (left) Bimolecular emission quenching kinetics **ReBpy-F –AcW**; **ReBpy-F** 50 μM in 50 mM phosphate buffer at pH 2 (blue), 0 7 (red) and 12 (green). Acetylated-tryptophan (AcW) concentration (0–2 mM), monitored at 600 nm ($\lambda_{max,em}$ of **ReBpy-F**). (right) Transient absorption spectra of **AcW** bimolecularly oxidized by **ReBpy-F,** 40 ns after 355 nm excitation. The TA spectrum at pH 2 (blue) shows the characteristics of tryptophan radical cation (~560 nm) while the TA spectrum at pH 7 (red) shows tryptophan radical (~510 nm).

2.3 Discussion

2.3.1 ReBPS-AA Systems

The excited-state quenching pathways for **ReBPS-AA** with AA = F and with redox active amino acids (AA = W, WMe, or Y) are shown in Scheme 2.2a and b, respectively. Without appended redox active amino acids, the observed emission lifetime τ_0 is the sum of the radiative decay (k_R) and non-radiative (k_{NR}) decay rate constants of the $^3[Re^I]^*$ (Eq. 2.1).

$$\text{(Eq. 2.1)} \qquad \boldsymbol{k_0 = \frac{1}{\tau_0} = k_R + k_{NR}}$$

Regardless of mechanistic pathways, the decay dynamics should appear mono-exponential due to a single excited state species. When redox active amino acids are present, the amino acid oxidation provides an additional decay route for $^3[Re^I]^*$ as compared to the F analog arising from charge separation, denoted as k_{CS},

$$\text{(Eq. 2.2)} \quad \boldsymbol{k_{CS} = k_{obs} - k_0 = \frac{1}{\tau_{obs}} - \frac{1}{\tau_0}}$$

The rate constants for charge separation, k_{CS}, is the weighted sum of all possible amino acid radical generation pathways,

$$\text{(Eq. 2.3)} \quad \boldsymbol{k_{CS} = k_{ETPT} + k_{CPET} + k_{PTET}}$$

The charge separation rate constants, k_{CS} calculated using Eq. 2.2, are tabulated in Table 2.3.

Scheme 2.2 (a) The decay pathway of $^3[Re^I]^*$ with appended F. F does not provide an additional decay pathway thus the observed rate constant can be defined as k_0. The k_0 includes the contribution from radiative decay, k_R and non-radiative decay, k_{NR} (b) The PCET oxidation pathways for appended W. In addition to k_0, the PCET oxidation pathway contributes to the observed k_{obs}. The PTET pathway is unlikely for W thus omitted.

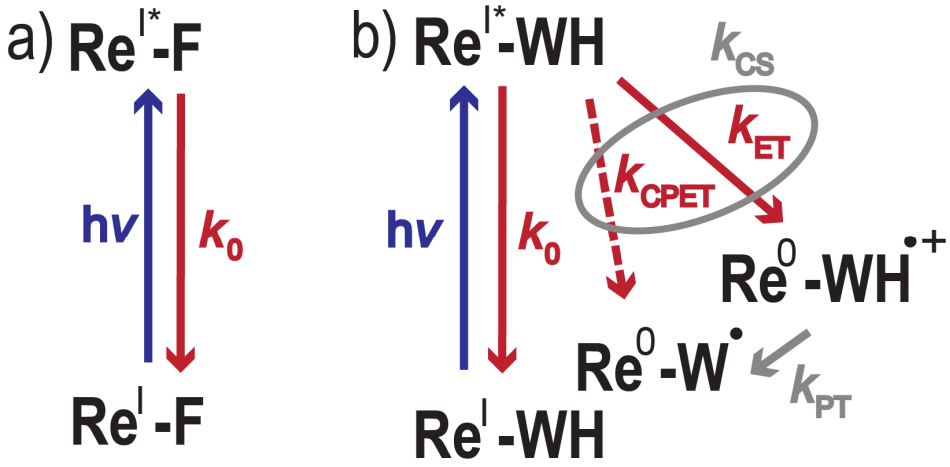

Table 2.3 k_{CS} charge separation rate constants (s^{-1}) as determined from emission quenching

Re complex	pH 12	pH 7.2	pH 2.8
ReBPS-Y	$2.35 \pm 0.10 \times 10^5$	$2.13 \pm 0.11 \times 10^5$	$0.86 \pm 0.07 \times 10^5$
ReBPS-W	$2.62 \pm 0.05 \times 10^5$	$1.65 \pm 0.15 \times 10^5$	$1.87 \pm 0.11 \times 10^5$
ReBPS-WMe	$0.99 \pm 0.06 \times 10^5$	$0.90 \pm 0.13 \times 10^5$	$1.17 \pm 0.08 \times 10^5$

The charge separation rate constant, k_{CS} increased with pH for Y; from pH 2.8 to pH 12, the tyrosine k_{CS} increased 2.7 fold. That of tryptophan overall increased 1.4 fold from pH 2.8 to pH 12; the difference between rate constants at pH 7.2 and pH 12 is statistically insignificant,

given the error of measurements. Unlike Y and W, the charge separation rate of WMe decreased by 0.8 fold. All changes in k_{CS} are logarithmically 0th order to the change of pH, in contrast to other reported amino acid oxidation kinetics where the log(k_{CS}) had a linear dependence of 0.5~1 on the pH.[8,13,14,15]

To evaluate the meaning of the observed pH independent trend, the redox property of amino acids needs to be considered in the context of intermolecular system. An ETPT pathway entails that the ET is the rate-determining step because the consequent proton transfer is fast due to the low pK_a of the amino acid radical cations as shown in the Pourbaix diagram (Figure 2.7).[4,30,31] Thus, the lack of radical cation observation (intermediate) does not contradict an ETPT pathway. Also, a PTET pathway is unlikely for W (pK_a^W ~17) in the experimental pH range and will be only competent for Y (pK_a^Y ~10) in a pH >10.[7]

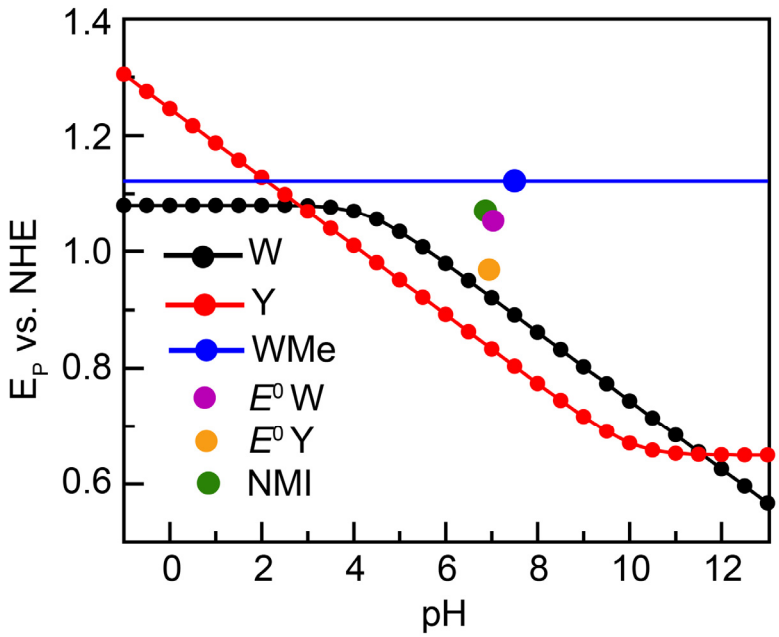

Figure 2.7 Pourbaix diagram constructed from E_P (W$^{\bullet}$/W) (black) and E_P (Y$^{\bullet}$/Y) (red) measured by differential pulse voltammetry of aqueous solutions.[30] The E_P of 1-methyl-tryptophan (blue) was measured at pH 7.2 and was pH independent. The E^0 of W, Y and NMI (*N*-methyl indole) were measured by pulse radiolysis at pH 7. [4,31].

To understand the weak dependence of k_{CS} upon pH change, each component of the overall rate was evaluated. First, the rate equation for WMe can be simplified to the following since there is no transferable proton;

(Eq. 2.4) $\boldsymbol{k_{CS} = k_{ET}}$, simplified for WMe

The standard reduction potentials of the protonated indole (pH < 17) and 1-N-methyl indole are comparable (Figure 2.7). As W and WMe are estimated to have similar reorganization energies for the pure ET process, the k_{ET} (WMe) serves as a good approximation for k_{ETPT} (W). In case of W oxidation, the PTET contribution is regarded as negligible due to the high pK_a of indole N-H proton (~17). Thus Eq. 2.3 can be simplified as following:

(Eq. 2.5) $\boldsymbol{k_{CS} = k_{ETPT} + k_{CPET}}$, simplified for W

The ETPT pathway of **ReBPS-W** should proceed via tryptophan radical cation (pK_a 4.7) as an intermediate. However, the transient absorption spectra could not confirm any significant amount of $WH^{\bullet+}$ at pH 2.8 due to the spectral overlap with $^3[Re^I]$*. Moreover, if PT is faster that ET, then $W^{\bullet}$ will be observed as the primary photoproduct, even for an ETPT pathway. This has been established in a recent study of W photoRNRs.[32] Inasmuch as the ET rate is independent from the PT rate in an ETPT pathway, substitution of k_{ETPT}^{W} with k_{ET}^{WMe} yields a reasonable approximation for the contribution of k_{CPET}^{W}. From this simple approximation of substituting k_{ET}^{WMe} into Eq. 2.5, the percentage contributions of k_{CPET}^{W} to k_{CS}^{W} were tabulated in Table 2.4. The results of k_{CPET}^{W} based on these data are: ~ 62 % (pH 12), ~ 46 % (pH 7.2), and 37% (pH 2.8). The percent contribution serves as only comparison since the substitution of k_{ETPT}^{W} with k_{ET}^{WMe} may result in a larger error than estimated and the k_{CS}^{W} dependence on pH was not monotonous. However, the higher pH provides more solution species that can serve as a proton acceptor (base buffer, -OH). Thus the higher contribution of CPET to the observed quenching pro-

cess at higher pH is not surprising. In recent study of $[Ru(bpy)_3]^{2+}$-tryptophan system by Hammarström and co-workers[33], the stronger photooxidant resulted in ETPT pathway while the weaker photooxidant resulted in a CPET pathway and the weak pH dependence of k_{cs} (slope ~ 0.1 for log(k_{cs}) vs. pH). The oxidizing power of **ReBPS-AA** system is much higher than the $[Ru(bpy)_3]^{2+}$ species,[13–15] thus assigning ETPT as a dominant pathway seems reasonable. It would be enlightening to see how these contributions change with a deuterium kinetic isotope effect.

Table 2.4 k_{CS} charge separation rate constants (s^{-1}) as determined from emission quenching

Re complex	pH 12	pH 7.2	pH 2.8
a. **ReBPS-W**	$2.62 \pm 0.10 \times 10^5$	$1.65 \pm 0.15 \times 10^5$	$1.87 \pm 0.11 \times 10^5$
b. **ReBPS-WMe**	$0.99 \pm 0.06 \times 10^5$	$0.90 \pm 0.13 \times 10^5$	$1.17 \pm 0.08 \times 10^5$
c. CPET (a–b)	$1.63 \pm 0.16 \times 10^5$	$0.75 \pm 0.37 \times 10^5$	$0.70 \pm 0.15 \times 10^5$
CPET %	62.2 %	45.5%	37.4%

For tyrosine, Eq. 2.5 and Eq. 2.4 are both appropriate to describe the charge separation event depending on the pH of the solution. At pH 11, 90% of tyrosine (pK_a 10) in **ReBPS-Y** is deprotonated. Thus, the main contribution to charge separation is ET from tyrosinate, expressed by k_{ET}^{Y-} (Eq. 2.4). The PTET pathway rate k_{PTET} is determined by k_{PT}^{Y} (tyrosine deprotonation rate) and k_{ET}^{Y-} (tyrosinate oxidation ET rate). At pH < 9, less than 10% of tyrosine is deprotonated , so that the contribution from PTET pathway is minimal (Eq. 2.5).

The intramolecular tyrosine oxidation rates were compared to the analogous, **RuBpy-Y** system, studied by Hammarström et al.[13] The pure ET rate at pH 2.8 for **RuBpy-Y** was measured to be 10^3 times faster than the ETPT rate at pH 10.34 (Table 2.5).[13] In contrast, the charge separation rates of **ReBPS-Y** were much faster with little variance (Table 2.5). The reduction poten-

tial of ($Re^{I*/0}$) **ReBPS-Y** is 600 mV higher than $Ru^{(III/II)}$ **RuBpy-Y**, and has a significant effect on the ETPT rate of tyrosine oxidation. In other words, the system has enough driving force to support facile tyrosine oxidation at all pHs and the subtle pathway selection between tyrosine and tyrosinate oxidation is not observed.

Table 2.5 k_{CS} charge separation rate constants (s^{-1}) of **ReBPS-Y** vs. **RuBpy-Y**.[13]

Photo-oxidant	E^0 (NHE)	pH 2.8	pH 7.2	pH 12.0
ReBPS-Y ($Re^{I*/0}$)	1.80 V	$0.81 \pm 0.03 \times 10^5$	$2.15 \pm 0.05 \times 10^5$	$2.00 \pm 0.04 \times 10^5$
RuBpy-Y ($Ru^{III/II}$)	1.3 V	$2.40 \pm 0.2 \times 10^3$	$1.21 \pm 0.07 \times 10^4$	$1.86 \pm 0.02 \times 10^{6a}$

[a] pH 10.34. [b] all rates in unit (s^{-1}).

In conclusion, the amino acid oxidation pathway in **ReBPS-AA** (AA = Y, W and WMe) has a major contribution from the ETPT pathway, but the CPET pathway contribution can account for the slight rate enhancement at higher pH for W. In the case of Y, the driving force for YH and Y– oxidation is sufficient that a significant difference between the pathways is not observed due to an overwhelming driving force.

2.3.2 ReBpy-AA (AA = F and W) System

The kinetics analysis (Eq. 2.1–2.3) described above is also applicable to analyze radical generation within the **ReBPS-AA** system. Though $^3[Re^I]$*(**ReBpy**) has enough potential, it cannot oxidize tryptophan and tyrosine (Figure 2.5). **RuBpy** Ru^{III} has a lower driving force, but a longer lifetime to oxidize W and Y.[13,33] In light of the potential conformational barrier to intramolecular oxidation, bimolecular quenching experiments were undertaken.[34] Comparing the quenching in the absence and in the presence of a quencher yields the following set of equations:

(Eq. 2.6) $$\Phi_f^0 = \frac{k_f}{k_f + k_d} = \frac{k_f}{1/\tau_0} = k_f \tau_0$$ In absence of quencher

(Eq. 2.7) $$\Phi_f = \frac{k_f}{k_f + k_d + k_q[Q]} = \frac{k_f}{k_q[Q] + 1/\tau_0}$$ In presence of quencher

(Eq. 2.8) $$\frac{\Phi_f^0}{\Phi_f} = \frac{\frac{k_f}{1/\tau_0}}{\frac{k_f}{k_q[Q]+1/\tau_0}} = 1 + k_q\tau_0[Q]$$

(Eq. 2.9) $$\frac{\Phi_f^0}{\Phi_f} = \frac{\tau_0}{\tau} = 1 + k_q\tau_0[Q]$$ Stern-Volmer Equation

Bimolecular quenching experiments with **RuBpy** (Scheme 2.1c) and **AcW** (N-acetyl-tryptophan) were reported to be pH independent at k_q = 2 × 10^9 $M^{-1}s^{-1}$ (pH= 3–12).[13] With **ReBpy-F**, the bimolecular quenching rates showed a linear correlation between [**AcW**] and $^3[Re^I]$* quenching. The observed long lifetime (~ 1.5 μs) of tryptophan radical (510 nm, pH = 7 and 12) and tryptophan radical cation (560 nm, pH = 2) suggests that the bimolecular charge re-combination is a slow process. The rate constants at different pHs were calculated to be 1.71 × 10^9 M^{-1} s^{-1} (pH = 12), 3.65 × 10^9 M^{-1} s^{-1} (pH = 7.2), and 9.14× 10^9 M^{-1} s^{-1} (pH = 2.8). The pH increase by 9 units resulted in a 5-fold increase in the k_q (Figure 2.6).[8]

It is noteworthy that the bimolecular quenching of $[Ru(dmb)_3]$ and $[Ru(bpy)_3]$ excited state by **AcW** was reported to proceed by ETPT pathway with a constant k_q across the pH 2 – 12.(Table 2.2).[15,16] As described earlier for **ReBPS**, the stronger photooxidant is more prone to proceed by the fast ETPT pathway. **ReBpy** system is a stronger photooxidant than $[Ru(bpy)_3]$ system by ~400 mV, suggesting the ETPT pathway for **ReBpy-F** and **AcW** bimolecular oxidation. PTET is unlikely due to high pK_a of indole at all pHs and the k_q has a weak dependence on pH (The 0^{th} order dependence). Thus, we concluded that ETPT pathway is mainly responsible for the observed k_q trend and the slight enhancement of CPET pathway responsible for the weak pH dependence like in **ReBPS-AA**.

2.4 Conclusion

A new water-soluble Re-based photooxidant system with appended amino acids was developed to investigate the PCET kinetics of W, Y and WMe radical generation in aqueous solution. The complex is soluble in aqueous media and has ample driving force to generate amino acid radicals. The PCET oxidation kinetics of tryptophan, 1-methyl tryptophan and tyrosine by the ^{3}MLCT of the Re excited state (^{3}[Re^I]*) were investigated by emission and nanosecond transient absorption spectroscopy over the pH range of 2–12. The radicals are generated by an apparent ETPT pathway as a result of the highly oxidizing ^{3}MLCT excited state of the **ReBPS** photooxidant. The potency and long lifetime of the **ReBPS-AA** photo-oxidant can oxidize tryptophan and tyrosine at all pHs, in contrast to **ReBpy-AA** system. **ReBpy-AA** system was unable to oxidize tryptophan over the pH range of 2–12 in a unimolecular manner even though it is a potent enough photooxidant. The successful observation of tryptophan oxidation in the bimolecular quenching study indicates that the fast charge recombination and/or the conformational limit can be responsible for lack of tryptophan oxidation in **ReBpy-W**.

2.5 Experimental Details

2.5.1 Materials and Methods

The ^{1}H NMR and ^{19}F NMR spectra were obtained using a Varian Mercury-400 NMR spectrometer at the Magnetic Resonance Facility of the Department of Chemistry and Chemical Biology at Harvard University. ESI-MS spectra were obtained using a Bruker microTOFII ESI LCMS in the same facility. The elemental analysis was obtained by Complete Analysis Laboratories.

L-Tyrosine methyl ester (Y-OMe), L-phenylalanine methyl ester hydrochloride (F-OMe•HCl), L-tryptophan methyl ester (W-OMe•HCl), isonicotinoyl chloride hydrochloride (Py-COCl•HCl), 1-methyl-L-tryptophan (1-Me-W-CO_2H), triethylamine (TEA, 99%), tetrabutylammonium (TBA) bisulfate, thionyl chloride ($SOCl_2$), bathophenanthrolinedisulfonic acid (BPS) disodium salt hydrate, methanol (MeOH, 99.5%), acetonitrile (MeCN, 99.9%), toluene (99.5%), ethyl acetate (EtOAc, 99.5%), dichloromethane (DCM, 99.5%), sodium sulfate (Na_2SO_4), tetrahydrofuran (THF, 99.5%), sodium bicarbonate ($NaHCO_3$), Amberlite IR120 H resin (Sigma Aldrich), d3-chloroform ($CDCl_3$), d4-methanol (CD_3OD), d3-acetonitrile (CD_3CN) (Cambridge Isotope Laboratories), silver tetrafluoroborate ($AgBF_4$), and pentacarbonylchlororhenium ($Re(CO)_5Cl$) (Strem) were used as received. (1-Me)-W-OMe was prepared with 1-Me-W-CO_2H. *fac*-[Re(1,10-bathophenanthroline sulphonate)$(CO)_3$MeCN]$(Bu_4N)_2(BF_4)$ (**ReBPS-MeCN**) was prepared as previously described.[23] **ReBpy-F** was prepared as published[5] and **ReBpy-W** was prepared the same way except that W-OtBu was used instead of F-OtBu.

Scheme 2.3 Synthesis of **ReBpy** system.

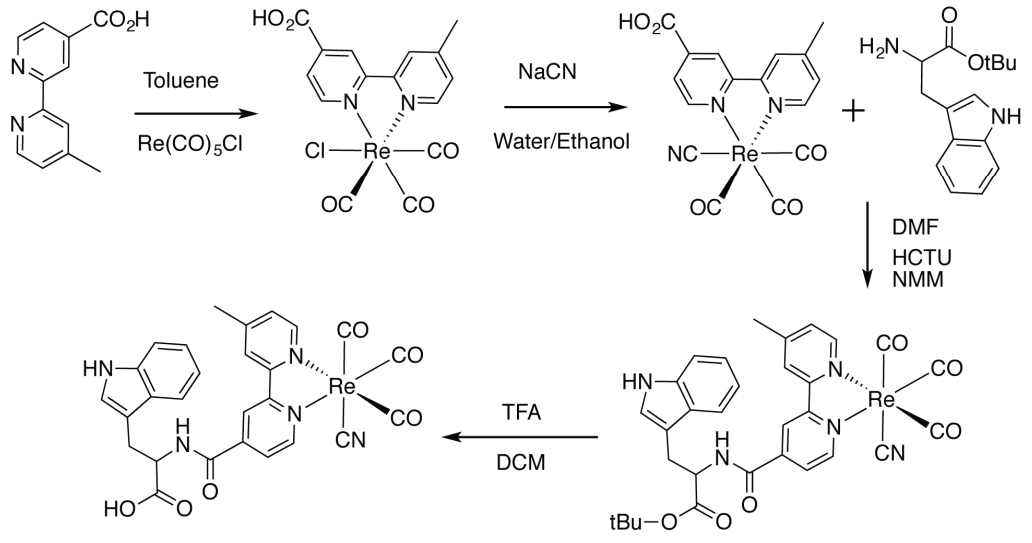

Scheme 2.4 Syntheses of (a) **ReBPS-AAs** and (b) **Py-AAs**.

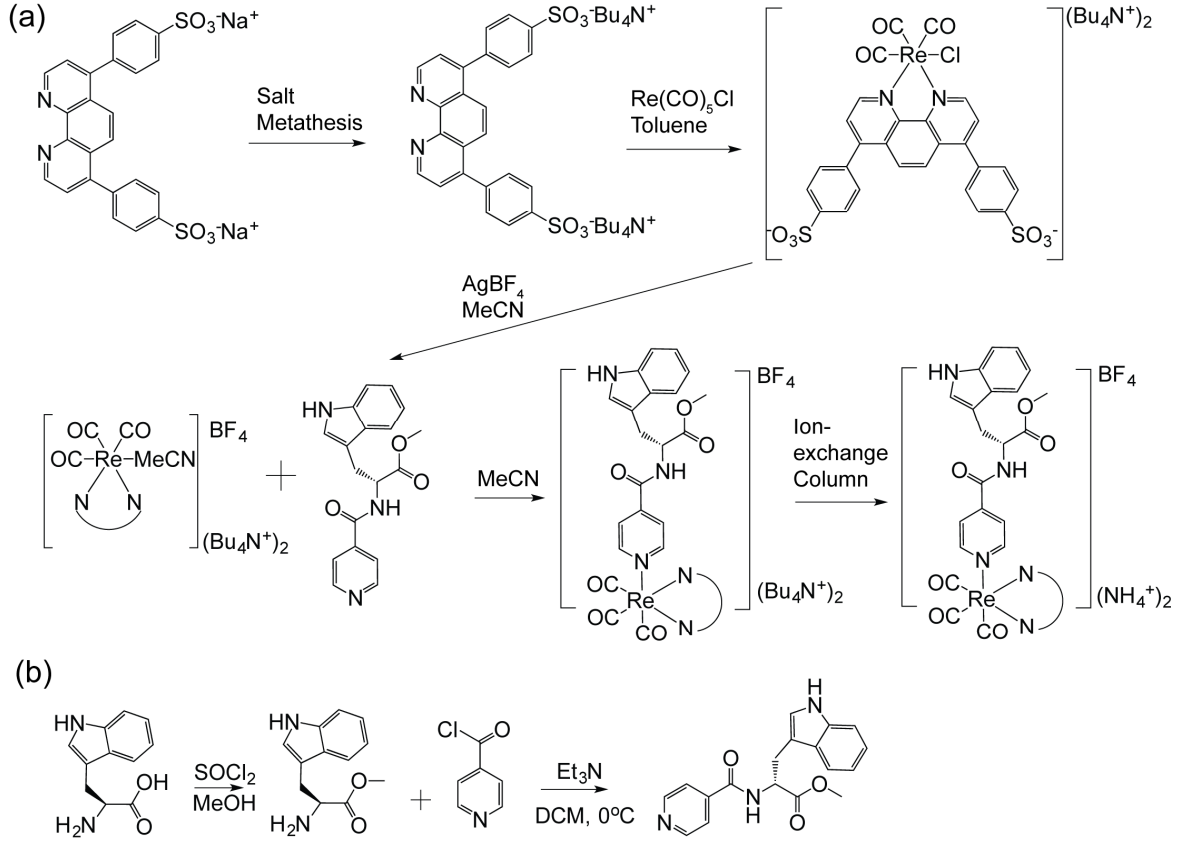

4-isonicotinoyl-L-AA (PyAA) (AA= amino acids methyl ester: F-OMe, Y-OMe, W-OMe, (1-Me)-W-OMe (WMe-OMe): The series of 4-isonicotinoyl-L-AAs was synthesized by following a reported procedure with a modification.[6] In a typical synthesis, 3 equiv. of TEA was added to a solution of 4.95 mmol of AA (1 equiv.) in DCM (300 mL) at 0 °C. One equiv. of Py-COCl•HCl was suspended in DCM (50 mL) and added dropwise to the solution of AA-OMe. The solution was stirred at 0 °C for 3 hours. The reaction mixture was washed sequentially with 1% $NaHCO_3$ (w/v in H_2O, 100 mL), 5% citric acid (w/v in H_2O, 100 mL), and H_2O (4 × 100 mL). The organic layer was dried over Na_2SO_4, filtered, and the solvent removed by rotary evaporation. The crude product was purified by flash chromatography (silica, DCM/ MeOH). The products were characterized by ^1H NMR and the spectra matched with the reported values (PyW, PyY and PyF). Yields of 70–95% were obtained for all PyAA analogues.

PyF: ^{1}H NMR (400 MHz, $CDCl_3$, 25 °C): δ = 8.53 (m, 2H, Py-H), 7.42 (m, 2H, Py-H), 7.26–7.06 (m, 5H, Ar-H), 4.82 (m, 1H, Cα-H), 3.73 (s, 3H, OCH_3), 3.48 (s, 3H, OCH_3), 3.10–3.02 (m, 2H, Cβ-H).

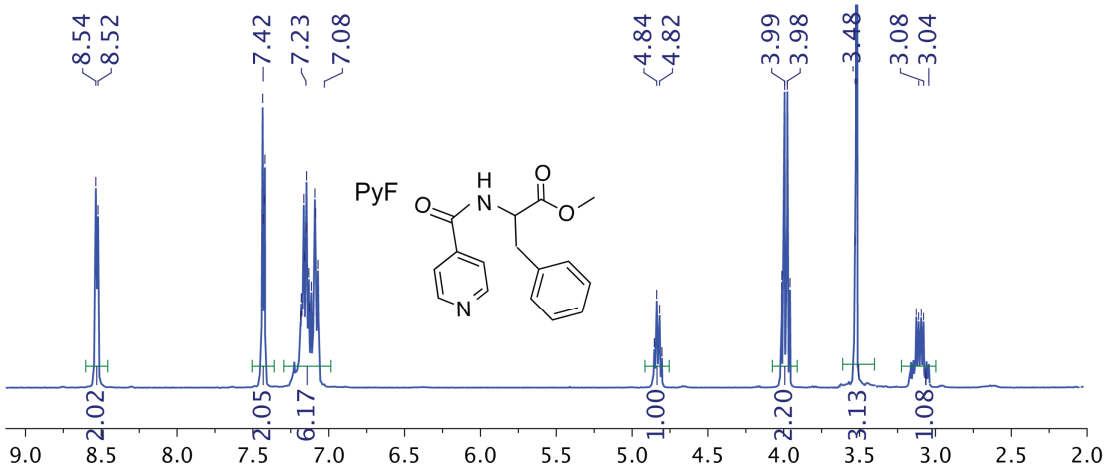

Figure 2.8 ^{1}H NMR spectrum of PyF in d_1-$CDCL_3$. The integration of peak at 7.22 ppm includes a solvent peak ($CHCl_3$). Peak at 3.98 ppm is a solvent peak (EtOAc).

PyY: ^{1}H NMR (400 MHz, CD_3OD, 25 °C): δ = 8.60 (m, 2H, Py-H), 7.63 (m, 2H, Py-H), 7.06 (d, 2H, Ar-H), 6.72 (d, 2H, Ar-H), 5.43 (d, 1H, amide), 4.82 (m, 1H, Cα-H), 3.34 (s, 3H, OCH_3), 3.02–2.96 (m, 2H, Cβ-H).

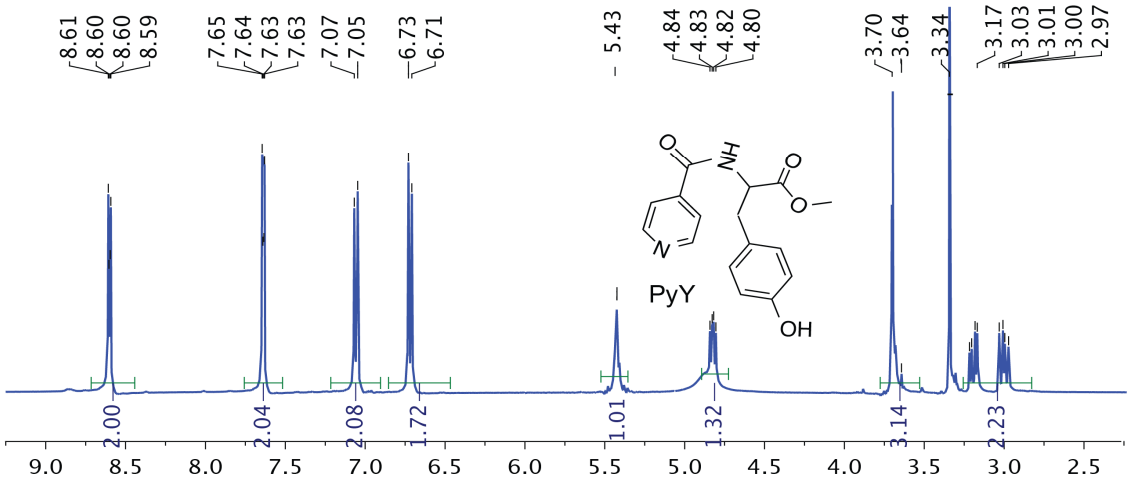

Figure 2.9 ^{1}H NMR spectrum of PyY in d_4-CD_3OD. Peak at 3.34 ppm is a solvent peak.

PyW: ^{1}H NMR (400 MHz, CD_3OD, 25 °C): δ = 8.61 (d, 2H, Py-H), 7.62 (d, 2H, Py-H), 7.53 (m, 1H, indole-H), 7.31 (m, 1H, indole-H), 7.10 (m, 1H, indole-H), 7.01–6.99 (m, 2H, indole-H), 4.93 (d, 1H, Cα-H), 3.72 (s, 3H, OCH_3), 3.46–3.30 (m, 2H, Cβ-H).

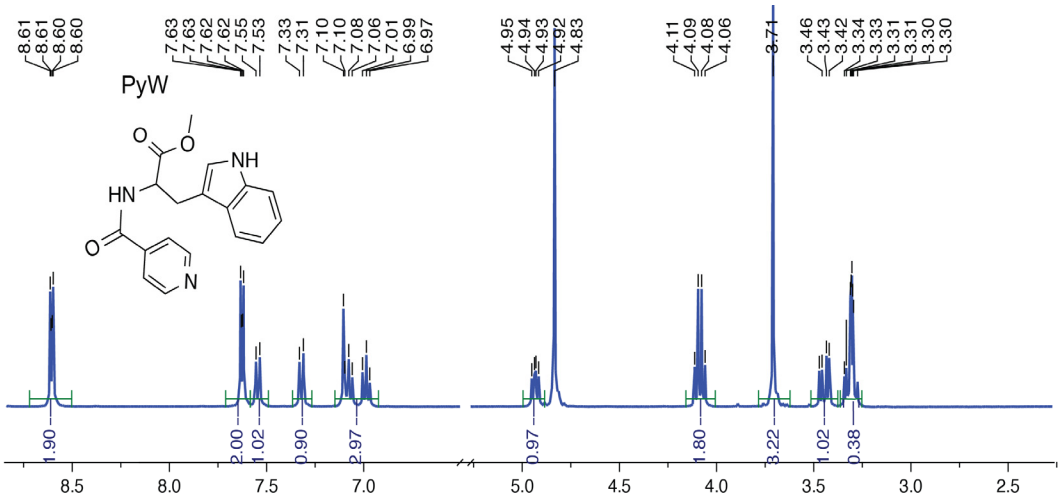

Figure 2.10 ^{1}H NMR spectrum of PyW in d_4-CD_3OD. Peak at 4.8 ppm (MeOH) and 4.09 (EtOAc) are solvent peaks.

WMe-OMe: ^{1}H NMR (400 MHz, CD_3OD, 25 °C): δ = 7.46 (m, 1H, indole-H), 7.30 (m, 1H, indole-H), 7.15 (m, 1H, indole-H), 7.03 (m, 2H, indole-H), 5.48 (d, 1H, amide), 4.23 (m, 1H, Cα-H), 3.73 (s, 3H, N-CH_3), 3.71 (s, 3H, OCH_3), 3.42–3.20 (m, 2H, Cβ-H).

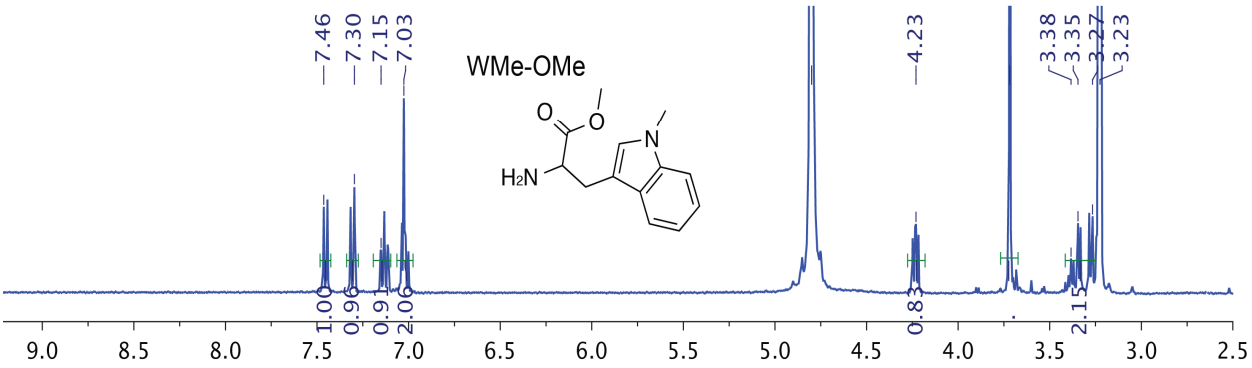

Figure 2.11 ^{1}H NMR spectrum of WMe-OMe in d_4-CD_3OD. Peaks at 4.7 and 3.3 ppm are solvent peaks.

Py(1-Me)W: ^{1}H NMR (400 MHz, CD_3OD, 25 °C): δ = 8.63 (d, 2H, Py-H), 7.65 (d, 2H, Py-H),

7.54 (m, 1H, indole-H), 7.32 (m, 1H, indole-H), 7.14 (m, 1H, indole-H), 7.03 (m, 2H, indole-H), 4.93 (m, 1H, Cα-H), 3.73 (s, 3H, N-CH_3), 3.71 (s, 3H, OCH_3), 3.42–3.20 (m, 2H, Cβ-H).

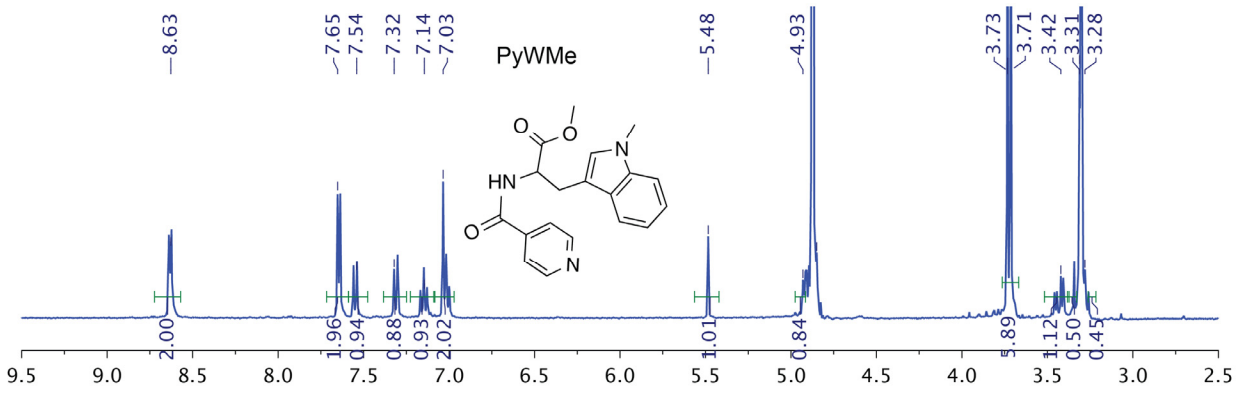

Figure 2.12 ^{1}H NMR spectrum of WMe-OMe in d$_4$-CD_3OD. Peaks at 4.7 and 3.3 are solvent peaks.

fac-[Re(1,10-bathophenanthroline sulphonate)$(CO)_3(CH_3CN)$]$(Bu_4N)_2(BF_4)$ (**ReBPS**-MeCN):

To a solution of *fac*-[Re(1,10-bathophenanthroline sulphonate)$(CO)_3$Cl]$(Bu_4N)_2$ (400 mg, 0.31 mmol) in acetonitrile (200 mL) was added $AgBF_4$ (486.2 mg, 2.49 mmol). The mixture was heated at reflux under nitrogen atmosphere in the dark overnight (~12 hrs). The solvent was removed in vacuum to yield a yellow solid. The crude solids were dissolved in a small amount of methanol and filtered to remove the excess $AgBF_4$ and the by-product AgCl. The filtrate was put under a high vacuum to yield yellow product (330 mg, 77.4 %). ^{1}H NMR (400 MHz, CD_3OD, 25°C): δ = 9.62–9.54 (m, 2H, BPS), 8.25 (s, 2H, BPS), 8.14-7.72 (m, 10H, BPS), 3.21(m, 16H, TBA), 2.16 (s, 3H, $NCCH_3$), 1.96 (m, 16H, TBA), 1.65 (m, 16H, TBA), 1.38 (m, 16H, TBA), 1.01 (m, 24H, TBA), ^{19}F NMR (400 MHz, CD_3OD, 25°C): δ = 153.89. Elemental analysis: Anal. Calcd. For [(**ReBPS**-MeCN)(BF_4)] $C_{29}H_{19}BF_4N_3O_9ReS_2^-$: C, 39.11; H, 2.15; N, 4.72; found C, 39.68; H, 2.78; N, 4.31.

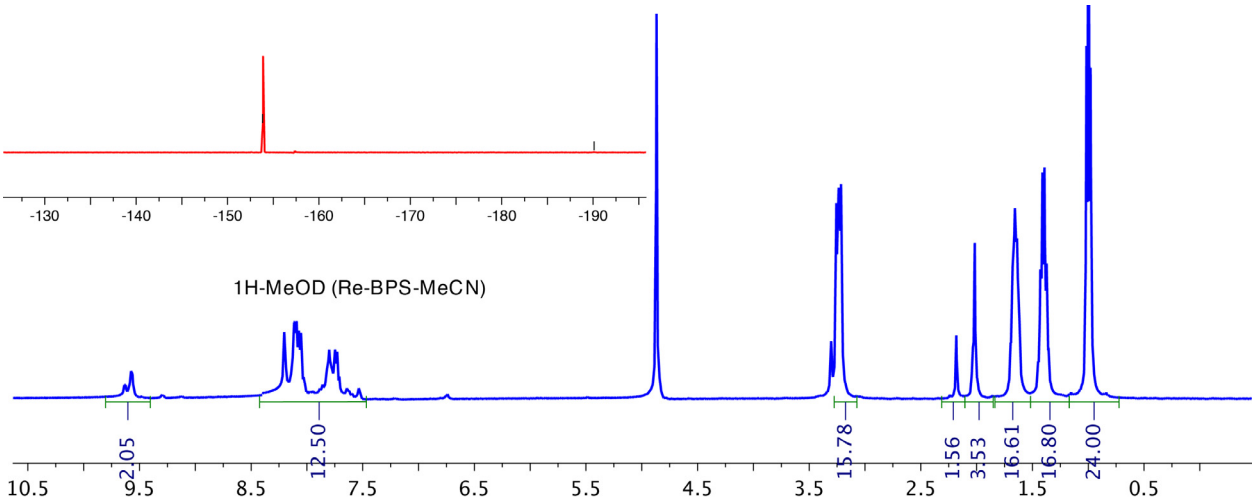

Figure 2.13 ^{1}H NMR spectrum (blue) and ^{19}F NMR spectrum (red) of **ReBPS**-MeCN in d_4-CD_3OD.

fac-[Re(1,10-bathophenanthroline sulphonate)$(CO)_3$(PyAA)]$(NH_4)_2(BF_4)$ (**ReBPS-AA**):

The series of *fac*-[Re(1,10-bathophenanthroline sulphonate)$(CO)_3$(AA)]$(NH_4)_2(BF_4)$ was synthesized by following a reported procedure.[23] In a typical synthesis, 1 equiv. of ReBPS-MeCN (200 mg, 0.145 mmol) was added to a solution of 5 equiv. of PyAA in MeCN (300 mL). The solution was heated at reflux under a nitrogen atmosphere for 2 days. The solvent was removed by rotary evaporation to yield a yellow solid. To remove excess PyAA, the yellow solid was dissolved in a minimal amount of MeOH and then diethyl ether was added until a precipitate was formed. The supernatant was removed carefully by syringe and the remaining slurry was dried under vacuum. TBA salts were changed into ammonium salts with an ion exchange column filled with Amberlite IR120H resin in its NH_4^+ form. The ion exchange column was prepared by following procedure. After washing with aqueous ammonia (NH_4Cl) several times, dilute aqueous NH_3 was used to remove excess chloride ion. The column was washed with deionized water then the product in a small amount of MeOH was loaded. The ion exchange column was eluted with MeOH and wa-

ter mixture 50% MeOH/water to 100% water). The yellow fraction was dried under vacuum to yield the product. The products were characterized by ^{1}H NMR and ESI-MS. Yields of 28-60 % were obtained for all **ReBPS-AA** analogues. The salt precipitated with one NH_4^+ group as the [NH_4^+][**ReBPS-AA**] compound.

fac-[Re(1,10-bathophenanthroline sulphonate)$(CO)_3$(PyF)](NH_4) (**ReBPS-F)**:

^{1}H NMR (400 MHz, CD_3OD, 25°C): δ = 9.72 (m, 2H, py-H), 8.86 (d, 2H, Py-H), 8.40–8.25 (m, 2H, BPS), 8.25 – 7.95 (m, 10H, BPS), 7.50 (m, 2H, BPS), 7.27–7.16 (m, 5H, F), 4.80 (m, 1H, Cα-H), 3.64 (s, 3H, OCH_3), 3.09 (m, 2H, Cβ-H). ^{19}F NMR (400 MHz, CD_3OD, 25°C): 154.83 (BF_4). *m/z* (ESI-MS) 1065.07 [**ReBPS-F**-H-NH_4]$^+$ (theoretical: 1064.13).

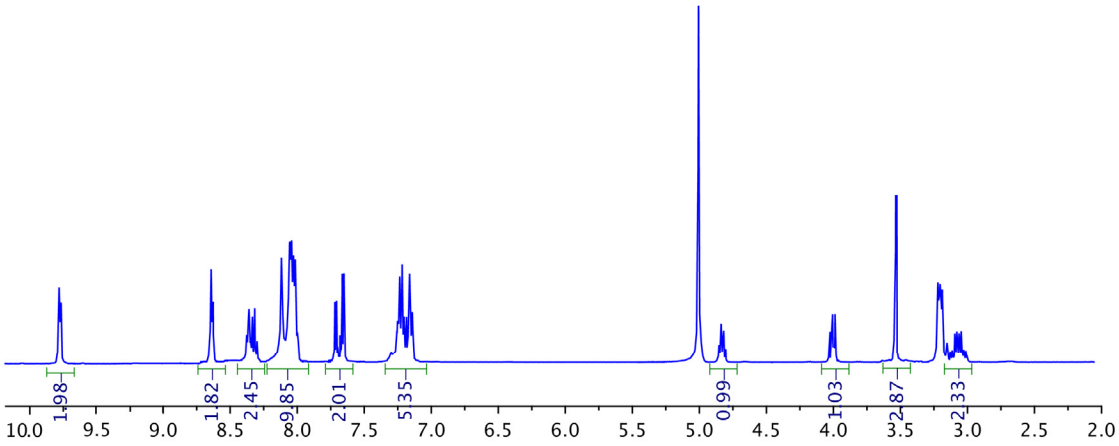

Figure 2.14 ^{1}H NMR spectrum of **ReBPS-F** in d_4-CD_3OD.

fac-[Re(1,10-bathophenanthroline sulphonate)$(CO)_3$(PyY)](NH_4) (**ReBPS-Y**):

^{1}H NMR (400 MHz, CD_3OD, 25°C): δ = 9.72 (m, 2H, Py-H), 8.75 (d, 2H, Py-H), 8.40–8.25 (m, 2H, BPS), 8.21 – 7.75 (m, 12H, BPS), 7.15 (d, 2H, Y), 6.75 (d, 2H, Y), 5.65 (s, 1H, 1H, amide-NH), 4.78 (m, 1H, Cα-H), 3.59 (s, 3H, OCH_3), 3.15 – 2.92 (m, 2H, Cβ-H). ^{19}F NMR (400 MHz,

CD_3OD, 25°C): δ =154.33 (d, BF_4). m/z (ESI-MS) 1064.10 [**ReBPS-Y**-H-NH_4]$^+$.

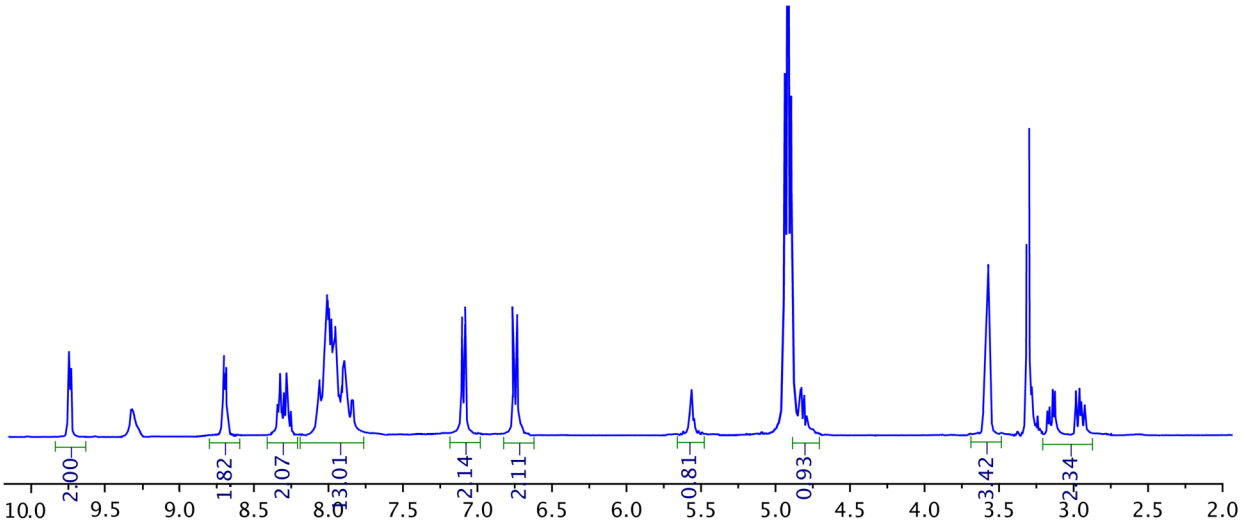

Figure 2.15 ^{1}H NMR spectrum of **ReBPS-Y** in d$_4$-CD_3OD.

fac-[Re(1,10-bathophenanthroline sulphonate)$(CO)_3$(PyW)](NH_4) (**ReBPS-W**):

^{1}H NMR (400 MHz, CD_3OD, 25°C): δ = 9.76 (m, 2H, BPS), 8.60 (d, 2H, Py-H), 8.22 – 8.04 (m, 8H, BPS, Py-H), 7.72 (m, 5H, BPS), 7.32 (m, 1H, W), 7.19(m, 1H, W), 6.97 – 6.82 (m, 2H, W), 6.74 (m, 1H, W), 4.62 (m, 1H, Cα-H), 3.72 (s, 3H, OCH_3), 3.46–3.30 (m, 2H, Cβ-H). *m/z* (ESI-MS): 1086.12 [**ReBPS-W**-H_2]$^+$, 1108.19 [**ReBPS-W**-H-Na]$^+$. Elemental analysis: Anal. Calcd. For [(**ReBPS-W**)(NH_4)] $C_{45}H_{35}N_6O_{23}ReS_2^-$: C, 49.04; H, 3.20; N, 7.63; found C, 49.35; H, 4.97; N, 6.25.

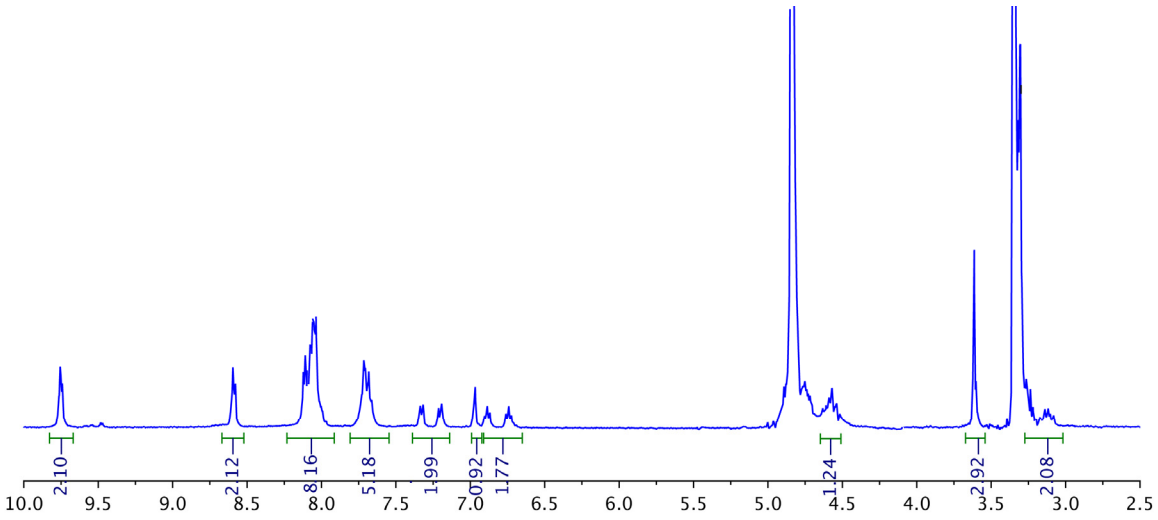

Figure 2.16 ^{1}H NMR spectrum of **ReBPS-W** in d$_4$-CD$_3$OD. Peaks at 4.80 and 3.31 ppm are solvent peaks (MeOH)

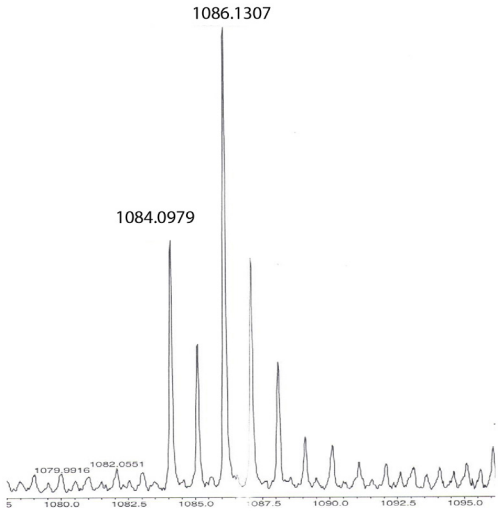

Figure 2.17 Rhenium isotope pattern in ESI-MS **ReBPS-W**: M; 100.0%, M–2; 59.7%, M+1; 46.5 %, M–1; 27.8 %.

fac-[Re(1,10-bathophenanthroline sulphonate)(CO)$_3$(PyWMe)](NH$_4$) (**ReBPS-WMe**):

^{1}H NMR (400 MHz, CD$_3$OD, 25°C): δ = 9.75 (m, 2H, BPS), 8.68 (m, 2H, Py-H), 8.20 – 8.04 (m, 8H, BPS), 7.68 (m, 4H, BPS), 7.46 (m, 2H, Py-H), 7.30 (m, 2H, Py-H), 6.98 (m, 1H, WMe), 6.78 (m, 1H, WMe), 6.65 (m, 2H, WMe), 4.88 (m, 1H, Cα-H), 3.62 (2, 6H, N-CH$_3$, OCH$_3$), 3.26 – 3.22 (m, 2H, Cβ-H). *m/z* (ESI-MS): 1117.24 [**ReBPS-WMe**-NH$_4$-H]$^{+}$. Elemental analysis: Anal. Calcd. For [(**ReBPS-WMe**)(NH$_4$)] C$_{46}$H$_{37}$N$_6$O$_{23}$ReS$_2^{-}$: C, 49.50; H, 3.34; N, 7.53; found C, 49.36; H, 5.01; N, 6.14.

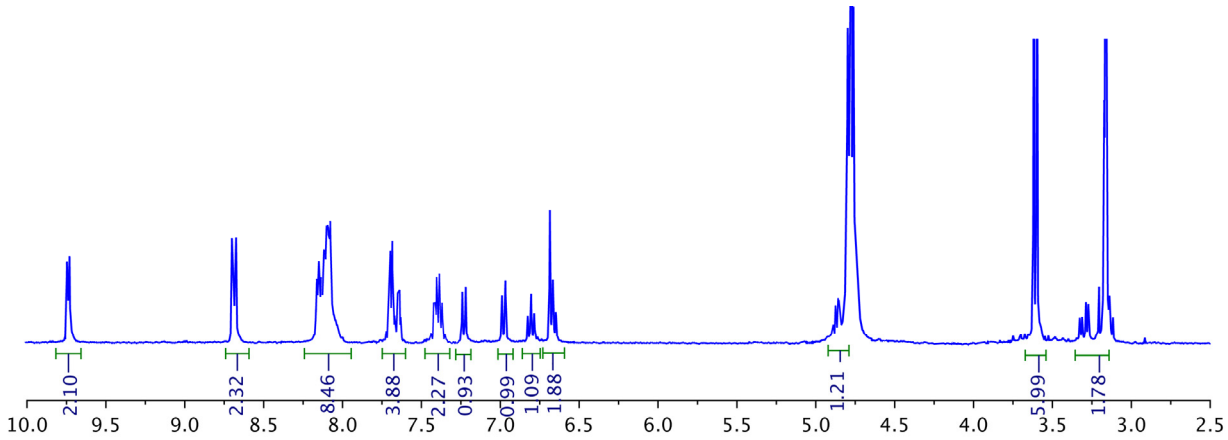

Figure 2.18 ^{1}H NMR spectrum of **ReBPS-WMe** in d$_4$-CD$_3$OD. Peaks at 4.78 ppm and 3.31 ppm are solvent peaks (MeOH).

Tricarbonylcyano(4'-methyl-2,2'-bipyridine-4-phenylalanine)rhenium(I) (**ReBpy-F**):

^{1}H NMR (400 MHz, CD$_3$OD, 25°C): δ = 9.14 (m, 1H, bpy-H), 8.89 (m, 1H, bpy-H), 8.79 (m, 1H, bpy-H), 8.49 (m, 1H, bpy-H), 7.86 (m, 1H, bpy-H), 7.57 (m, 1H, bpy-H), 7.30 (m, 6H, F-ph), 4.96 (m, 1H, F-CH), 3.13 (m, 2H, F-CH$_2$), 2.64 (s, 3H, bpy-CH$_3$).

Tricarbonylcyano(4'-methyl-2,2'-bipyridine-4-tryptophane)rhenium(I) (**ReBpy-W**):

^{1}H NMR (400 MHz, CD$_3$OD, 25°C): δ = 9.13 (m, 1H, bpy-H), 8.89 (m, 1H, bpy-H), 8.68–8.63 (m, 1H, W), 8.34 (m, 1H, bpy-H), 7.87 (m, 1H, bpy-H), 7.55 (m, 2H, bpy-H, W), 7.35 (m, 1H, W), 7.14 (m, 1H, W), 7.08 (m, 1H, W), 6.98 (m, 1H, W), 4.94 (m, 1H, W-CH), 3.15 (m, 2H, W-CH$_2$), 2.64 (s, 3H, bpy-CH$_3$). Elemental analysis: Anal. Calcd. For $C_{27}H_{20}N_5O_6Re$: C, 46.55; H, 2.89; N, 10.05; found C, 46.23; H, 2.92; N, 10.13.

2.5.2 Steady State Emission Measurement

Steady-state emission data were collected using a PTI QM 4 Fluorometer equipped with a 150 W Xe-arc lamp for excitation and a Hamamatsu R928 photomultiplier tube cooled to –78 °C

for detection. Samples were dissolved to a dilute solution (10 – 50 μM) and a 6Q quartz 1 cm path length cell was used for emission experiments.

2.5.3 Latimer Diagram of ReBPS-F

ReBPS-F was dissolved to 100 μM concentration in dry 0.1 M $TBAPF_6$ CH_3CN solution under nitrogen. The E^0 ($Re^{I/0}$) reduction potential was determined from differential pulse voltammetry (DPV) measurements using a platinum disk working electrode, a Ag/AgCl reference electrode, and a platinum wire counter electrode. The Latimer diagram was constructed in acetonitrile, as water did not provide an electrochemical window large enough to accommodate the redox chemistry of the complex. The measured $Re^{I/0}$ couple was –1.37 V vs. NHE (– 0.72 vs. Fc^+/Fc). The steady state emission spectrum at 77 K did not resolve E_{00}. To estimate an accurate excited state energy, the emission band fitting method was used following published procedures.[29] Parameters obtained were fitted using a Frank-Condon analysis:[35,36]

$$I(\bar{\nu}) = \sum_{n}^{5} \left(\frac{E_{00} - n\hbar\omega}{E_{00}}\right)^3 \left(\frac{S^n}{n!}\right) \exp\left[-4\ln 2\left(\frac{\bar{\nu} - E_{00} + n\hbar\omega}{\Delta\bar{\nu}_{1/2}}\right)^2\right]$$

where $I(\bar{\nu})$is the emission intensity in quanta, S is the dimensionless Huang-Rhys factor, ħω is the vibrational energy spacing, and $\Delta\bar{\nu}_{1/2}$ is the bandwidth. With ħω = 8.5 × 10^2 cm^{-1}, $\Delta\bar{\nu}_{1/2}$== 1.19 × 10^3 cm^{-1}, S = 2.757, the value of E_{00} was 1.93 × 10^4 cm^{-1}.

2.5.4 Ground State Electronic Absorption Measurement

UV-vis spectra were recorded on a Varian Cary 5000 UV-vis-NIR spectrophotometer using a 1 cm path length 6Q quartz Starna spectroscopy cell with 10 – 50 μM analyte solution

2.5.5 Laser Spectroscopy

Nanosecond timescale laser spectroscopy experiments utilized a system that has been reported.[17] For the experiments reported in this chapter, a few modifications were made. First, the 500 nm blaze grating (300 grooves/mm) was used for emission kinetics measurements and the 250 nm blaze grating (300 grooves/mm) was used for all transient absorption experiments. All experiments were performed at room temperature and the emission lifetime was averaged over 3 measurements. Time-resolved emission and transient absorption (TA) measurement samples were flowed without recirculation to prevent interference from decomposition products. Both **ReBpy-AA** and **ReBPS-AA** samples were 50 μM in 50 mM phosphate buffer.[14] **ReBpy-AA** sample solutions were freeze-pump-thaw degassed to 10^{-5} Torr and **ReBPS-AA** sample solutions were bubbled with Ar for 30 minutes prior to the TA experiment and were flowed once through to obtain clear kinetics data without interference from potential photochemical decomposition products. TA spectra reported are an average of 1000 four-spectrum sequences; for time-resolved emission experiments, individual traces are an average of 1000 sweeps.

2.6 References

(1) Reece, S. Y.; Nocera, D. G. *Annu. Rev. Biochem.* **2009**, *78*, 673.

(2) Gagliardi, C. J.; Westlake, B. C.; Kent, C. A.; Paul, J. J.; Papanikolas, J. M.; Meyer, T. J. *Coord. Chem. Rev.* **2010**, *254*, 2459.

(3) Hammes-Schiffer, S. *Energy Environ. Sci.* **2012**, *5*, 7696.

(4) M. R. DeFelippis, C. P. Murthy, F. Broitman, D. Weinraub, M. Faraggi, M. H. Klapper *J. Phys. Chem.* **1991**, *95*, 3416.

(5) a) Reece, S. Y.; Nocera, D. G. *J. Am. Chem. Soc.* **2005**, *127*, 9448. b) Reece, S. Y.; Seyedsayamdost, M. R.; Stubbe, J.; Nocera, D. G. *J. Am. Chem. Soc.* **2006**, *128*, 13654.

(6) Pizano, A. A.; Yang, J. L.; Nocera, D. G. *Chem. Sci.* **2012**, *3*, 2457.

(7) a) Costentin, C.; Louault, C.; Robert, M.; Savéant, J.-M. *Proc. Natl. Acad. Sci. U.S.A.* **2009**, *106*, 18143. b) Bonin, J.; Costentin, C.; Robert, M.; Routeir, M.; Savéant, J.-M. *J. Am. Chem. Soc.* **2013**, *135*, 14359.

(8) Zhang, M. T.; Nilsson, J.; Hammarström, L. *Energy Environ. Sci.* **2012**, *5*, 7732.

(9) Gagliardi, C. J.; Binstead, R. A.; Thorp, H. H.; Meyer, T. J. *J. Am. Chem. Soc.* **2011**, *133*, 19594.

(10) a) Stubbe, J.; Nocera, D. G.; Yee, C. S.; Chang, M. C. Y. *Chem. Rev.* **2003**, *103*, 2167. b) Stubbe, J.; van der Donk, W. A. *Chem. Rev.* **1998**, *98*, 705.

(11) Huynh, M. H. V; Meyer, T. J. *Chem. Rev.* **2007**, *107*, 5004.

(12) Uhlin, U.; Eklund, H. *Nature* **1994**, *370*, 533.

(13) Irebo, T.; Zhang, M. T.; Markle, T. F.; Scott, A. M.; Hammarström, L. *J. Am. Chem. Soc.* **2012**, *134*, 16247.

(14) Irebo, T.; Reece, S. Y.; Sjödin, M.; Nocera, D. G.; Hammarström, L. *J. Am. Chem. Soc.* **2007**, *129,* 15462.

(15) Zhang, M. T.; Irebo, T.; Johansson, O.; Hammarström, L. *J. Am. Chem. Soc.* **2011**, *133*, 13224.

(16) Bonin, J.; Costentin, C.; Robert, M.; Routier, M.; Savéant, J.-M. *J. Am. Chem. Soc.* **2013**, *135*, 14359.

(17) Pizano, A. A.; Lutterman, D. A.; Holder, P. G.; Teets, T. S.; Stubbe, J.; Nocera, D. G. *Proc. Natl. Acad. Sci.* **2012**, *109*, 39.

(18) Holder, P. G.; Pizano, A. A.; Anderson, B. L.; Stubbe, J.; Nocera, D. G. *J. Am. Chem. Soc.* **2012**, *134*, 1172.

(19) Hackett, J. W.; Turro, C. *J. Phys. Chem. A,* **1998**, *102*, 5728.

(20) Dattelbaum, D. M.; Omberg, K. M.; Schoonover, J. R.; Martin, R. L.; Meyer, T. J. *Inorg. Chem.* **2002**, *41*, 6071.

(21) Guthrie, J. P. *Can. J. Chem.* **1978**, *56*, 2342.

(22) Lauz, M.; Eckhardt, S.; Fromm, K. M.; Giese, B. *Phys. Chem. Chem. Phys.* **2012**, *14*, 13785.

(23) Amoroso, J.; Coogan, M. P.; Dunne, J. E.; Fernández-Moreira, V.; Hess, J. B.; Hayes, A. J.; Lloyd, D.; Millet, C.; Pope, S. J. A.; Williams, C. *Chem. Commun*. **2007**, *29*, 3066.

(24) Santus, R.; Bazin, M.; Aubailly, M.; Guermonprez, R. *Photochem. Photobiol*. **1972**, *15*, 61.

(25) D'Elia, L. F.; Ortiz, R. L. *J. Electrochem. Soc*. **2006**, *153*, D187

(26) Pizano, A. A.; Olshansky, L.; Holder, P. G.; Stubbe, J.; Nocera, D. G. *J. Am. Chem. Soc.* **2013**, *135*, 13250.

(27) Pascaly, M.; Yoo, J.; Barton, J. K. *J. Am. Chem. Soc.* **2002**, *124*, 9083.

(28) Chen, P.; Meyer, T. J. *Chem. Rev.* **1998**, *98*, 1439.

(29) Anderson, B. L.; Maher, A. G.; Nava, M.; Lopez, N.; Cummins, C. C.; Nocera, D. G. *J. Phys. Chem. B* **2015**, *119*, 7422.

(30) Tommos, C.; Skalicky, J. J.; Pilloud, D. L.; Wand, A. J.; Dutton, P. L. *Biochemistry* **1999**, *38*, 9495.

(31) Neta, P.; Huie, R. E.; Ross, A. B. *J. Phys. Chem. Ref. Data* **1988**, *17*, 1027.

(32) Olshansky, L.; Finkbeiner, C.; Koo, B.; Stubbe, J.; Nocera, D. G. *J. Am. Chem. Soc.,* submitted for the publication.

(33) Dongare, P.; Maji, S.; Hammarström, L. *J. Am. Chem. Soc.* **2016**, *138*, 2194.

(34) Cukier, R. I.; Nocera, D. G. *Annu. Rev. Phys. Chem.* **1998**, *49*, 337.

(35) Kober, E. M.; Caspar, J. V.; Lumpkin, R.S.; Meyer, T. J. *J. Phys. Chem.* **1986**, *90*, 3722.

(36) Striplin, D. R.; Reece, S. Y.; McCafferty, D. G.; Wall, C. G.; Friesen, D. A.; Erickson, B. W. Meyer, T. J. *J. Am. Chem. Soc.* **2004**, *126*, 5282.

Chapter 3 –

Modulation of Phenol Oxidation in Cofacial Dyads

Portions of this chapter have been published:

Koo, B.; Huynh, M.; Halbach, R. L.; Stubbe, J.; Nocera, D. G. *J. Am. Chem. Soc*. **2015**, *137*, 11860[1]

3.1 Introduction

Amino acid radicals play an essential role in the biochemistry of metabolism and catalysis.[2] Under physiological conditions, the generation and transport of amino acid radicals requires the coupling of a proton and an electron. The prominence of proton-coupled electron transfer (PCET) is arguably nowhere better exemplified than in *E. coli* class *Ia* ribonucleotide reductase (RNR), which catalyzes the reduction of nucleoside diphosphates to deoxynucleoside diphosphates.[3–5] RNR function relies on reversibly transferring a radical over a ~35 Å pathway between the amino acid, Y_{122} in β2 and C_{439} in α2 of *E. coli* class *Ia* RNR. The proposed pathway, for both forward and backward transfer, is β-Y_{122} ⇄ β-Y_{356} ⇄ α-Y_{731} ⇄ α-Y_{730} ⇄ α-C_{439}.[2–4] Radical injection from β-Y_{356} into Y_{731} of the α2 subunit is facilitated by the presence of adjacent Y_{730} (Figure 3.1).[6,7]

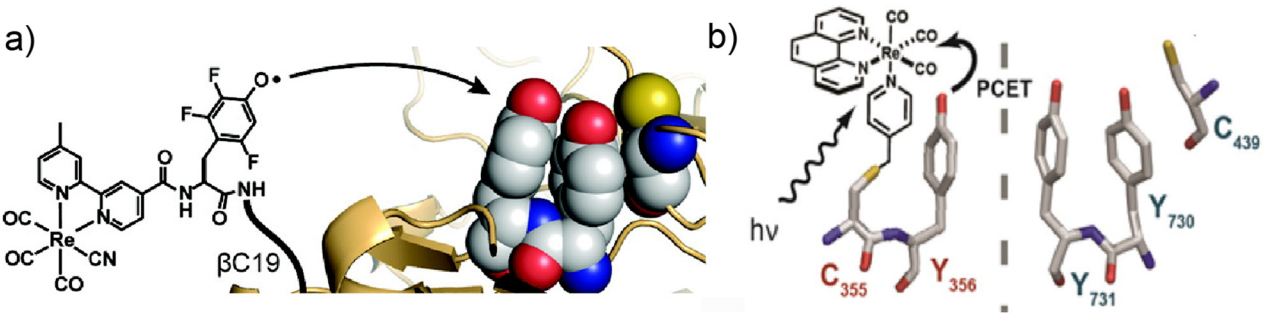

Figure 3.1 PhotoRNR studies that suggest the unique redox cooperativity of the Y_{731}−Y_{730} dyad. a) Point mutations that disrupt the Y_{731}−Y_{730} dyad shut down radical transport.[6] b) The rate of Y_{356} oxidation depends on the presence of Y_{731} across the interface.[7]

This result suggests that the dyad of two tyrosines does not simply provide two sequential radical pathway steps but that there is a collective property of two tyrosines, Y_{730} and Y_{731}. Whereas the oxidation kinetics of a phenol, the side chain of tyrosine, have been thoroughly studied by photochemical, electrochemical, and radiochemical methods in the context of PCET,[8–14] the redox chemistry of π-stacked, cofacially-aligned phenol dyads is unknown.

In much the same way that the potential of guanines is perturbed by the presence of a neighboring guanine in DNA,[15,16] we wondered whether the potential of tyrosine is affected by the presence of a neighboring tyrosine. To address this issue, we have prepared the models shown in Scheme 3.1. Two phenols may be cofacially positioned at a fixed distance from a 2,7-di-tert-butyl-4,5-di(4-hydroxyphenyl)-9,9-dimethylxanthene backbone (**DPX**). We have also developed control model systems **FPX** and **MPX** (Scheme 3.1) to allow the π-interaction between neighboring phenol units to be assessed. Electrochemical studies together with computational results establish that the phenol oxidation potential is perturbed within dyad **DPX** as compared to **FPX** and **MPX**. The perturbation in the redox potential has significant implications to the PCET pathway of RNR.

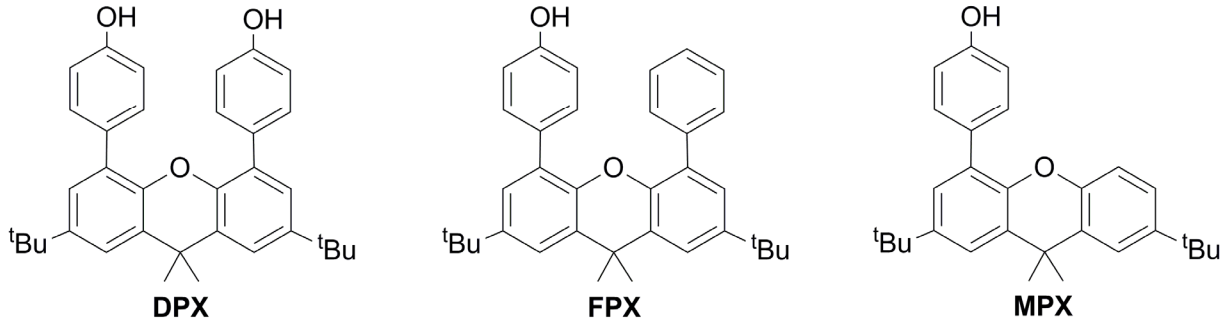

Scheme 3.1 Stacked phenol and control systems for modeling the tyrosine dyad in RNR.

3.2 Results

3.2.1 Synthesis

Model systems **DPX**, **FPX** and **MPX** were synthesized at a high yield (~70%) by Suzuki cross-coupling. The sequential cross coupling afforded the final asymmetric model systems. Bromo-aryl and phenyl boronic acid did not couple well, therefore phenyl boronic acid pinacol ester was used instead. Column chromatography was performed on a Biotage column chroma-

tography instrument. The products were characterized by NMR spectroscopy and ESI-MS for purity and identity.

3.2.2 X-ray Crystallography

X-ray crystallography shows that two phenols are cofacially arranged, akin to the Y_{731} and Y_{730} arrangement in RNR.[17] The O···O distance between phenols is 4.35 Å, the centroid distance is 4.41 Å and the distance of intermolecular oxygen-oxygen distance is 2.72 Å (Figure 3.2). The X-ray structure also suggests that intramolecular hydrogen-bonding may occur and form a homo-conjugates in solution. The side view shows that the phenol moieties placed parallel to each other and out of the plane of xanthene backbone.

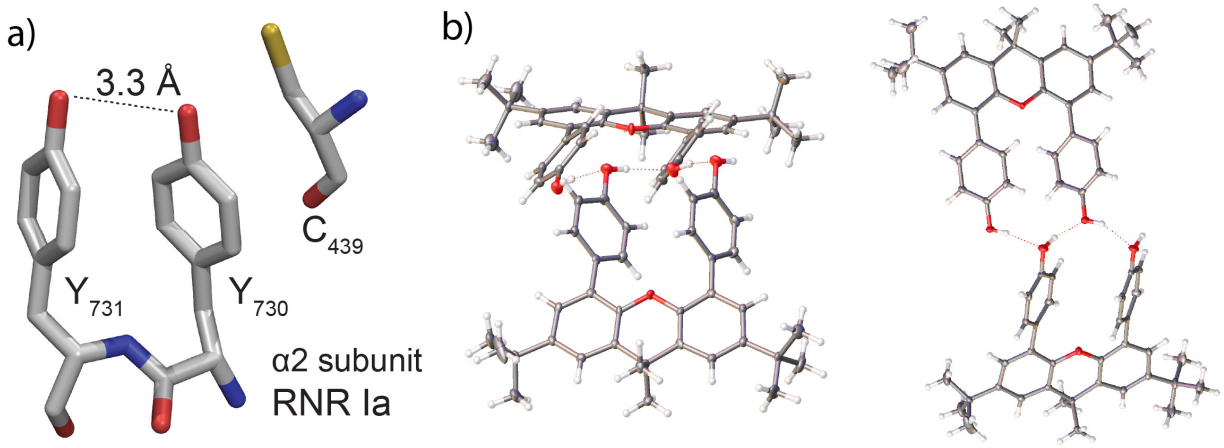

Figure 3.2 a) Y_{731} and Y_{730} in α2 from protein crystal structure 4R1R. b) X-ray crystallography structure of **DPX**: oxygen (red) carbon (grey) hydrogen (white). The side view shows the phenol moieties placed parallel to each other and out of the plane of xanthene backbone.

3.2.3 Electrochemistry - Cyclic Voltammetry

The CVs of the mono-phenol systems **FPX** and **MPX** in acetonitrile show a single peak (peak **IV** and peak **V**, respectively, in Figure 3.3). Using the xanthene backbone peak as an inter-

nal one-electron redox reference, both **MPX** and **FPX** show that the total charge passed during phenol oxidation corresponds to two-electron processes.

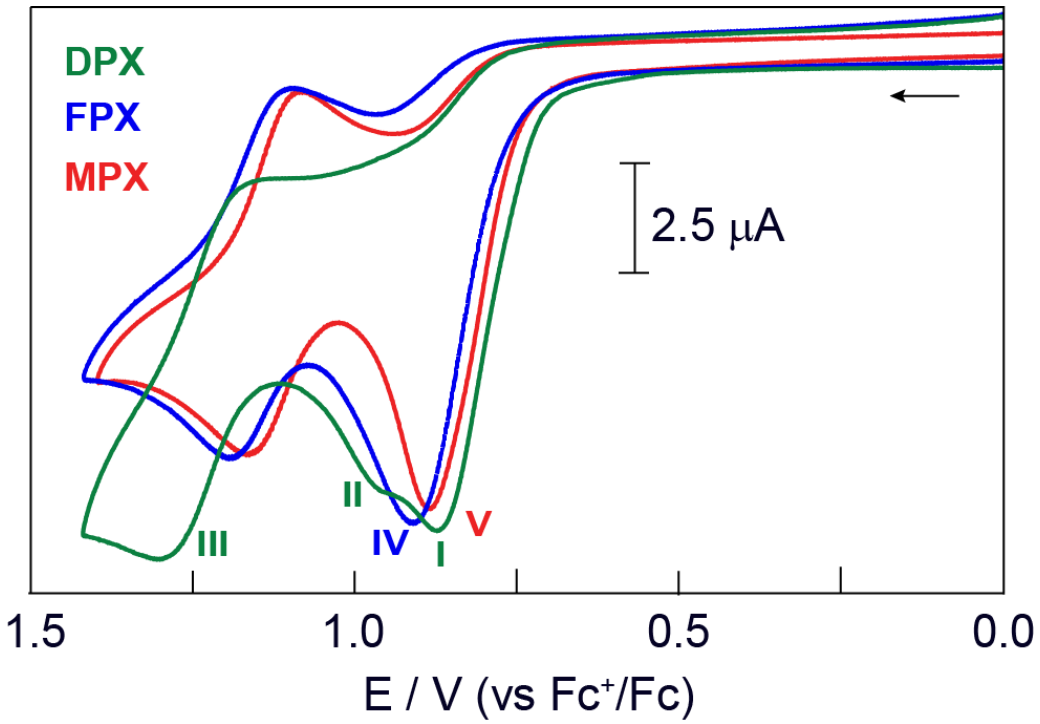

Figure 3.3 Cyclic voltammograms of **DPX** (green), **FPX** (blue), and **MPX** (red). The peak potentials of peaks **I**, **II**, **III**, **IV**, and **V** are 0.88 V, 0.98 V, 1.29 V, 0.92 V, and 0.89 V, respectively. All CVs in the chapter were taken in 0.5 mM analyte, 0.1 M $TBAPF_6$ electrolyte in dry acetonitrile solution with a Pt working electrode, a Pt wire electrode, a Ag wire pseudo reference electrode, and referenced to Fc^+/Fc.

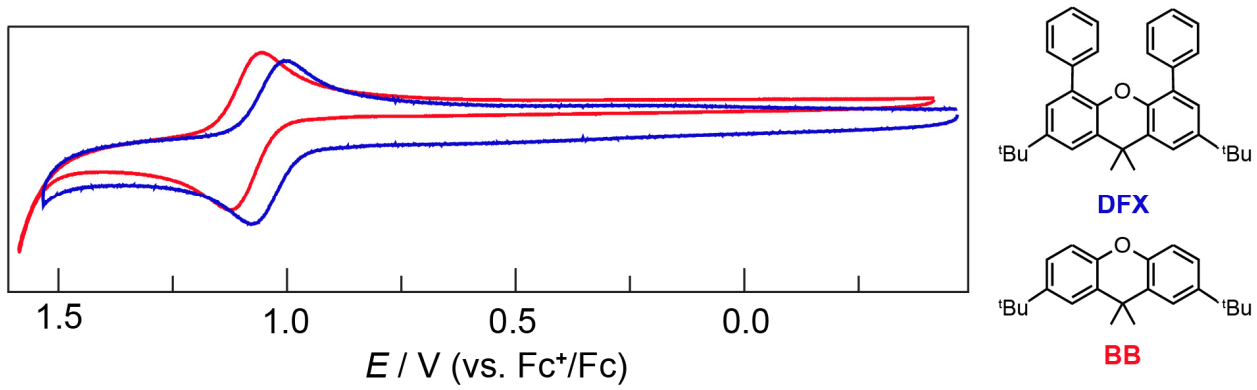

Figure 3.4 Cyclic voltammograms of reversible one-electron oxidation of xanthene backbones: **BB** (red) and **DFX** (blue).

A wave centered at 1.12 V is consistent with the one-electron chemically reversible oxidation of the xanthene backbone; this oxidation does not interfere the phenol oxidation as shown by electrochemical analysis of various substituted xanthenes with phenyl analogues (Figure 3.4). In contrast to the single two-electron ECE (electron transfer –chemical step–electron transfer) wave for phenol oxidation in **MPX** (and **FPX**), the CV of **DPX** shows two oxidation peaks at 0.88 V and 0.98 V (peaks **I** and **II** in Figure 3.3, respectively), with the xanthene oxidation peak centered at 1.23 V. The total charge associated with the two waves corresponds to a two-electron process, as references to the one-electron xanthene wave.

3.2.4 Concentration Dependence of CV

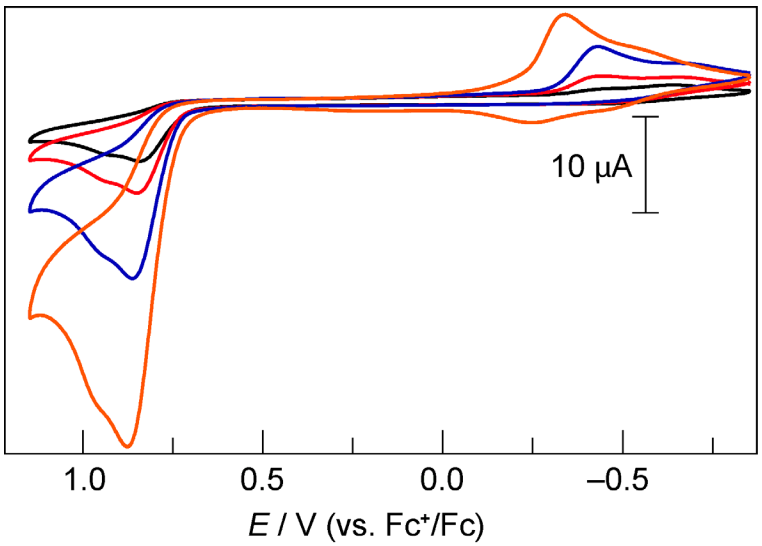

Figure 3.5 Cyclic voltammetry of **DPX** at varying concentrations: 0.3 mM (black), 0.5 mM (red), 0.8 mM (blue), and 1.4 mM (orange).

As shown in the X-ray crystallography structure of Figure 3.2b, **DPX** may form homo-conjugate dimer held by intramolecular hydrogen-bonding in solution. The dimeric conjugation may complicate the interpretation of the CV data. Thus the concentration dependence of the peak potentials and ratio of peak amplitudes were measured (Figure 3.5). The peak potentials and ratio

of peak amplitudes were invariant over a concentration range of 0.1–5 mM, confirming that the CV characteristics are not a result of an intermolecular interaction.

3.2.5 Scan Rate Dependence of CV

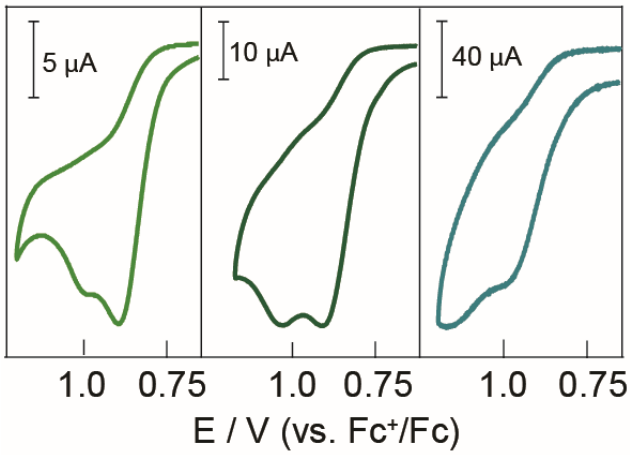

Figure 3.6 Scan rate dependence of **DPX**: peak **I** and peak **II** amplitudes at 0.1 V/s (left, green), 1 V/s (middle, dark green), 10 V/s (right, emerald). Peak **I** and **II** exhibit a peak potential dependence on scan rate of ~60 mV/decade, suggesting the coupling of a chemical step with each electron transfer step.

The CV peak feature results from k_{et} (heterogeneous electron transfer rate constant) and k_d (diffusion coefficient). The varying scan rate dependence of the CV feature indicates that there is a chemical event following the electrochemical event, as does the irreversibility of the waves. CV features **I** and **II** both exhibit a peak potential dependence on scan rate of ~60 mV/decade (Figure 3.6). The electrochemical process associated with the irreversible process of peak **I** and **II** are fast as indicated by the inability to achieve a reversible (quasi-irreversible) wave, even at the fastest scan rates.

3.2.6 UV-vis Spectra of DPX and MPX with Base Titration

The relative acidity and the phenolate absorption features of phenol moieties in **DPX** and **MPX** were measured with TBAOH titration. **MPX** shows an isosbestic point was observed at 280 nm while DPX does not show an overall isosbestic point. The deprotonation of **DPX** may proceed from **DPX** to mono-deprotonated, then to fully deprotonated **DPX**. Full deprotonation of **DPX** did not result in increased amplitude of the phenolate absorption peak identified in **MPX** (~325 nm). This observation implies that the phenolates of **DPX** have a distinct electronic interaction, resulting in the resolved ground state absorption features. The 250 nm peak of **MPX** was broadened from the 254 nm peak of **DPX**. The phenol moieties of **DPX** are locked into a conformation with a smaller degree of freedom, perpendicular to the xanthene backbone plane. Conversely, the phenol moiety of **MPX** has larger conformational degrees of freedom, thus resulting in the broadened phenol ground state absorption feature.

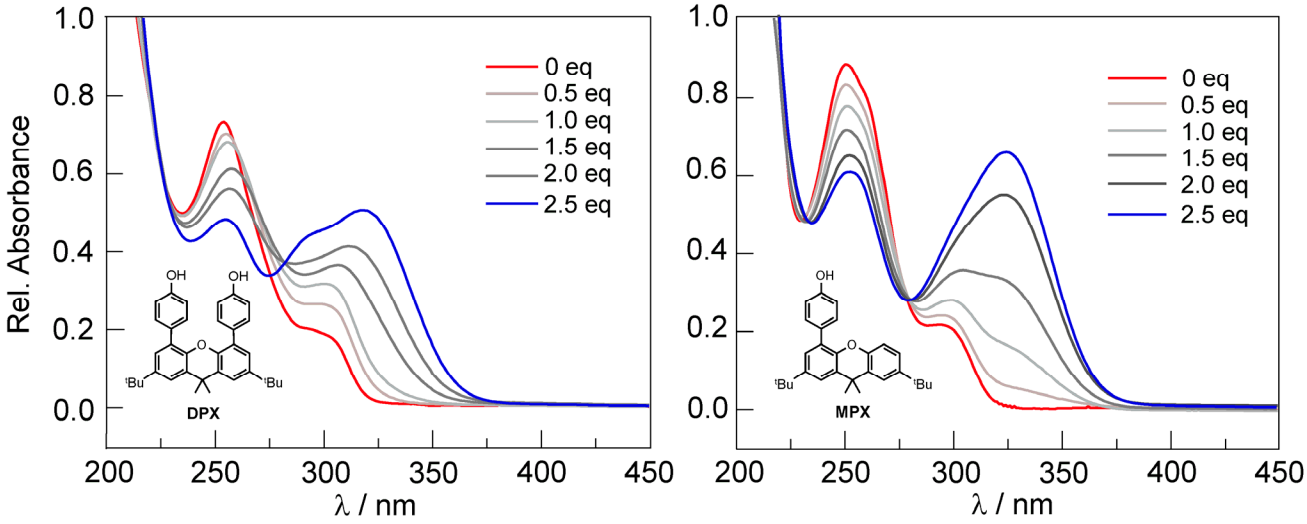

Figure 3.7 UV-vis spectroscopy of **DPX** (λ_{max} = 254 nm, 302 nm) and **MPX** (λ_{max} = 250 nm, 300 nm) with TBAOH titration. The decrease in 260 nm is accompanied by the appearance of a peak at 325 nm. At greater than 2 equiv. of base, a shoulder appears at 290 nm, corresponding to deprotonation of the second phenol. This second deprotonation affects peak **II** in Figure 3.3, and hence a proton dependence of the peak **II** potential only appears at >2 equiv. of base.

The oxidation of the dyads was examined in the presence of a proton accepting base pyridine. The interaction between phenol moieties and pyridine was characterized via UV-vis spectroscopy (Figure 3.8). The change in the UV-vis spectra of **DPX** upon pyridine addition is simply due to the added absorption feature of pyridine. No hydrogen-bonded complex was observed in the spectrum, the change caused by hydrogen-bonded complex may be too small to be resolved in UV-vis spectroscopy. The enthalpy of hydrogen bond formation between phenol and pyridine was measured by calorimetry: 5.25 ± 0.32 kcal/mol in benzene ($-\Delta H^0$).[18,19] The equilibrium constant of the phenol–pyridine hydrogen bonding complex in acetonitrile was reported as K_{eq}= 0.9 (for py + phenol → py···phenol, 303 K) and the complex formation enthalpy as 14 kJ/mol ($-\Delta H$).[20,21]

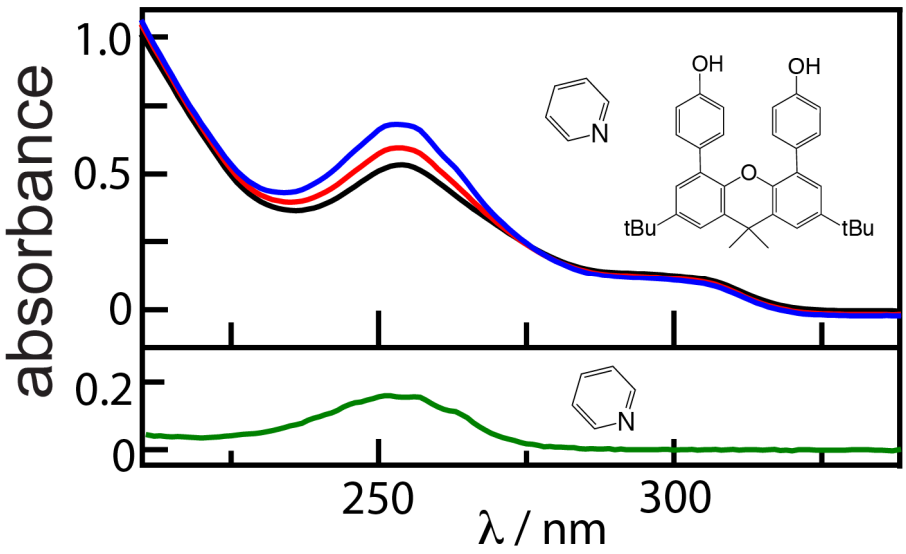

Figure 3.8 UV-vis spectra of **DPX** pyridine titration. (top) **DPX** (25 μM) with pyridine 0 equiv. (black), 2.5 equiv. (red) and 5 equiv. (blue) in acetonitrile. (bottom) UV-vis spectra of pyridine (5 equiv., 125 μM) in acetonitrile.

3.2.7 Base Dependence of CV

To investigate the effect of intramolecular hydrogen bonding on the redox properties of the dyad, cyclic voltammetry was performed on **DPX** and **MPX** with the titration of tetrabu-

tylammonium hydroxide, TBAOH.[14] Base addition to **MPX** results in a wave corresponding to phenolate oxidation at –0.3 V. For **DPX**, base addition affected peak **I** whereas peak **II** was largely unperturbed. These results suggest that peak **II** is a one-electron oxidation process largely independent of a proton (Figure 3.9 top) whereas peak **I** is more intimately related to the proton. Consistent with this contention, peak I shifts to –0.25 V with the addition of base, in accordance with the shift in potential resulting for the one-electron oxidation of phenolate to phenoxy radical (Figure 3.9).[33]

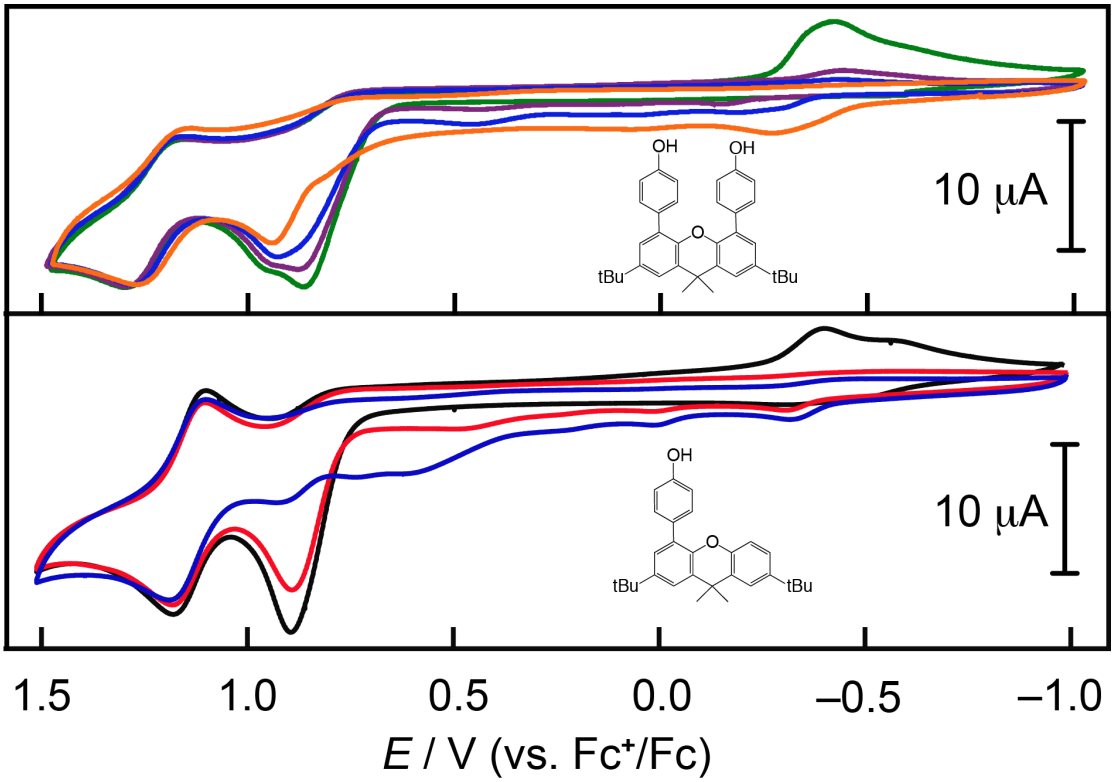

Figure 3.9 *(top)* Cyclic voltammogram of **DPX** with TBAOH base titration: 0 (green), 0.5 (violet), 1.0 (blue), and 2.0 equiv. (orange). (bottom) **MPX** titration 0 (black), 0.5 (red), and 1.5 equiv. (blue).

Whereas the affect of pyridine on **DPX** is not apparent in UV-vis spectra, changes are observed in the electrochemistry of the compound. Figure 3.10 shows the CV with pyridine titration. The phenol oxidation peak potential is lowered by 300 mV for **DPX** and became a 1 e^- oxidation wave (Figure 3.10). The first and second peak of **DPX**'s ECE oxidation decreased in se-

quential order, as more pyridine was added. The disappearance of the phenol oxidation peak (red arrow) was accompanied with the growth of a wave at ~0.7 V (blue arrow). This peak is attributed to the CEPT oxidation of **DPX** promoted by pyridine. In contrast to the hydroxide titration, the phenolate oxidation peak (ca. –0.5 V) was not observed with pyridine titration. The maximum CEPT peak amplitude was achieved when 2.5 equiv. of pyridine was added. Between 2.5 to 5 equiv. of added pyridine, the ECE oxidation peaks decreased gradually, but the CEPT oxidation peak amplitude remain unchanged. The amount of charge passed under the CEPT CV peak was calculated using literature procedures.[22] These results suggest that the 2 e^- oxidation process of **DPX** shown in Figure 3.10 becomes a 1 e^- oxidation when pyridine is the base.

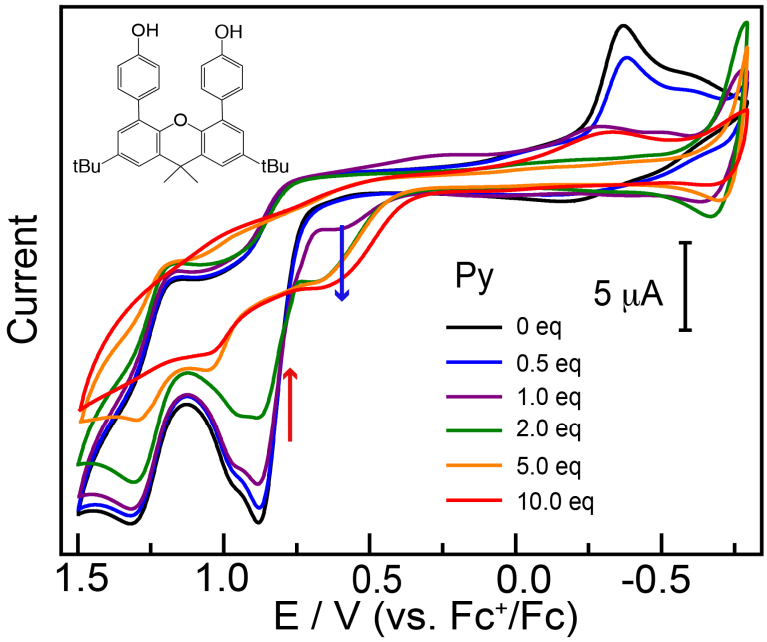

Figure 3.10 Cyclic voltammogram of **DPX** with pyridine base titration. Amount of pyridine added: 0 equiv. (—), 0.5 equiv. (—), 1 equiv. (—), 2 equiv. (—), 5 equiv. (—), and 10 equiv. (—). All CVs in this chapter were taken in 500 µM analyte, 0.1 M $TBAPF_6$ electrolyte in dry acetonitrile with a Pt working electrode and referenced to Fc^+/Fc.

3.2.8 DFT Calculation

Computational methods were employed to analyze the mechanistic pathways suggested from electrochemical experiments. Density functional theory (DFT) calculations were performed

with Gaussian 09 where all structures were optimized in the gas phase at the B3LYP/6-311+G(d,p) level of theory with Grimme's D3 dispersion correction[23] and verified by the absence of imaginary vibrational frequencies as local minima. Solvation free energies in acetonitrile were computed by the SMD polarizable continuum model,[24] which includes corrections for non-electrostatic interactions. From these gas-phase free energies, solution-phase reaction free energies were calculated for each step of the mechanism using the Born-Haber cycle.[25] The free energies were converted to reduction potentials[25–28] or pK_as[28–32] by using appropriate reference reactions to account for systematic error in the computations, primarily stemming from the calculation of solvation and thermal energies as well as functional and basis set limitations. For the phenol systems, oxidation of the xanthene backbone (reversible peak **III** in Figure 3.3) served as an internal reference between calculated and experimental reduction potentials, while the isodesmic reaction between the phenol systems and 4-*tert*-butylphenol was employed for improving the accuracy of calculated pK_as. The calculated electronics and energetics of the phenol systems are shown in Figure 3.11 for **DPX**, Figure 3.12 for spin state of **DPX**, Figures 3.13 and 3.14 for **FPX** and **MPX**, respectively.

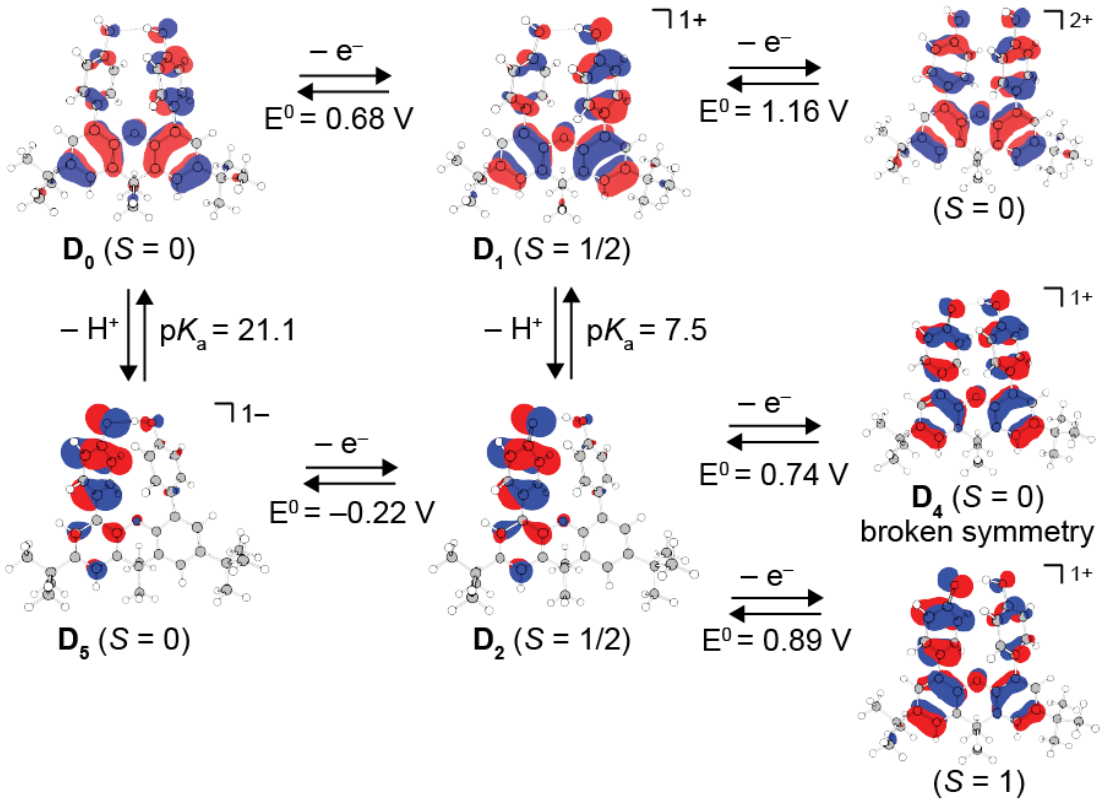

Figure 3.11 Calculated reduction potentials and pK_as for **DPX**. Bolded labels correspond to **DPX** states defined in Scheme 3.3. Molecular orbitals depict the HOMO for singlet (S = 0) states and the "spin density" SOMO for doublet and triplet states (S = 1/2 and 1, respectively). In addition, the "spin density" SOMO is shown for the **D₄** state of **DPX** and is predicted to be a "broken symmetry" singlet. The triplet ground state of **D₄** is more stable than the singlet.

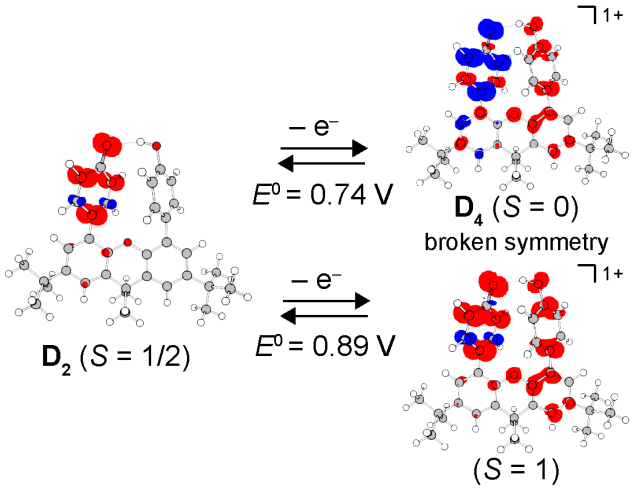

Figure 3.12 Spin density plots for the second oxidation of the **D₂** state. These plots correspond with the "spin density" SOMOs shown in the left. Red and blue shaded areas correspond to α and β spin density, respectively. The **D₄** state of **DPX** and is predicted to be a broken symmetry singlet where separate radicals on each of the phenol units are diamagnetically coupled to achieve an overall spin of zero.

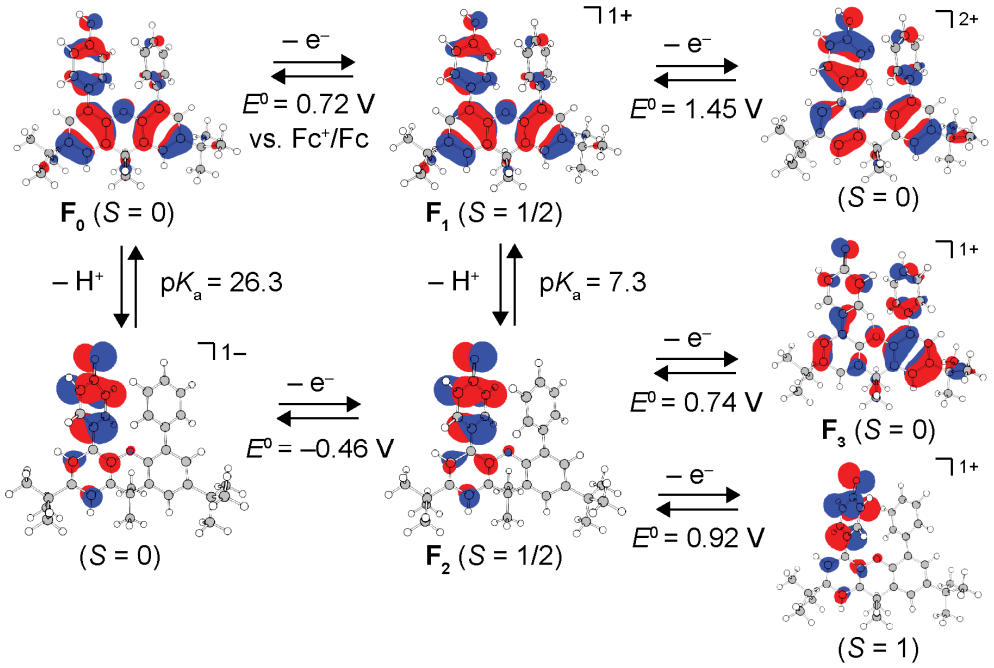

Figure 3.13 Calculated reduction potentials and pK_as for **FPX** using DFT. Bolded labels correspond to FPX states defined in Scheme 2. Molecular orbitals, shown as red and blue shaded areas, depict the HOMO for singlet (S = 0) states and the "spin density" SOMO for doublet and triplet states (S = ½ and 1, respectively).

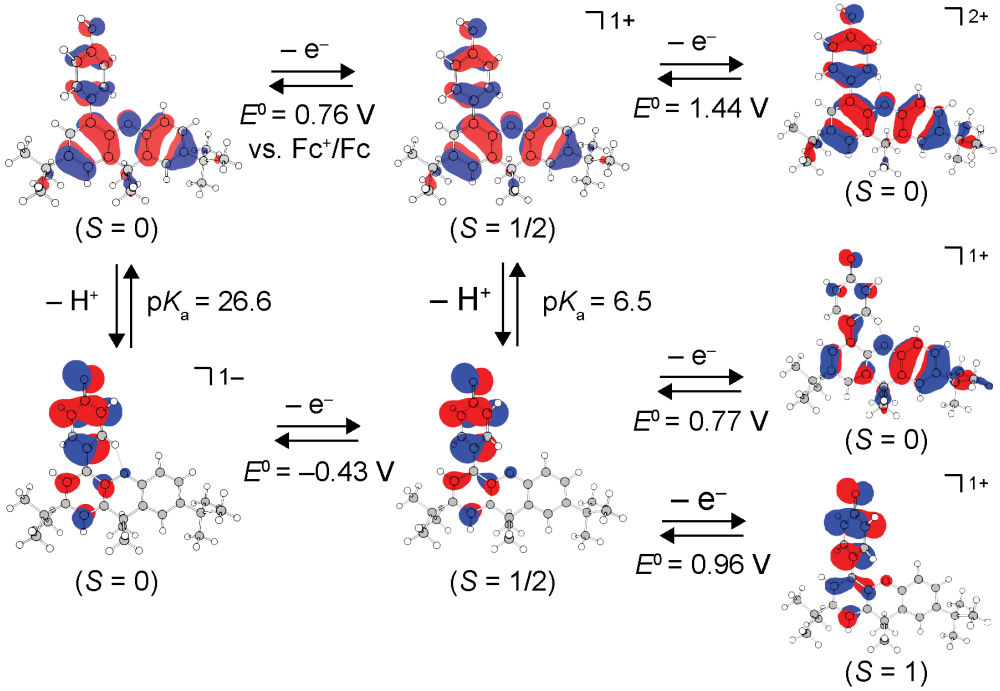

Figure 3.14 Calculated reduction potentials and pK_as for **MPX** using DFT. Molecular orbitals, shown as red and blue shaded areas, depict the HOMO for singlet (S = 0) states and the "spin density" SOMO for doublet and triplet states (S = 1/2 and 1, respectively).

3.2.9 Spectroelectrochemistry

As the absorption features of phenol radical have been characterized,[2] thus spectroelectrochemical Uv-vis spectroscopy was attempted to correlate the electrochemistry to the radical species. However, consistent with the CV results, the **DPX** absorption feature decay was accompanied with a rise of peaks at 230 and 290 nm; the phenol radical absorption feature (~ 410 nm) was not observed (Figure 3.15). These results are consistent with a prompt chemical reaction (no intermediate accumulation) upon oxidation, and one that does not produce the one-electron oxidized radical.

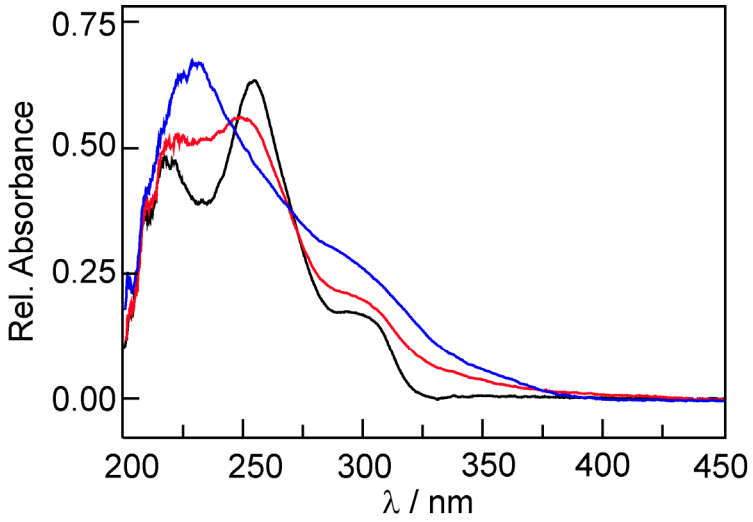

Figure 3.15 Spectroelectrochemical UV-vis spectroscopy during bulk electrolysis performed at 1.1 V (vs. Fc^{+}/Fc). Bulk electrolysis was performed from 0.9 V to 1.3 V in 0.1 V intervals for 600 sec. Spectrum taken at other potentials identically overlaps therefore only spectra at 0.9 V bulk electrolysis are shown. **DPX** 0 s (black), 40 s (red) and 300 s (blue).

3.3 Discussion

The two separated waves (Figure 3.3) in **DPX** indicate that the oxidation process of stacked phenols is perturbed in the dyad structure. We note that the peak potentials and ratio of peak amplitudes are invariant over a concentration range of 0.1–5 mM (Figure 3.5), confirming

that the CV characteristics are not a result of an intermolecular interaction. CV features **I** and **II** exhibit a peak potential dependence on scan rate of ~60 mV/decade (Figure 3.6), suggesting the coupling of a chemical step with each electron transfer step.[22]

This peak amplitude is consistent with the two-electron ECE mechanism of phenol oxidation in CH_3CN:[22,33]

(Eq. 3.1)

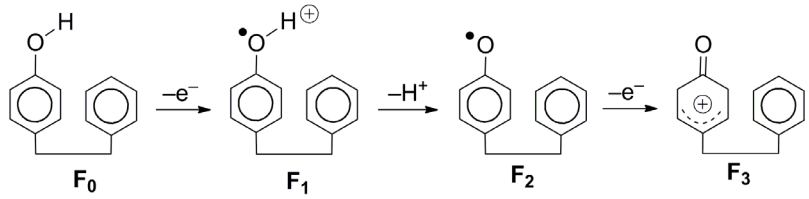

The first oxidation yields a phenol radical cation (**F₁**), which has a pK_a ~ –5 in acetonitrile, some ~20 pK_a units more acidic than the starting phenol. **F₁** deprotonates to a neutral phenol radical **F₂**,[8] which is oxidized to phenoxium (**F₃**) at a lower anodic potential than the initial oxidation, thus resulting a single peak for the total two-electron process.

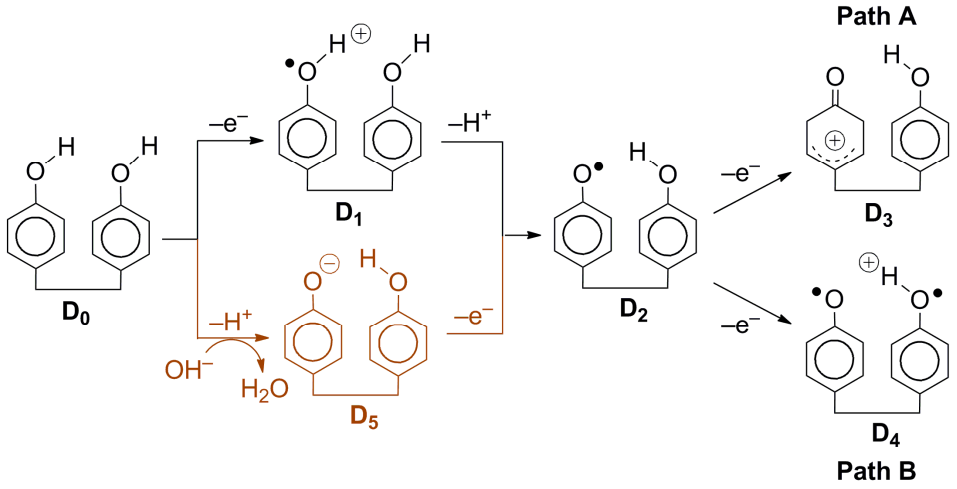

Scheme 3.2 The postulated oxidation pathways of **DPX**. Path A depicts a case where the second oxidation occurs on the phenol ring of the first oxidation step. Thus, path A results in a phenoxium and an intact phenol (**D₃**). Path B depicts a case where the second oxidation occurs on the other phenol ring. Path B results in a bi-radical like product (**D₄**). The products both pathways decompose quickly, inhibiting isolation and identification.

The first one-electron oxidation of **DPX** in base is described by **D₅** to **D₂** in Scheme 3.2. In base, phenol **D₀** is deprotonated to phenolate **D₅**, which is the species that is oxidized by one-

electron to produce phenoxy radical **D₂**. Given peak **II** is proton independent (base < 2 equiv), the subsequent oxidation of **D₂** proceeds from phenolate. In the absence of base, **D₂** is produced by the direct one-electron oxidation (peak **I** in Figure 3.3) of **D₀** to produce phenol radical cation species (**D₁** in Scheme 3.2) followed by fast deprotonation to yield phenol radical (**D₂**).[8,34]

The second 1 e^- oxidation of **DPX** requires deprotonation of the first oxidation product (**D₁** to **D₂**, Scheme 3.3). Without removal of the proton, the phenol radical (**D₁**) requires a much higher potential for oxidation than the deprotonated radical (**D₂**). The loss of proton results in irreversibility (blue arrow, Scheme 3.3). In this regard, one possible explanation for the observed overall 1 e^- oxidation of **DPX** is that the associated pyridine prevents deprotonation of the radical cation, by effectively binding the proton in a hydrogen bond complex. Without the deprotonation, the follow-up 2nd oxidation does not occur in the scanned potential range.

Scheme 3.3 Comparison of the postulated oxidation pathways of **DPX** with hydroxide vs. with pyridine. The blue arrow refers to the irreversible phenol oxidation which results from deprotonation. The red arrow portrays the case of electrochemical reversible phenol oxidation.

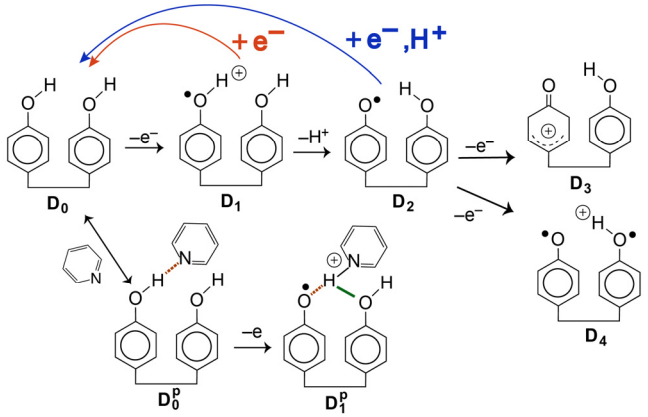

The pK_a of pyridinium is known to be much lower than pyridine (pK_a PyH^+ = 0.6),[35] and therefore proton transfer to unassociated pyridine is unlikely. Rather, pyridine and phenol are strongly associated and upon oxidation of phenol, proton shift is likely with the pyridinium species contained within the associated complex: pyridine···phenol $\xrightarrow{-e^-}$ phenolic radical···pyridinium. It is known that appended bases in hydrogen bonded contact to phenol support the latter's 1 e^-

oxidation.[10] A characteristic of this condition is that the 1 e^- oxidation is reversible. In the case of **DPX** upon pyridine titration, a reversible wave is not observed. Instead, the large shift of ETPT waves (in the absence of pyridine) to less oxidizing potentials and loss of reversibility on a cathodic scan suggests that pyridine associated to phenols can promote CEPT reaction ($\mathbf{D_0^p}$ to $\mathbf{D_1^p}$) by serving as a proton acceptor (Scheme 3.3).

A scan rate dependent shift of the peak **I** potential indicates involvement of a chemical step, which is consistent with deprotonation accompanying the conversion of $\mathbf{D_0}$ to $\mathbf{D_2}$. Further oxidation of $\mathbf{D_2}$ may follow two paths, indicated by Path A and B. In Path A, the two-electron oxidation process results in one phenoxium and an intact phenol unit ($\mathbf{D_3}$) and in Path B, $\mathbf{D_4}$ is produced. Computation shows that biradical $\mathbf{D_4}$ (triplet) is considerably more stable than $\mathbf{D_3}$ (vide infra).

Spectroelectochemistry shows that this product ($\mathbf{D_4}$) is unstable, and it cannot be detected. Because the standard potential of the second oxidation step (from $\mathbf{D_2}$ to $\mathbf{D_4}$) is greater than that of the first oxidation step (from $\mathbf{D_1}$ to $\mathbf{D_2}$, Scheme 3.2), the phenol oxidation peaks are separated. The separation of ~100 mV occurs about the potential that is observed for the single wave oxidation of **FPX**. Note that the overall ECE mechanism is similar for both **DPX** and **FPX**. However, the presence of the hydrogen bonding from the second phenol in **DPX** stabilizes the first oxidation with respect to the ensuing oxidation, thus resulting in a split peak in the CV.

A computational analysis of phenols with appended pyridine as internal proton acceptor[36,37] suggests that the modulation of phenol oxidation, such as **DPX**, can originate from the hydrogen bonding. Consistent with this contention is the disparate behavior of **DPX** and **FPX** despite similar π-aromatic electronic environments. Computational results of electronics and energetics of the phenol systems are shown in Figure 3.11 and Figure 3.12 for **DPX**, and in Figure

3.13 and Figure 3.14 for **FPX** and **MPX**, respectively. First, the calculated reduction potentials for all three model systems agree with an ECE mechanism. The first oxidation facilitates the deprotonation of a phenol unit, where the calculated first pK_as decreases by 13–20 units to pK_as = ~7 in acetonitrile, which establishes a minor equilibrium of singly deprotonated phenol systems. This then enables the second oxidation to occur at similar potentials as the first oxidation, which is consistent with the integration of the first oxidation wave to a two-electron process in the CVs of the model systems (peaks **I**/**II**, **IV**, and **V** in Figure 3.3). In particular, DFT determines a larger first and second reduction potential difference for **DPX** of ~60 mV compared to that of **FPX** and **MPX** (of 10–20 mV gap), which explains why **DPX** exhibits split peaks (**I** and **II** in Figure 3.3) in CVs whereas **FPX** and **MPX** only display a single peak (**IV** and **V** in Figure 3.3) as the second oxidation closely overlaps with the first oxidation. In contrast, calculations show that without the intermediate deprotonation step, the second oxidation of the phenols occurs ~500–700 mV to higher anodic potential, which supports the assignment that the second oxidation is the subsequent oxidation of deprotonated product. Similarly, when the phenol are deprotonated prior to any oxidations (by the addition of base), the calculations predict a drastic cathodic shift of the first reduction potential (~900–1200 mV) that is observed in the CVs of base-titrated phenol systems (Figure 3.9), where the first oxidation now occurs from –0.25 to –0.30 V vs. Fc^+/Fc. Direct comparison of calculated to experimental reduction potentials is discouraged because whereas DFT reports reversible potentials, the CVs show only peak potentials for oxidation of the phenol systems—the experimental reversible reduction potentials are unknown. Notwithstanding, the PCET effects of oxidations and deprotonations on the phenol systems are readily reproduced by computation.

Analysis of calculated molecular orbitals and spin densities provides a qualitative view of the electronic interaction occurring in the phenol model systems, and in particular, suggests that the second oxidation of **DPX** is distributed on the adjacent phenol moiety (Path B in Scheme 3.2). In all phenol systems, visualization of the spin density via the corresponding singly occupied molecular orbital (SOMO) shows that the first oxidation results in a radical cation that is distributed on a single phenol with minor extension of spin to the xanthene backbone (e.g., see the $\mathbf{D_1}$ state for **DPX** in Figure 3.11). Upon deprotonation, the radical cation becomes primarily localized on the single phenol unit, which is consistent with Scheme 3.2 (i.e., $\mathbf{D_2}$ and $\mathbf{F_2}$ in Scheme 3.2 and Equation 3.1, respectively). The second oxidation after deprotonation favors the singlet (phenoxium cation) over the triplet (biradical) state by ~4–6 kcal/mol. For **FPX** and **MPX**, the spin density of this singlet state was zero, demonstrating that the second oxidation removes an electron from the same phenol unit that had initially undergone the first oxidation and deprotonation (e.g., $\mathbf{F_3}$ in Equation 3.1). Conversely, for **DPX**, the same singly-deprotonated, doubly-oxidized singlet state exhibited significant spin density of opposing character on each of the phenol units (triplet biradical $\mathbf{D_4}$ in Figure 3.11 and Scheme 3.2, and Figure 3.12), signifying the presence of "broken symmetry" where the α and β spins of the highest occupied molecular orbital (HOMO) are localized as antiferromagnetically-coupled radical cations on each of the phenol units, respectively.[38,39] Thus, a formal singlet spin state is preserved while retaining local diradical character. These calculations suggest that the biradical is stabilized by the coupling of phenol rings (via hydrogen bonding) and thus Path B in Scheme 3.2 describes the second oxidation of **DPX**.

3.4 Conclusion

In summary, we have shown that oxidation of a phenol moiety is perturbed when it resides within a cofacial dyad. The stacked phenol units of **DPX** display a cooperative ECE oxidation mechanism that is unique from that of mono-phenol analogues (**FPX** and **MPX**). Unlike the ECE mechanism of **FPX** and **MPX** in acetonitrile, **DPX** showed two one-electron oxidations. The presence of broken symmetry in **DPX**, but not in **FPX** and **MPX**, indicates the importance of the hydroxide group on the adjacent phenol, which aids in electronically modifying electron density (and by extension, the radical) within the dyad and also assists in coupling the two units via hydrogen bonding site. Consequently, the strong coupling of phenols in **DPX** results in each phenol not behaving as independent redox units but rather as a cooperative redox entity where removal of a second electron from the system occurs at a higher anodic potential than that of the first oxidation. These results have implications to the radical transport pathway in RNR. Comparison of **DPX** to **FPX** shows that the potential of phenol is perturbed by ~50 mV, (peak potential difference between the first oxidation of **DPX** and **FPX**). We note that the entire redox ramp for radical transport in RNR—from Y_{356} to Y_{731}—is estimated to be ~100 mV uphill.[40] Thus the perturbation of the oxidation of the phenol moiety within the dyad would represent significant tuning of the redox potential within the radical transport pathway of RNR. Both statistical and computational analyses suggest that pairs of aromatic amino acids with a centroid distance range of 3.4 – 7 Å, like that of the Y_{730} and Y_{731} dyad, are likely to play crucial functions in substrate recognition, structure, and catalysis in proteins.[41, 42] Various aspects of through-space π-interaction have been investigated for their effects on charge transfer, pK_a and energy transfer.[43–45] We now show that the redox properties of the phenol moiety of tyrosine will be affected by cofacial disposition within a dyad, thus highlighting the fidelity of the RNR radical transport

pathway. Further investigation on the energetics and mechanism of **DPX** oxidation in terms of hydrogen bonding and π–interaction will afford greater insight into how these non-covalent interactions are being used in enzyme systems like RNR.

The presentation of two phenols on a xanthene backbone is akin to the tyrosine dyad (Y_{730} and Y_{731}) of ribonucleotide reductase. X-ray crystallography reveals that the two phenol moieties are cofacially disposed at 4.35 Å. Cyclic voltammetry (CV) reveals that phenol oxidation is modulated within the dyad, which exhibits a splitting of one-electron waves with the second oxidation of the phenol dyad occurring at larger positive potential than that of a typical phenol. In contrast, a single phenol appended to a xanthene exhibits a two-electron (ECE) process, consistent with reported oxidation pathways of phenols in acetonitrile. The perturbation of the phenol potential by stacking is reminiscent of a similar effect for guanines stacked within DNA base pairs.[16]

3.5 Experimental Details

3.5.1 Materials and Methods

Materials. 2,7-Di-tert-butyl-4,5-dibromo-9,9-dimethyl-xanthene, 4-hydroxyphenyl boronic acid, phenyl boronic acid pinacol ester, N,N-dimethyl formamide (DMF), 2,7-di-tert-butyl-9,9-dimethyl-xanthene (**BB**) (Sigma Aldrich), tetrakis(triphenylphosphane)palladium(0) ($Pd(PPh_3)_4$) (Strem), and potassium carbonate (K_2CO_3) (Mallinkrodt) were used as received.

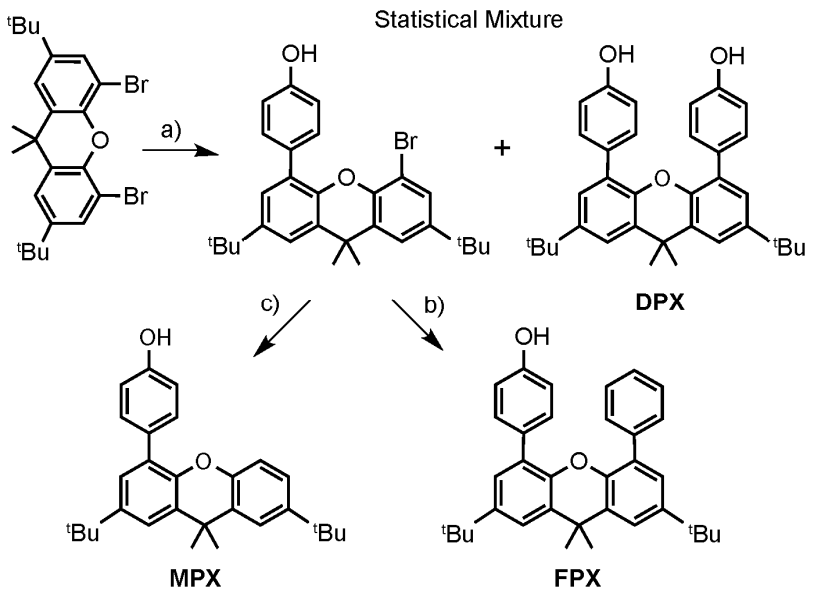

Scheme 3.4 Synthesis of **DPX**, **FPX**, and **MPX**.

Synthesis. The syntheses of **DPX**, **FPX** and **MPX** were achieved by utilizing Suzuki cross-coupling with various Pd catalysts (Scheme 3.4). The sequential cross coupling afforded the final asymmetric model systems. Bromo-aryl and phenyl boronic acid did not couple well therefore phenyl boronic acid pinacol ester was used instead. Column chromatography was performed on the biotage column chromatography instrument.

2,7-di-tert-butyl-4,5-di(4-hydroxyphenyl)-9,9-dimethyl-xanthene (**DPX**): (a) 2,7-Di-tert-butyl-4,5-dibromo-9,9-dimethyl-xanthene (400 mg, 0.833 mmol, 1.00 equiv.), 4-hydroxyphenyl boronic acid (345 mg, 2.49 mmol, 3.00 equiv.), K_2CO_3 (345 mg, 2.49 mmol, 3.00 equiv.) and $Pd(PPh_3)_4$ (114 mg, 0.098 mmol, 0.120 equiv.) were added to 100 mL of a 9:1 DMF:water mixture in a 250 mL round-bottom flask. The mixture was heated at reflux overnight under N_2 and then cooled to room temperature after which 400 mL of distilled water was added to the flask. The product was extracted with dichloromethane (DCM), and a solid was obtained upon drying

under vacuum. The **DPX** product was purified by column chromatography (hexanes/DCM) to deliver a white solid (310 mg, 73.5%) ^{1}H NMR (600 MHz, CD_2Cl_2): δ = 7.40 (d, 2H), 7.17 (d, 2H), 7.12 (m, 4H), 6.66 (m, 4H), 1.71 (s, 6H), 1.35 (s, 18H).

2,7-di-tert-butyl-4-(4-hydroxyphenyl)-9,9-dimethyl-xanthene (**MPX**): (a) 2,7-Di-tert-butyl-4,5-dibromo-9,9-dimethyl-xanthene (400 mg, 0.833 mmol, 1.00 equiv.), 4-hydroxyphenyl boronic acid (114 mg, 0.833 mmol, 1.00 equiv.), K_2CO_3 (115.13 mg, 0.833 mmol, 1.0 equiv.), $Pd(PPh_3)_4$ (113 mg, 0.098 mmol, 0.120 equiv.) were added to 100 mL 9:1 mixture of DMF and water in a 250 mL round-bottom flask. The mixture was heated at reflux overnight under N_2 and then cooled to room temperature after which 400 mL of distilled water was added to the flask. The product was extracted with dichloromethane (DCM), and a solid was obtained upon drying under vacuum. The product 2,7-di-tert-butyl-4-(4-hydroxyphenyl)-5-bromo-9,9-dimethyl-xanthene was extracted with DCM, dried under vacuum and purified by column chromatography (hexanes/DCM). (c) The mono-bromo xanthene was dissolved in 30.0 mL THF and 1 equivalent of N-butyl lithium in THF was added slowly via cannula. After stirring at –20 C° about an hour, H_2O was added to quench the reaction. The final product (**MPX**) was purified by column chromatography and yielded the product as a white solid (144 mg, 41.7%) ^{1}H NMR (500 MHz, CD_2Cl_2): δ = 7.52 (d, 2H), 7.42 (m, 2H), 7.28 (m, 1H), 7.23 (m, 1H), 6.96 (m, 2H), 6.90(d, 2H), 1.72 (s, 6H), 1.40 (s, 9H), 1.37 (s, 9H).

2,7-di-tert-butyl-4-phenyl-5-(4-hydroxyphenyl)-9,9-dimethyl-xanthene (**FPX**): (c) Statistical mixture product of step (a) 2,7-di-tert-butyl-4-bromo-5-(4-hydroxyphenyl)-9,9-dimethyl-xanthene (250 mg, 0.833 mmol, 1.00 equiv.), phenyl boronic acid pinacol ester (290 mg, 1.20

mmol, 1.50 equiv.), 4-hydroxyphenyl boronic acid pinacol ester (264 mg, 1.20 mmol, 1.50 equiv.), K_2CO_3 (442 mg, 3.20 mmol, 4.00 equiv.), $Pd(dppf)Cl_2{*}CH_2Cl_2$ (78.17 mg, 0.10 mmol, 0.125 equiv.) were added to 25.0 mL 9:1 mixture of 1,4-Dioxane and water in a 250 mL Schlenk flask. The mixture was heated at reflux overnight under N_2 and then cooled to room temperature after which 400 mL of distilled water was added to the flask. The product was extracted with dichloromethane (DCM), and a solid was obtained upon drying under vacuum. The product (**FPX**) (R_f~ 0.8, DCM) was purified by column chromatography (Hexanes → DCM: Hexanes (1:4) → DCM) and obtained as white solid. ^{1}H NMR (500 MHz, CD_3OD): δ = 7.49 (dd, 1H), 7.44 (dd, 2H), 7.23~7.21 (m, 3H), 7.15~7.11 (m, 4H), 7.03 (t, 2H), 6.53 (d, 2H), 1.70 (s, 6H), 1.35(d, 18H). ^{1}H NMR (500 MHz, $CDCl_3$): δ = 7.43 (dd, 2H), 7.32~7.21 (m, 4H), 7.21~7.12 (m, 5H), 6.56 (d, 2H), 1.73 (s, 6H), 1.36(d, 18H).

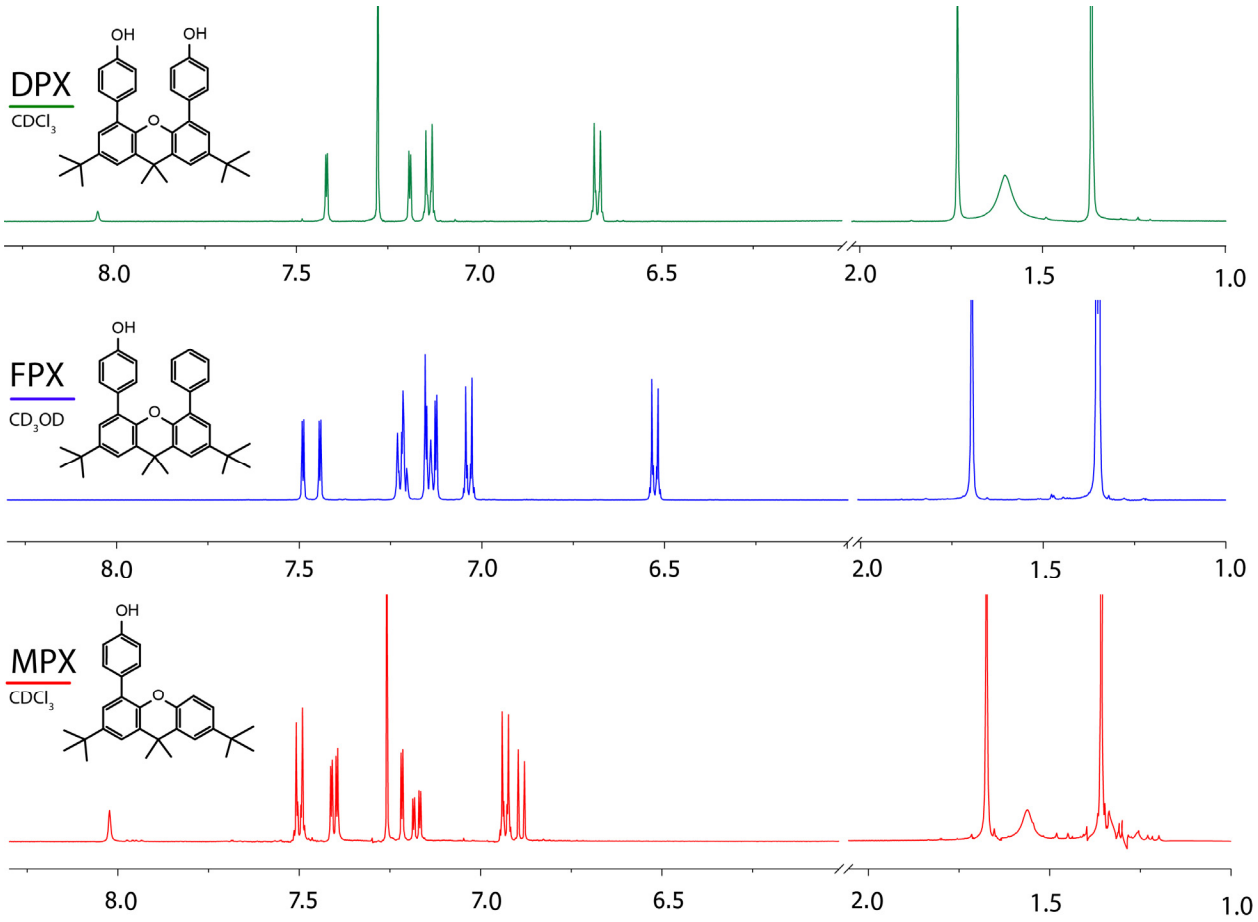

Figure 3.16 ^{1}H NMR spectroscopy of **DPX** ($CDCl_3$), **FPX** (CD_3OD) and **MPX** ($CDCl_3$).

3.5.2 Electrochemical Methods

Electrochemical measurements were performed on compounds dissolved in acetonitrile in a nitrogen atmosphere glove box at room temperature. All CVs in this chapter were taken on 500 µM analyte, 0.1 M $TBAPF_6$ electrolyte in dry acetonitrile with a Pt working electrode and referenced to Fc^+/Fc. Voltammetric experiments were conducted with computer controlled CH Instruments 760D Electrochemical Workstation using CHI Version 10.03 software. A three-electrode cell with a 1 mm diameter planar platinum working electrode was used together with a platinum wire counter electrode. A platinum wire reference electrode was used as a pseudo-reference and all CVs were referenced to Fc^+/Fc. Acetonitrile (ACS, 99.95%, Aldrich) was puri-

fied on a Glass Contour Solvent Purification System manufactured by SG Water and kept over activated 3 Å molecular sieves overnight under nitrogen. The residual water in acetonitrile was less than ~2 ppm by Mettler Toledo C20 compact Karl-Fischer coulometer. The electron equivalency was determined from CV measurements of peak height i_p:

$$i_p = 0.992FSC^0\sqrt{D}\sqrt{\frac{Fv}{RT}} \quad \text{(Eq. 3.2)}$$

where D is the diffusion coefficient ($7.5 \pm 0.5\times10^{-6}$ cm^2/s) obtained from DOSY NMR spectroscopy of **DPX** (**FPX** and **MPX** are assumed to be the same), v is the scan rate (0.1 V/s), F is Faraday's constant, T is set to room temperature (297 K), C^0 is the initial concentration of analyte (0.5 mM), R is the gas constant, and S is the surface area of working electrode (0.0628 cm^2). The experimental i_p matches the calculated two-electron i_p.

3.5.3 X-ray Crystallographic Details

Diffraction quality crystals of **DPX** were obtained by slow evaporation of a 1:1 mixture of hexane and DCM, affording crystals as clear blocks; a single crystal was cut from a larger one for the x-ray diffraction study. Low temperature (100 K) X-ray diffraction data was collected on a Bruker three-circle platform goniometer equipped with an Apex II CCD detector and an Oxford cryostream cooling device, performing φ- and ω- scans. Radiation was generated from a graphite fine focus sealed tube Mo Kα (0.71073 Å) source. Crystals were mounted on a cryoloop using Paratone-*N* oil. Data were processed and refined using the program SAINT supplied by Siemens Industrial Automation. Structures were solved by intrinsic phasing methods in SHELXT and refined by standard difference Fourier techniques in the SHELXTL program suite. Hydrogen atoms were located in the difference map and were refined isotropically using a riding model; all non-hydrogen atoms were refined anisotropically. Unit cell parameters, morphology, and solu-

tion statistics for the structure are summarized in Table 3.1. Thermal ellipsoid plots are drawn at the 50% probability level with hydrogen atoms removed for clarity.

3.5.4 Absorption Measurements

Spectroelectrochemical measurements were made in a N_2-atmosphere glovebox using a CH Instruments 760D Electrochemical Workstation using CHI Version 10.03 software. Thin-layer UV-vis spectroelectrochemistry experiments were performed using a 0.5 mm path length quartz cell with an Ocean Optics USB4000 spectrophotometer and DT-Mini-2GS UV-vis-NIR light source in conjunction with the CH electrochemical workstation. Sample concentration was 1 mM for spectroelectrochemical UV-vis spectroscopy. Electrolyte $TBAPF_6$ concentration was 0.1 M in acetonitrile.

UV-vis spectra were recorded on a Varian Cary 5000 UV-vis-NIR spectrophotometer using 1 cm path length 6Q quartz cell. For TBAOH titration, a 1.0 M methanol solution obtained from Sigma Aldrich was used as received. The analyte sample was made in a N_2-atmosphere glove box.

3.5.5 DOSY NMR Spectroscopy for the Diffusion Coefficient Measurement

The diffusion coefficient of **DPX** was measured by DOSY NMR spectroscopy. The diffusion coefficient is calculated from the average of ^1H NMR aromatic peaks (7.40 (d, 2H), 7.17 (d, 2H), 7.12 (m, 4H), 6.66 (m, 4H)).

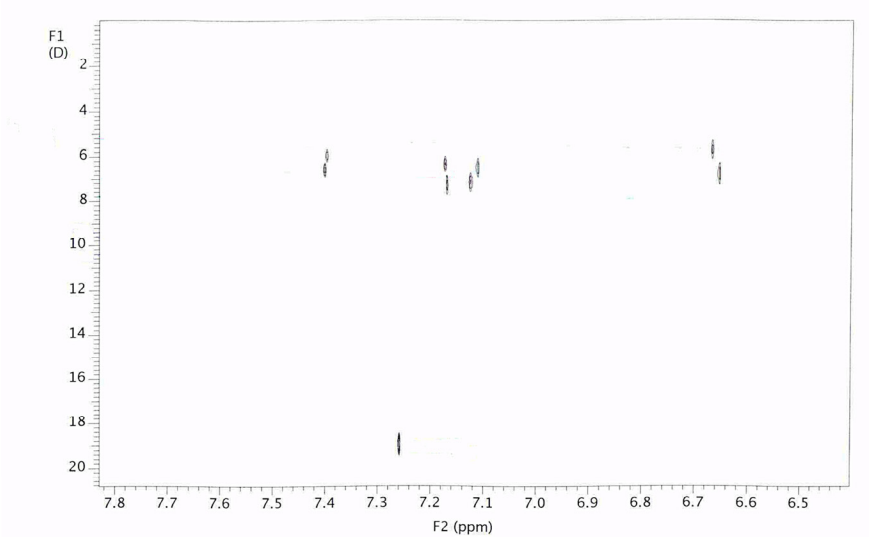

Figure 3.17 DOSY NMR spectroscopy of **DPX**, taken at $CDCl_3$ (the solvent peak appears at 7.25 ppm) The x-axis is ^1H proton chemical shift (ppm) and y-axis is D (unit 10^{-6} cm^2/s). The spectrum is taken at room temperature at 600 MHz Agilent DD2-600 instrument at DCIF, Harvard University.

3.5.6 DFT Calculations

The calculation of solution-phase reduction potentials[25–28] and pK_as[27–32] were accomplished by using the Born-Haber free energy cycle. Free energies of the products and reactants were determined in the gas phase and then referenced to solvent by computing the solvation energy for each gas-phase species. These calculations were performed with Gaussian 09, revision D.01 using the B3LYP hybrid DFT functional with Grimme's D3 dispersion correction (Becke-Johnson damping) and the 6-311+G(d,p) basis set. All structures were initially optimized in vacuum with tight geometry. SCF convergence criteria and vibrational frequency analysis verified that optimized structures were local minima, from which enthalpy, entropy, and Gibbs free energies (at T = 298.15 K) were calculated. Solvation free energies of the gas-phase optimized structures were computed in acetonitrile by the SMD polarizable continuum model, which includes corrections for non-electrostatic interactions. For reduction potential calculations, free energies were first

converted into an absolute electrode potential and then calibrated by referencing the calculated xanthene backbone reversible reduction potential of **DPX** to that obtained from CV measurements ($E_{1/2}$ = 1.23 V vs. Fc^+/Fc in acetonitrile, see Figure 3.3). For pK_a calculations, the Born-Haber cycle was prepared for an isodesmic reaction between the given phenol system and 4-*tert*-butylphenol where the latter pK_a in acetonitrile is experimentally known (pK_a = 27.5[35]); this pK_a served as the reference point between calculation and experiment. These appropriate reference reactions mitigate large systematic errors primarily stemming from the calculation of solvation and thermal energies as well as functional and basis set limitations.

3.6 References

(1) Koo, B.; Huynh, M.; Halbach, R. L.; Stubbe, J.; Nocera, D. G. *J. Am. Chem. Soc*. **2015**, *137*, 11860.

(2) Stubbe, J.; Nocera, D. G.; Yee, C. S.; Chang, M. C. Y. *Chem. Rev.* **2003**, *103*, 2167.

(3) Minnihan, E. C.; Nocera, D. G.; Stubbe, J. *Acc. Chem. Res.* **2013**, *46*, 2524

(4) Uhlin, U.; Eklund, H., *Nature* **1994**, *370*, 533.

(5) Nordlund, P.; Reichard, P. *Annu. Rev. Biochem.* **1998**, *67*, 71.

(6) Holder, P. G.; Pizano, A. A.; Anderson, B. L.; Stubbe, J.; Nocera, D. G. *J. Am. Chem. Soc.* **2012**, *134*, 1172.

(7) Pizano, A. A.; Olshansky, L.; Holder, P. G.; Stubbe, J.; Nocera, D. G. *J. Am. Chem. Soc.* **2013**, *135*, 13250.

(8) Warren, J. J.; Winkler, J. R.; Gray, H. B. *FEBS Lett.* **2012**, *586*, 596.

(9) Weinberg, D. R.; Gagliardi, C. J.; Hull, J. F.; Murphy, C. F.; Kent, C. A.; Westlake, B. C.; Paul, A.; Ess, D. H.; McCafferty, D. G.; Meyer, T. J. *Chem. Rev.* **2012**, *112*, 4016.

(10) Markle, T. F.; Rhile, I. J.; Mayer, J. M. *J. Am. Chem. Soc.* **2011**, *133*, 17341.

(11) Moore, G. F.; Hambourger, M.; Kodis, G.; Michl, W.; Gust, D.; Moore, T. A.; Moore, A. L. *J. Phys. Chem. B* **2010**, *114*, 14450.

(12) Irebo, T.; Reece, S. Y.; Sjödin, M.; Nocera, D. G.; Hammarström, L. *J. Am. Chem. Soc.* **2007**, *129*, 15462.

(13) Costentin, C.; Robert, M.; Savéant, J.-M.; Tard, C. *Angew. Chem.* **2010**, *122*, 3891.

(14) Costentin, C.; Robert, M.; Savéant, J.-M.; Tard, C. *Phys. Chem. Chem. Phys.* **2011**, *13*, 5353.

(15) Sistare, M. F.; Codden, S. J.; Heimlich, G.; Thorp, H. H. *J. Am. Chem. Soc.* **2000**, *122*, 4742.

(16) Stemp, E. D. A; Arkin, M. R.; Barton, J. K. *J. Am. Chem. Soc.* **1997**, *119*, 2921.

(17) Nick, T. U.; Lee, W.; Koßmann, S.; Neese, F.; Stubbe, J.; Bennati, M. *J. Am. Chem. Soc.* **2015**, *137*, 289.

(18) Spencer, J. N.; Sweigart, J. R.; Brown, M. E.; Bensing, R. L.; Hassinger, T. L.; Kelly, W.; Housel, D. L.; Reisinger, G. W.; Reifsnyder, D. S. *J. Phys. Chem.* **1977**, *81*, 2237.

(19) Spencer, J. N.; Holmboe, E. S.; Firth, D. W.; Kirshenbaum, M. R. *J. Sol. Chem.* **1981**, *10*, 745.

(20) Titov, E. V.; Shurpach, V. I.; Belkina, G. A.; Gonchar, N. P. *J. Mol. Str.* **1990**, *219*, 257.

(21) Rospenk, M.; Zeegers-Huyskens, T. *J. Phys. Chem. A* **1997**, *101*, 8428.

(22) Savéant, J.-M. *Elements of Molecular and Biomolecular Electrochemistry*: An Electrochemical Approach to Electron Transfer Chemistry; John Wiley: Hoboken, NJ, 2006.

(23) Grimme, S.; Antony, J.; Ehrlich, S.; Krieg, H. *J. Chem. Phys.* **2010**, *132*, 154104.

(24) Marenich, A. V.; Cramer, C. J.; Truhlar, D. G. *J. Phys. Chem. B* **2009**, *113*, 6378.

(25) Cramer, C. J. In *Essentials of Computational Chemistry Theories and Models*; John Wiley: West Sussex, England, 2004; p. 429.

(26) Baik, M.-H.; Friesner, R. A. *J. Phys. Chem. A* **2002**, *106*, 7407.

(27) Konezny, S. J.; Doherty, M. D.; Luca, O. R.; Crabtree, R. H.; Soloveichik, G. L.; Batista, V. S. *J. Phys. Chem. C* **2012**, *116*, 6349.

(28) Solis, B. H.; Hammes-Schiffer, S. *Inorg. Chem.* **2011**, *50*, 11252.

(29) Ho, J.; Coote, M. L. *J. Chem. Theory Comput.* **2009**, *5*, 295.

(30) Alongi, K. S.; Shields, G. C. *Annu. Rep. Comput. Chem.* **2010**, *6*, 113.

(31) Casasnovas, R.; Fernández, D.; Ortega-Castro, J.; Frau, J.; Donoso, J.; Muñoz, F. *Theor. Chem. Acc.* **2011**, *130*, 1.

(32) Sastre, S.; Casasnovas, R.; Muñoz, F.; Frau, J. *Theor. Chem. Acc.* **2012**, *132*, 1310.

(33) Richards, J. A.; Whitson, P. E.; Evans, D. H. *J. Electroanal. Chem. Interfacial Electrochem.* **1975**, *63*, 311.

(34) Bordwell, F. G.; Cheng, J. *J. Am. Chem. Soc.* **1991**, *113*, 1736.

(35) Izutsu, K. Acid-base dissociation constants in dipolar aprotic solvents; Blackwell Scientific Publications: Oxford, 1990.

(36) Kaila, V. R. I.; Hummer, G. *J. Am. Chem. Soc.* **2011**, 133**,** 19040.

(37) Mayer, J. M.; Hrovat, D. A.; Thomas, J. L.; Borden, W. T. *J. Am. Chem. Soc.* **2002**, *124*, 11142.

(38) Sinnecker, S.; Neese, F.; Noodleman, L.; Lubitz, W. *J. Am. Chem. Soc.* **2004**, *126*, 2613.

(39) Neese, F. *J. Phys. Chem. Solids* **2004**, *65*, 781.

(40) Yokoyama, K.; Smith, A. A.; Corzilius, B.; Griffin, R. G.; Stubbe, J. *J. Am. Chem. Soc.* **2011**, *133*, 18420.

(41) Grimme, S. *Angew. Chem. Int. Ed.* **2008**, *47*, 3430.

(42) McGaughey, G. B.; Gagné, M.; Rappé, A. K. *J. Biol. Chem.* **1998**, *273*, 15458.

(43) Holmlin, R. E.; Dandliker, P. J.; Barton, J. K. *Angew. Chem. Int. Ed.* **1997**, *36*, 2714.

(44) Cozzi, F.; Cinquini, M.; Annuziata, R.; Siegel, J. S. *J. Am. Chem. Soc.* **1993**, *115*, 5330.

(45) Cadman, C. J.; Croft, A. K. *Beilstein J. Org. Chem.* **2011**, *7*, 320.

Table 3.1 Summary of Crystallographic Data for **DPX**

	DPX
Formula	$C_{35}H_{38}O_3$
Formula weight (g/mol)	506.65
Temperature (K)	100(2)
Crystal System	Orthorhombic
Space Group	$Pna2_1$
Color	Colorless
a (Å)	10.0579(15)
b (Å)	25.425(4)
c (Å)	22.169(4)
α (°)	90
β (°)	90
γ (°)	90
V (Å ^{3})	5669.0(15)
Z	8
No. Reflections	11600
No. Unique Reflections	6587
R_{int}	0.141
$R1^a$ (all data)	0.1323
$wR2^b$ (all data)	0.1500
$R1$ [(I > 2σ)]	0.0607
$wR2$ [(I > 2σ)]	0.1235
GOF^c	0.971

^{a} $R1 = (\Sigma||F_o| - |F_c||)/\Sigma|F_o|$. ^{b} $wR2 = [\Sigma w(F_o^2 - F_c^2)^2/\Sigma wF_o^2]^{1/2}$. ^{c} GOF $= [\Sigma w(F_o^2 - F_c^2)^2/(n-p)]^{1/2}$ where n is the number of independent reflections and p is the number of refined parameters.

Calculated Structures by DFT

Cartesian coordinates (*x*, *y*, and *z* in Å) and gas-phase optimized electronic energies (in Hartrees) are provided for each **DPX**, **FPX**, **MPX**, and 4-tert-butylphenol structure employed in reduction potential and pK_a calculation:

Table 3.2. Calculated Structure of **DPX**, **FPX**, **MPX**, and 4-*tert*-butylphenol

Structure	Filename	E_{el} (Hatree)
DPX (D_0)[a]	01 DPX (+0, singlet).xyz	–1,582.91440200
DPX^{1+} (**D$_1$**)	02 DPX (+1, doublet).xyz	–1,582.67228231
DPX^{2+}, singlet	03 DPX (+2, singlet).xyz	–1,582.31077821
DPX$^{–H, 1–}$ (**D$_5$**)	04 DPX (–1, singlet, –H).xyz	–1,582.37985334
DPX$^{–H}$ (D_2)	05 DPX (+0, doublet, –H).xyz	–1,582.27681533
DPX$^{–H, 1+}$ (**D$_4$**), singlet–BS	06 DPX (+1, singlet–BS, –H).xyz	–1,582.02920248
DPX$^{–H, 1+}$, triplet	07 DPX (+1, triplet, –H).xyz	–1,582.02381825
DPX$^{–H, 2+}$, singlet	08 DPX (+2, singlet, –H).xyz	–1,581.66132928
FPX (F_0)	01 FPX (+0, singlet).xyz	–1,507.66096986
FPX^{1+} (**F$_1$**)	02 FPX (+1, doublet).xyz	–1,507.41832780
FPX^{2+}, singlet	03 FPX (+2, singlet).xyz	–1,507.05258764
FPX$^{–H, 1–}$	04 FPX (–1, singlet, –H).xyz	–1,507.10804219
FPX$^{–H}$ (F_2)	05 FPX (+0, doublet, –H).xyz	–1,507.02018137
FPX$^{–H, 1+}$ (**F$_3$**), singlet	06 FPX (+1, singlet, –H).xyz	–1,506.77344848
FPX$^{–H, 1+}$, triplet	07 FPX (+1, triplet, –H).xyz	–1,506.76130264
MPX	01 MPX (+0, singlet).xyz	–1,276.52031528
MPX^{1+}	02 MPX (+1, doublet).xyz	–1,276.27362475
MPX^{2+}, singlet	03 MPX (+2, singlet).xyz	–1,275.89711230
MPX$^{–H, 1–}$	04 MPX (–1, singlet, –H).xyz	–1,275.96395960
MPX$^{–H}$	05 MPX (+0, doublet, –H).xyz	–1,275.87918866
MPX$^{–H, 1+}$, singlet	06 MPX (+1, singlet, –H).xyz	–1,275.62747320
MPX$^{–H, 1+}$, triplet	07 MPX (+1, triplet, –H).xyz	–1,275.61321524
4-*tert*-butylphenol	01 p-tbutyl (+0, singlet).xyz	–464.90000849
4-*tert*-butylphenol$^{–H}$	02 p-tbutyl (–1, singlet, –H).xyz	–464.33412023

[a] Bolded labels in parentheses defined in Scheme 3.2.

Page intentionally left blank

Chapter 4 –

Variations on Dyad Systems

Portions of this chapter were performed in collaboration with Müge Kasanmascheff (EPR).

4.1 Introduction

We wish to understand the PCET kinetics of radical transport in the tyrosine dyad (Y_{730}-Y_{731}) in the α_2 subunit of *E. coli* ribonucleotide reductase (RNR) type Ia. In Chapter 3, we introduced the design, synthesis, electrochemical analysis, and computational analysis of PCET oxidation kinetics for **DPX**, **FPX** and **MPX** cofacial tyrosine model systems. The unique redox property of **DPX** raises intriguing questions as to the origin of its cooperativity. In this chapter, detailed thermodynamic and kinetic analysis using electronic and π-distance perturbations of the cofacial linker are presented (Scheme 4.1). A second challenge presented in Chapter 3 is that the 1 e^- oxidized species could not be isolated or detected. Under the nonaqueous electrochemical conditions employed in Chapter 3, a fast ensuing chemical process led to the 2 e^- species to be performed in an ECE mechanism. Thus we turned to other experimental methods in an attempt to characterize the 1 e^- oxidized intermediate in cofacial dyad systems. Additionally, laser spectroscopy and EPR methodologies are used to characterize the cofacial dyad systems.

Scheme 4.1 Systems to survey the redox cooperativity in the cofacial dyad.

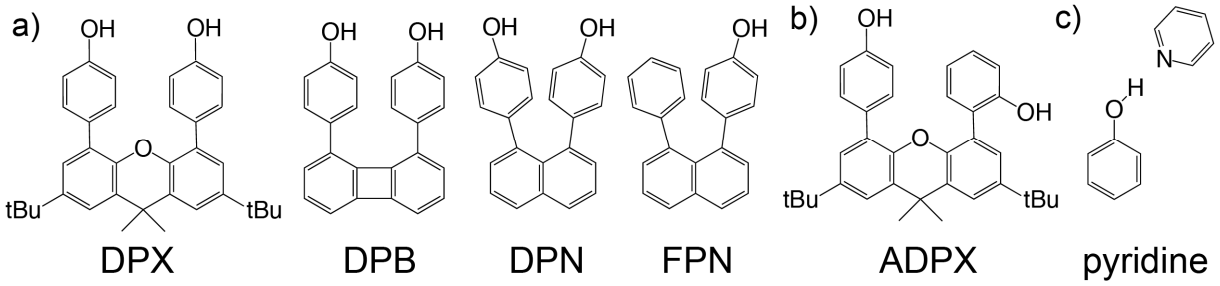

4.1.1 Variations in Structure and Hydrogen Bonding

The xanthene backbone was replaced with naphthalene[1] (**DPN** and **FPN**) and biphenylene[2] (**DPB**) to vary the distance between phenols (Scheme 4.1a). The π–ion interaction[3] and energy transfer interaction[4] between aromatic units will be affected by the different distances imposed by these spacers.

The similarity between CVs of **FPX** and **MPX** suggested to us that **DPX**'s unique property may originate from two redox active units placed in cofacial proximity and in hydrogen bonding contact. **ADPX** (Scheme 4.1) is an attractive model because each ring is a phenol (as opposed to phenol/phenyl in **FPN**), but the intramolecular hydrogen bonding network is disrupted by the regiochemistry of the hydroxyl group. The reduction potential for each moiety, 4-hydroxy benzene (*para*-xanthene phenol) and 2-hydroxy benzene (*ortho*-xanthene phenol), in **ADPX** (Scheme 4.1b) may be slightly different due to the substitution.[5] Nonetheless, **APDX** serves a good template for probing the cooperativity between redox active moieties resulting from cofacial conformation.

The CVs with strong base hydroxide (TBAOH, tetrabutylammonium hydroxide) titration demonstrate reduced **DPX** redox activity due to a mechanistic change from PCET to ET by completely removing the proton transfer coordinate.[6] Titration with pyridine, a weak base (pK_a ~12.33 in acetonitrile)[7,8], can perturb the proton transfer coordinate subtly without deprotonating phenol. In addition, pyridine is redox inactive in the CV scan range (–1.0 V to 1.6 V in MeCN). The pyridine and hydroxide titration on the dyad systems can provide the insights on the effect of proton coordinate perturbation in the redox activity.

4.1.2 Probing One Electron Photooxidation by Transient Laser Spectroscopy

The reversible PCET radical pathway of RNR transfers 1 hole (i.e., loss of an e^-) at a time. However, as discussed in Chapter 3, due to poor water solubility, **DPX** was studied in organic solvent where each phenol's 1 e^- oxidation cannot be de-convoluted from follow-up chemical steps. A **DPX** analogue in water is expected to provide a 1 e^- oxidation platform: for example, quinone undergoes a single reversible two-electron ECE oxidation in water while exhibiting

two separate reversible one-electron EC oxidations in acetonitrile.[9] Phenol undergoes 1 e^- oxidation in water while displaying a two-electron ECE oxidation in aprotic organic solvents such as acetonitrile.[10,11] We therefore wished to explore the synthetic conditions for delivering a water-soluble **DPX** analog.

An alternative strategy to study the kinetics of 1 e^- oxidations in **DPX** in nonaqueous solution is to use a photooxidant to prompt the 1 e- oxidation and transient laser spectroscopy to probe the intermediate. The time scale offered by the transient laser approach is exceptionally fast, so much so that it can capture intermediates prior to chemical steps subsequent to oxidation. As established in Chapter 2, the $^3[Re^I]^*$ (^{3}MLCT) excited state is capable of prompting photooxidation in a bimolecular quenching step. The potent oxidation power ($E^0(Re^{I*/0})$ = 1.78 V vs. NHE) affords sufficient driving force for the photooxidation to occur, as well as a sufficiently (E_p = **DPX** 1.52 V and **FPX** 1.56 V vs. NHE) long excited state $^3[Re^I]^*$ lifetime (τ_{em} ~ 3.9 μs) to enable bimolecular quenching.

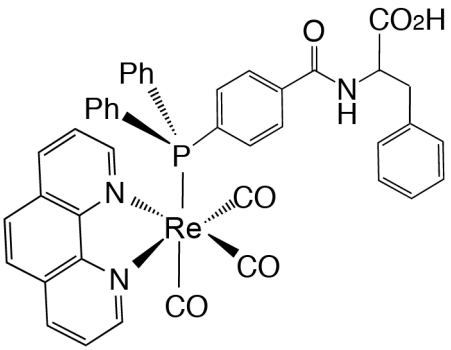

Scheme 4.2 RePF photooxidant[12] previously reported. The excited state $^3[Re^I]^*$ lifetime is τ_{em} ~ 3.9 μs and the reduction potential is $E^0(Re^{I*/0})$ = 1.78 V vs. NHE.

4.1.3 Electron Paramagnetic Resonance Spectroscopy

The phenolic radical species and intermediates of **DPX** decay quickly and thus were not able to be identified by spectroelectrochemical methods.[13] We therefore turned to characterize putative radical species of the cofacial platforms, by electron paramagnetic resonance spectroscopy (EPR). In an external magnetic field, an unpaired electron (radical) can move between two

energy levels (Figure 4.1), thus providing information regarding a paramagnetic center's electronic structure (*g* value). In principle, radicals generated by flash photolysis of the dyad models in frozen glass may allow the 1e- radical to be captured and characterized. The likelihood of capturing the radical in the solid state EPR experiment is enhanced because the phenol radical of **DPX** will invariably retain a proton after 1 e^- oxidation and thus better resemble the postulated intermediate in the electrochemical experiment, $\mathbf{D_2}$. If photolysis generates a di-radical (a radical on each phenol unit of **DPX**), this di-radical can provide the electronic structure information of the final **DPX** ECE oxidation product ($\mathbf{D_4}$, Figure 4.1). Thus the EPR experiment provides new inroads to understanding the dyad oxidation that are not available by electrochemical means.

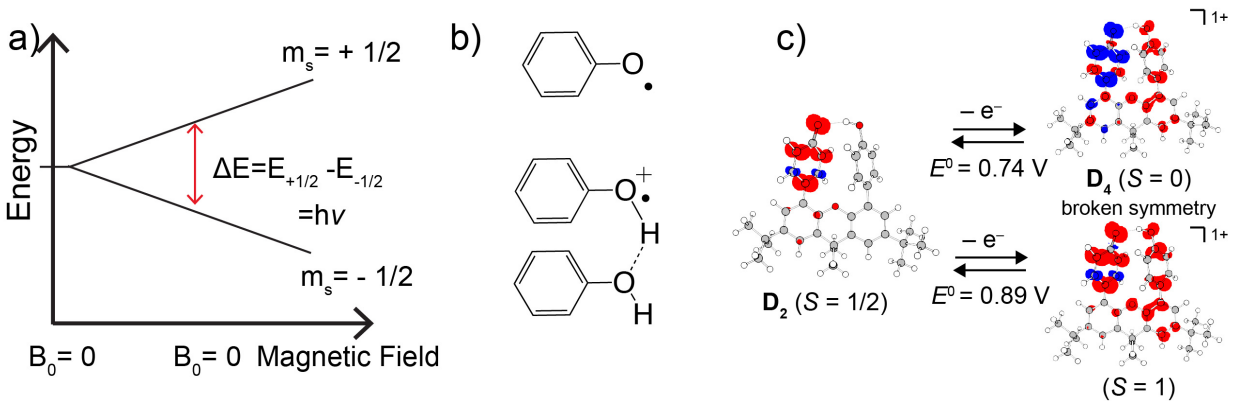

Figure 4.1 a) EPR spectroscopy energy splitting[14.] b) EPR to analyze hydrogen-bonding effects on the properties of phenoxyl radicals[15.] c) Calculated radical spin characteristics of **DPX**.

4.2 Results & Discussion

4.2.1 Synthesis of Modified Dyads

The biphenylene backbone synthon, 1,8-dibromobiphenylene, was synthesized at comparable yield to the published procedure.[16] The backbone synthons were appended with aromatic moieties via cross coupling. Aryl–aryl cross coupling between dibromo-backbone starting materials (xanthene, biphenylene and naphthalene) and boronic acid/pinacol ester afforded a modest yield cofacial dyad systems after purification (~40–60 % yield). For the synthesis of asymmetric

models (**FPN**, **ADPX**, etc.), the statistical approach (a mixture of boronic acids were used for cross coupling) showed better product yield than the sequential step-wise cross couplings. **ADPX** statistical synthesis yielded two products (**ADPX** and **DPX)** and two **2'-DPX** "ortho" conformational isomers (see Scheme 4.3) were not obtained in significant quantity (Scheme 4.3). The directing effect (*ortho*- vs. *para*-) of substituents during aryl–aryl cross coupling resulted in the difference in product yields.[17] All purified model systems were white powders and were insoluble in water.

Scheme 4.3 The products of asymmetric statistical cross coupling synthesis for **ADPX**. The major products were **DPX** and **ADPX**. **2'-DPX**s were not isolated.

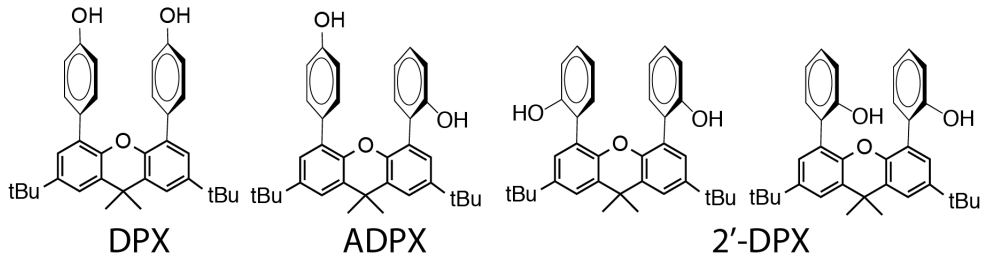

4.2.2 Structural Chemistry of Modified Dyads

The X-ray crystallographic structures for the **DPN** and **DPB** compounds shown in Figure 4.2 reveal that aromatic rings placed on naphthalene or biphenylene backbones experience strong repulsion from each other. In **DPX**, the O-O distance is 4.35 Å while the C-C distance was 4.49 Å, showing that the phenol rings were slightly bent away from each other. The C-C distance (between carbons where aromatic moieties are appended) of 2.49 Å in **DPN** is much closer than that in DPX whereas the O-O distance is 4.41 Å. For **DPB**, the crystal structure shows two different structures: one with O-O distance of 4.53 Å and another with 4.45 Å with a C-C distance of 3.84 Å in both structures. This structural metrics results in the planes of the phenol rings that are not parallel due to the repulsion between phenols (Figure 4.2. There is a slightly lesser degree of distortion of otherwise parallel planes of phenol rings in **DPB** compared to **DPN**. The closer C-C

distance causes the aromatic rings to exert stronger repulsion to each other. In the solid state, the only way to relieve the repulsion is to bend them away from each other. It is important to note that these distances are in the solid state as opposed to solution where the interplanar clashing could be relieved in other ways such as ring slippage. Notwithstanding, the X-ray structures offer us a gateway to understanding the interaction between aromatic moieties imposed by different backbones.

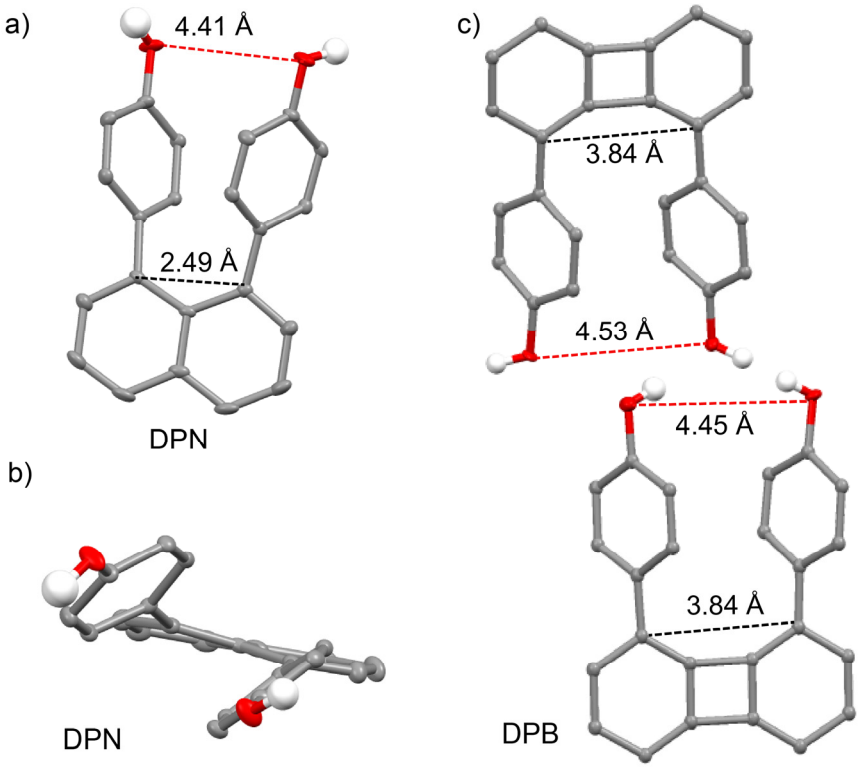

Figure 4.2 X-ray crystallographic structures of **DPN** and **DPB**. The O-O distances in **DPN** and **DPB** are larger than that of **DPX**, resulting from the electrostatic repulsion between cofacial aromatic rings. a) **DPN** O-O distance is 4.41 Å. b) **DPN** side on view shows that the phenol moieties were staggered out of the plane of the naphthalene backbone. It also shows that the planes of phenols are not parallel. c) **DPB** O-O distance 4.45/4.53 Å.

4.2.3 Electrochemistry of DPN and FPN

The xanthene of **DPX** backbone has a reversible $1e^-$ oxidation peak at a higher reduction potential than phenol that serves as a convenient internal reference. Naphthalene exhibits a simi-

lar oxidation feature (albeit not reversible) higher positive potential than phenol in aprotic organic solvent. The peak potential for the oxidation for naphthalene is E_p = 1.4 V vs. Fc^+/Fc in MeCN.[18,19] All potentials in the chapter are referenced to Fc^+/Fc. Accordingly, the electrochemistry of phenol moieties can be de-convoluted from the redox activity of backbone.

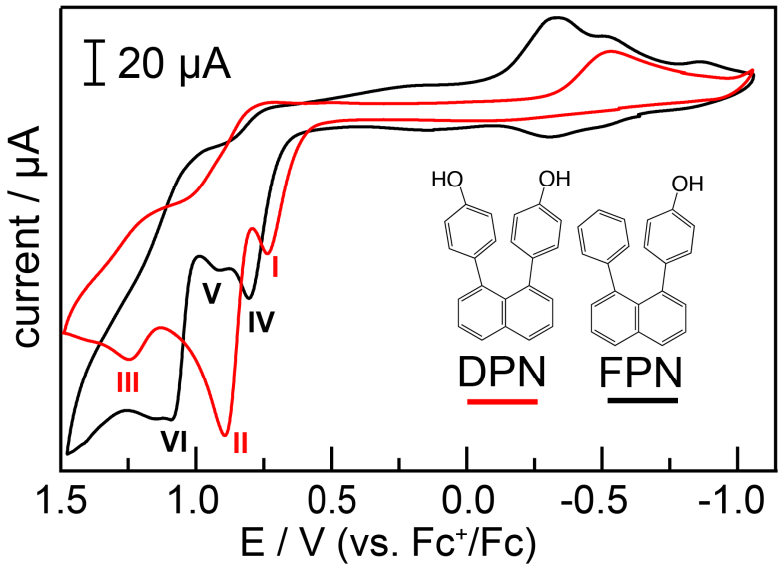

Figure 4.3 Cyclic Voltammograms of **DPN**(▬) and **FPN**(▬) in acetonitrile. Phenol oxidation was irreversible and the peak potentials are following: **DPN** peaks (E_p: peak **I** 0.74 V, **II** 0.89 V and **III** 1.25 V) and **FPN** peaks (E_p **IV** 0.81 V, **V** 0.91 V, and **VI** 1.13 V) All potentials are referenced to Fc^+/Fc.

The cyclic voltammograms of **DPN** and **FPN** shown in Figure 4.3 were obtained in 0.1 M $TBAPF_6$ acetonitrile under N_2. **DPN** showed 3 irreversible oxidation (anodic) peaks (E_p: peak **I** 0.74 V, **II** 0.89 and **III** 1.25 V) and **FPN** also showed 3 irreversible peaks (E_p: **IV** 0.81 V, **V** 0.91 V, and **VI** 1.13 V). The first two irreversible oxidation peaks around 0.8 V (vs. Fc^+/Fc) of each model were assigned to phenol oxidation. Peaks **III** and **VI** originate from the naphthalene backbone. The potentials of peaks **III** and **IV** are comparable to the reported anodic irreversible peak potential of unsubstituted naphthalene (1.4 V in MeCN).[20] Using ferrocene as an external reference, the charges associated with each CV peak of **DPN** and **FPN** were calculated. The am-

plitudes of peak **I**, **II** and **IV** corresponded to roughly a 1 e^- oxidation while peak **V** was too small to be a 1 e^- oxidation process.

The CVs of **DPN** and **FPN** with the titration of hydroxide (TBAOH) or pyridine are shown in Figures 4.4 and 4.5, respectively. The growth of current at –0.3 resulted from the phenolate generated by hydroxide (Figure 4.4). Peaks **I**, **II**, **IV** and **V**, assigned to a phenolic oxidation, were shifted upon hydroxide titration. In contrast, the peaks **III** and **VI**, assigned to naphthalene oxidation, were not shifted. As naphthalene oxidation in acetonitrile does not involve a proton transfer, the CV peak was not influenced by the presence of hydroxide.

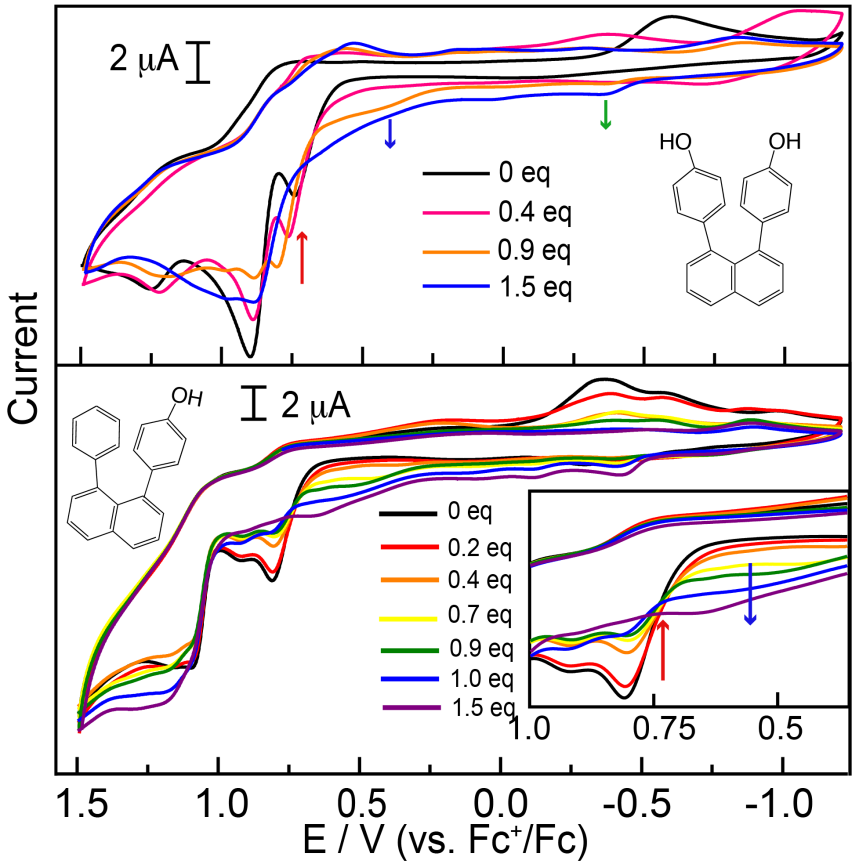

Figure 4.4 Cyclic voltammograms of **DPN** (top) and **FPN** (bottom) titration with tetrabutylammonium hydroxide in acetonitrile. **DPN**: 0 equiv. (▬), 0.4 equiv. (▬), 0.9 equiv. (▬), and 1.5 equiv. (▬). **FPN**: 0 equiv. (▬), 0.2 equiv. (▬), 0.4 equiv. (▬), 0.7 equiv. (▬), 0.9 equiv. (▬), 1.0 equiv. (▬) and 1.5 equiv. (▬).

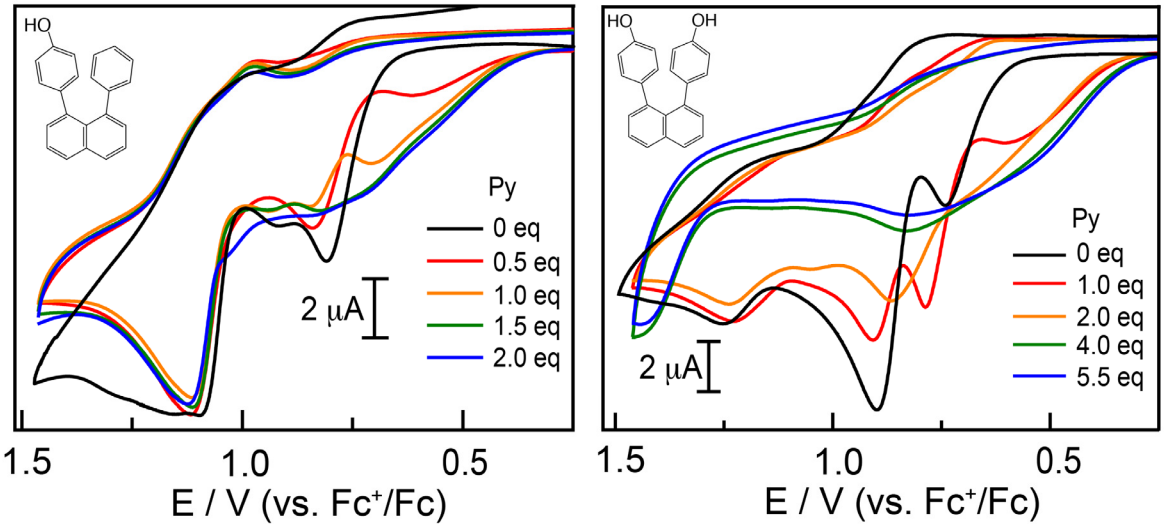

Figure 4.5 Cyclic voltammograms of **FPN** (left) and **DPN** (right) titration with pyridine. The equivalency of pyridine is noted as per molecule. **FPN**: 0 equiv. (▬), 0.5 equiv. (▬), 1.0 equiv. (▬), 1.5 equiv. (▬), and 2.0 equiv. (▬). **DPN**: 0 equiv. (▬), 1.0 equiv. (▬), 2.0 equiv. (▬), 4.0 equiv. (▬), and 5.5 equiv. (▬).

The growth of shoulder peak at ~300 mV lower potential was observed in both **DPN** and **FPN** and coincides with the decrease of phenol oxidation peaks (Peak **I** and **IV**, Figure 4.5). As for the titration of **DPX** with pyridine, this peak is attributed to a CPET 1 e^- oxidation. Both **DPN** and **FPN** required ~2 equiv. pyridine per phenol moiety to reach the maximum CPET peak amplitude.

Pyridine titration resulted in the CPET pathway promotion for **DPN** and **FPN**. In acetonitrile, the ECE peak is observed because the first 1 e^- oxidation product rapidly deprotonates to generate neutral phenol radical. The reduction potential of the radical is lower than the starting material, phenol thus the follow-up 2nd 1 e^- oxidation occurs instantaneously, resulting in ECE peak. In this regard, one possible explanation for the observed overall 1 e^- oxidation for **DPN** and **FPN** is that the associated pyridine prevents deprotonation of the radical cation, by effectively binding the proton in a hydrogen bond complex. Without the deprotonation, the follow-up 2nd oxidation does not occur in the scanned potential range.

The pK_a of pyridinium is known to be much lower than phenol, (pK_a PyH^+ = 0.6),[6] and therefore proton transfer to pyridine, thus generating pyridinium, is unlikely. Rather, pyridine and phenol are strongly associated and upon oxidation of phenol, proton shift is likely with the pyridinium species contained within the associated complex: pyridine···phenol $\xrightarrow{-e^-}$ phenolic radical···pyridinium. It is known that appended bases in hydrogen bonded contact to phenol support the latter's 1 e^- oxidation.[11] A characteristic of this condition is that the 1 e^- oxidation is reversible. The enhanced hydrogen-bonding network in phenol with pyridine was shown to promote CPET.[21–24]

Similar to the case of **DPX** pyridine titration, the CPET peaks of **FPN** and **DPN** were not reversible. Instead, the large shift of ETPT waves (in the absence of pyridine) to less oxidizing potentials and loss of reversibility on a cathodic scan suggests that pyridine associated to phenols can promote CPET reaction by serving as a proton acceptor. If pyridine-phenol complex persisted after CPET oxidation, the pyridinium would serve as a proton donor for the phenol reduction process. The pyridine-phenol complex may dissociate quickly after oxidation thus the corresponding reduction peak of phenol was not observed.

4.2.4 Electrochemistry of ADPX

CVs of **ADPX** were obtained in 0.1 M $TBAPF_6$ electrolyte in dry acetonitrile (Figure 4.6). In the anodic scan, three irreversible peaks were observed; E_p= 0.88 V (peak **I**), 1.07 V (Peak **II**) and 1.23 V (Peak **III**). Using one equiv. of ferrocene as a reference, peak **I** was calculated to be 2 e^- process and peak **II** to be 1 e^- process. The peak potential of peak **I** was comparable to the first phenolic oxidation peak of **DPX** (E_p = 0.88 V). The 1 e^- reversible xanthene

backbone peak observed in **DPX** appeared quasi-reversible in **ADPX**. **ADPX** phenols undergo 3 e^- oxidations in contrast to the 2 e^- ECE process of **DPX**.

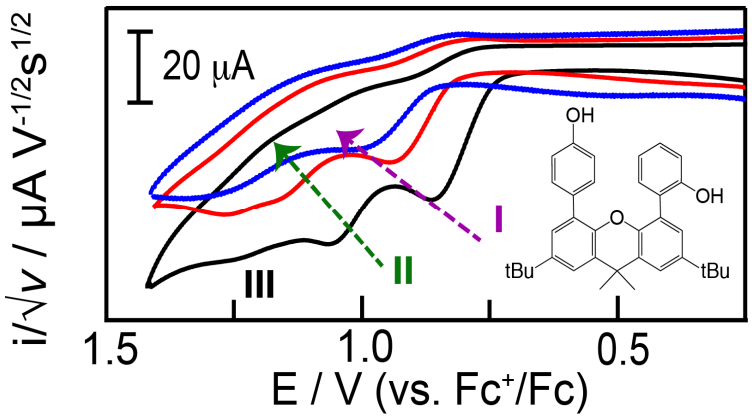

Figure 4.6 Cyclic voltammograms of **ADPX** at varying scan rate. 0.1 V/s (black), 1 V/s (red) and 10 V/s (blue). **APDX** peak **I** peak potential shift as scan rate increases: E_p 0.88 V (0.1 V/s), 0.94 V (1 V/s), and 1.01 V (10 V/s). The violet dotted arrow shows the shift of Peak **I.** The green dotted arrow shows the shift of Peak **II**.

The scan-rate dependence of **ADPX** CV peaks was obtained to characterize the involvement of chemical steps with each oxidation process (Table 4.1). The shifts of peaks **I** and **II** are indicated by the violet and green arrows, accordingly. Peak **I** exhibits a peak potential dependence on scan rate of ~60 mV/decade, suggesting the coupling of a chemical step with each electron transfer step.[25] At a faster scan rate, peaks **II** and **III** coalesce.

Table 4.1 The scan rate dependence of **APDX** peak potential (E_p)

Peak	**ADPX**			**DPX**
	0.1 V/s	1.0 V/s	10 V/s	0.1 V/s
I	0.88 V	0.94 V	1.01 V	0.88 V
II	1.07 V	1.16 V	1.33 V	0.98 V
III	1.23 V	1.27 V		1.29 V

DPX cooperativity is hypothesized to arise from: i) the proximal cofacial placement of redox active units that create redox cooperativity, distinct from individual unit; and ii) the internal hydrogen bonding of **DPX** may be responsible for two phenols experiencing 2 e^- oxidations.

ADPX serves as a **DPX** analogue without the internal hydrogen bonding possibility. Unlike the phenol hydroxyl groups of **DPX**, which are aligned in parallel, the phenol hydroxyl groups of **ADPX** are staggered. Thus, there is no internal hydrogen bonding in **ADPX** in any conformation. The CV of **ADPX** is different from CVs of **DPX**, **FPX** and **MPX**. The involvement of the phenolic moiety might be responsible for quasi-reversibility of xanthene backbone oxidation. Especially, the 2-hydroxy phenol group may assist electrochemical decomposition in xanthene backbone under the oxidative stress.

4.2.5 Photogeneration of One Electron Oxidized Species by Bimolecular Quenching

The ground state electronic absorption spectra of model systems were obtained at room temperature in acetonitrile and shown in Figure 4.7. All dyad model systems (**DPX**, **ADPX**, **FPX**, **DPN**, **FPN**, and **DPB**) show no absorption at 355 nm, thus allowing the samples to be cleanly excited by the laser (λ_{exc} = 355 nm). The peak at 254 nm in **DPX** appears broadened with a shoulder feature in **ADPX** (λ_{max} = 250 nm). **ADPX** is a "lowered" symmetry analogue of **DPX** where the removal of degeneracy resulted in the additional absorption feature (shoulder) that is similarly observed in UV-vis spectra of **MPX** and **DPX** (Figure 3.7).

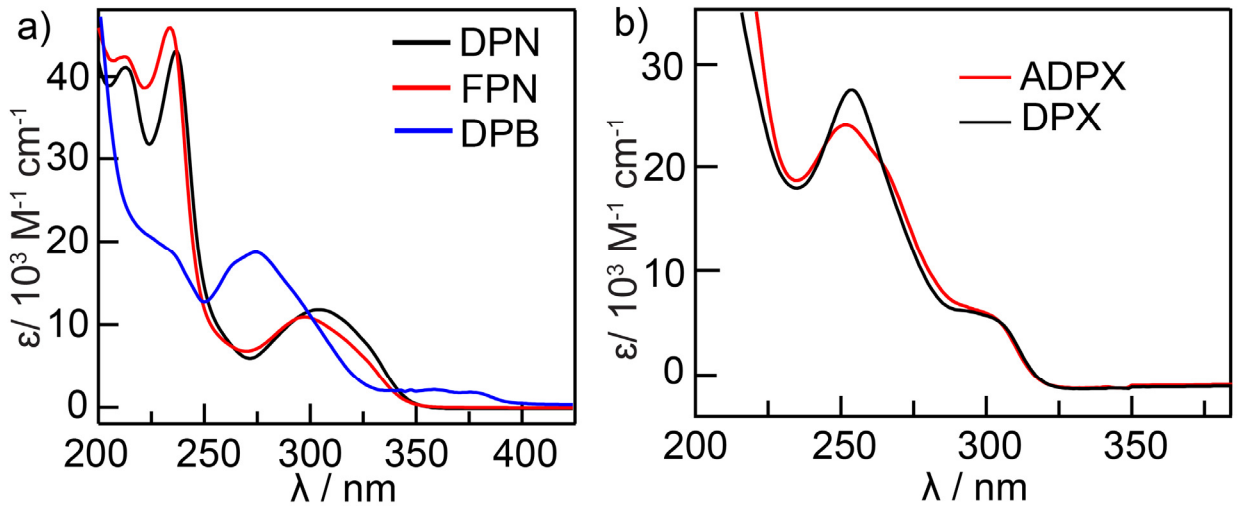

Figure 4.7 a) Electronic absorption spectra of **DPN** (λ_{max} = 240 nm, 305 nm), **FPN** (λ_{max} = 235 nm, 295 nm), and **DPB** (λ_{max} = 238 nm, 275 nm) 25 μM in acetonitrile. b) Electronic absorption spectra of **DPX** (λ_{max} = 254 nm, 302 nm) and **ADPX** (λ_{max} = 250 nm, 300 nm, shoulder ~265 nm), 25 μM in acetonitrile.

The driving force of the bimolecular quenching experiment was determined using the peak potentials E_p and calculated E^0 values (Table 4.2). Based on the electrochemical peak potentials of **DPX** and **FPX**, the driving forces for each oxidation by $^3[Re^I]^*$ ^{3}MLCT states are 0.26 eV and 0.22 eV, accordingly. The driving force for **ADPX**, **DPN** and **FPN** were estimated to be 0.26 eV, 0.40 eV and 0.32 eV, respectively.

The excited state lifetime τ_{obs} of the different dyads was monitored at 600 nm and 3 different samples were used to obtain average values. Each measurement was made in the acetonitrile solution with a photooxidant RePF (Figure 4.8) 50 μM; [Q] (Q= quenchers, model systems quench the excited state of RePF) concentration ranged from 50 μM (1 equiv.) to 500 μM (10 equiv.). The $^3[Re^I]^*$ ^{3}MLCT state of Re-PF has a transient absorption feature at 410 nm (phenol radical λ_{max}) (Figure 4.8) thus the TA spectra for the mono-phenolic (**FPX**) and corresponding di-phenolic systems (**DPX**) are obtained by subtracting TA at 40 ns after the 355 nm excitation.

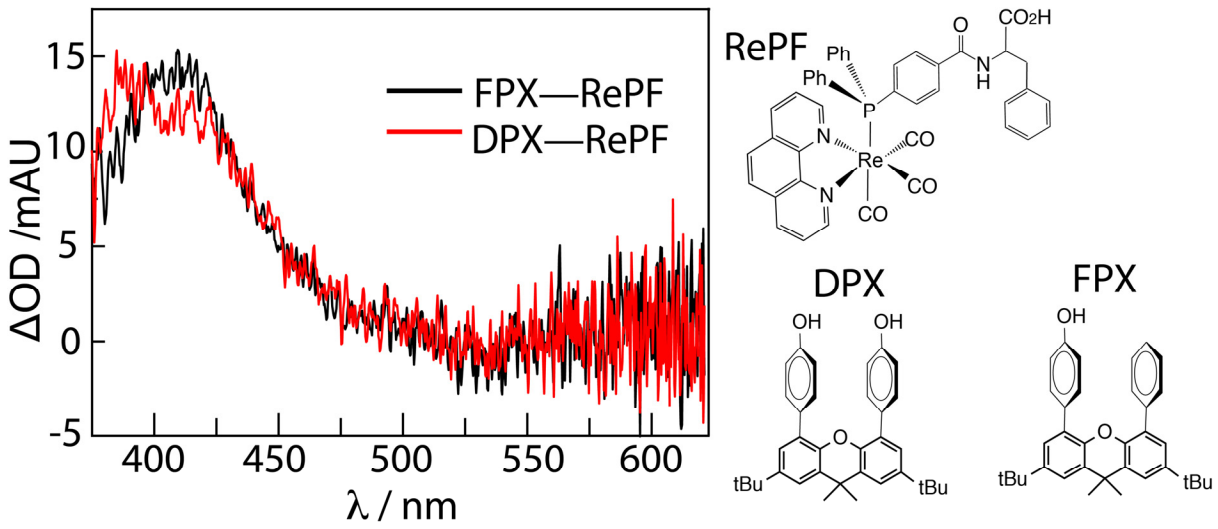

Figure 4.8 The subtracted TA spectra showing **DPX** (red) and **FPX** (black) radical species (λ = 410 nm). The subtracted spectra were obtained with the TA spectra of Re-PF, Re-PF+**DPX** and Re-PF+**FPX** 40 ns after the 355 nm excitation. Re-PF was 50 μM and **DPX** and **FPX** were 0.3 mM in acetonitrile.

The Stern-Volmer plots are provide in Figure 4.9.[26] The observed emission lifetimes against varying quencher (model system) concentrations were used to calculate the quenching rate constant k_q with the Stern-Volmer equation,

(Eq. 4.1) $$\frac{I_f^0}{I_f} = \frac{\tau_0}{\tau} = 1 + k_q \tau_0 [Q]$$

where [Q] is the concentration of the quencher (model systems), I_f^0 is the intensity (rate of fluorescence) without a quencher, I_f is the intensity with a quencher, τ_0 is the lifetime of the emissive excited state (^{3}[Re]^{I*} of Re-PF). The calculated k_qs are provided in Table 4.2 along with the calculated driving force of the quenching process.

Table 4.2 The comparison of experimental peak potential (E_p), reduction potential from computation, driving force and bimolecular quenching rates.

Model	E_p[a]	E^0 (from DFT)[b] E^{0a}	kq / ($M^{-1}s^{-1}$) Bimolecular Quenching	$-\Delta G^0$
DPX	1.52	0.68[b]/ 1.32[a]	$4.31 \pm 0.05 \times 10^9$	0.46 eV[c], 0.26 eV[d]
FPX	1.56	0.72[b]/ 1.36[a]	$2.73 \pm 0.04 \times 10^9$	0.42 eV[c], 0.22 eV[d]

ADPX	1.52		$2.31 \pm 0.13 \times 10^9$	0.26 eV[d]
DPN	1.38		$7.77 \pm 0.26 \times 10^9$	0.40 eV[d]
FPN	1.46		$6.09 \pm 0.08 \times 10^9$	0.32 eV[d]

[a] vs. NHE. [b] reference 18 computational data. [c] $E^0(Re^{I*/0}) = 1.78$ V (vs. NHE), $-\Delta G=(E^{0a}{}_{\text{model system}})-E^0(Re^{I*/0})$. [d]Driving force calculated with E_p serves as an upper limit for the driving force. $-\Delta G=(E_p{}^a{}_{\text{model system}})-E^0(Re^{I*/0})$.

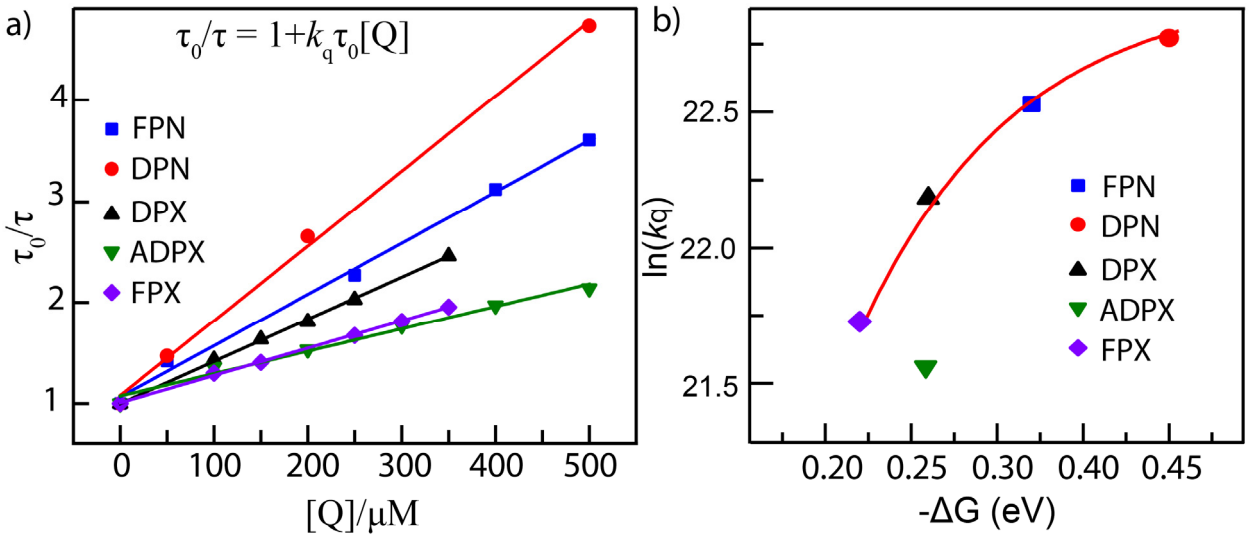

Figure 4.9 a) Bimolecular quenching of $^3[Re^I]^*$ [RePF] by each model system. The measurements were made in the acetonitrile solution with [RePF] 50 μM, [Q] (model systems) concentration ranged from 50 μM (1 equiv.) to 500 μM (10 equiv.), **FPN** (blue square), **DPN** (red circle), **DPX** (black triangle), **ADPX** (green inverted triangle), and **FPX** (violet diamond). b) The plot of ln(k_q) vs. $-\Delta G=(E_p{}^a{}_{\text{model system}})-E^0(Re^{I*/0})$. The plot shows that the observed bimolecular quenching rate constants are not diffusion limited.

All rate constants are in the range of 2–8 × 10^9 M^{-1} s^{-1}, near the diffusion-controlled rate limit. The rate constant of **DPX** was 1.6 times larger than the rate constant of **FPX** while the driving force difference was only 40 meV bigger. This result implies that the structure of **DPX** perturbs the kinetics of electron transfer in addition to the energetics of the phenol oxidation reaction. The rate constant of **DPN** was 1.3 times larger than the rate constant of **FPN** while the driving force difference was 80 meV higher. The comparison between naphthalene based models (**FPN**, **DPN**) and xanthene based models (**DPX**, **ADPX**, **FPX**) is challenging because the two

sets of systems have vastly different parameters such as diffusion coefficient, reorganization energy and molecular dipole moment. Also, the driving force for **FPN** and **DPN** bimolecular quenching experiments was calculated from the electrochemical peak potentials.

The plot of ln(k_q: dyad oxidation by RePF) against the driving force is provided in Figure 4.9b. The diffusion-limited rate constant[27] was assumed to be $1.2 \times 10^{10}\ M^{-1}\ s^{-1}$ and the curvature of the plot confirms that they are not diffusion-limited. The difference between the electrochemical peak potential and E^0 may be responsible for the aberration of **ADPX** (Figure 4.9b). In summary, the bimolecular quenching rates show that one electron phenol oxidation, if de-convoluted from the ensuing deprotonation or second oxidation, belongs to the normal region of Marcus-Hush ET regimes. [28, 29]

4.2.6 EPR Experiments

The electron spin echo (34 GHz) experiments were performed with **DPX**, **ADPX** and **FPX** and spectra are shown in Figure 4.10.

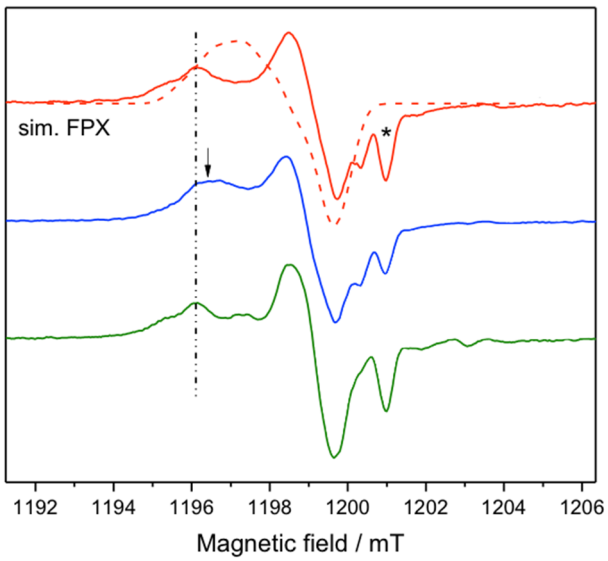

Figure 4.10 Derivative of the electron-spin-echo (ESE) spectra of **FPX** (red), **DPX** (blue) and

ADPX (green) in CH_3CN recorded at 34 GHz. The corresponding simulation for **FPX** is shown with red dashed line.

The g_x value of **DPX**, which is marked with an arrow, is shifted compared to that of **FPX** and **ADPX**. This might be due to the hydrogen bonding between two phenols in **DPX**. ^{2}H Mims-ENDOR experiment can elucidate the hydrogen bonding of radical species. To gain sensitivity in the ^{2}H Mims-ENDOR experiments, the deuterated analogues of xanthene model systems are to be prepared (Scheme 4.4).

Scheme 4.4 Synthesis of d_8-**DPX** and d_4-**FPX** for the ^{2}H Mims-ENDOR experiment.

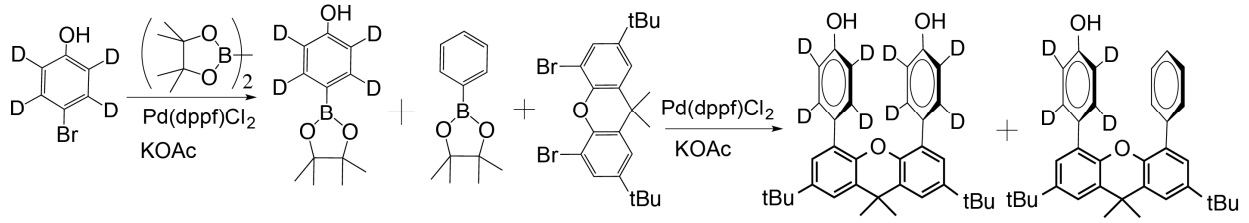

4.3 Conclusion

Modifications of the phenol dyad motif introduced in Chapter 3 were further explored by varying the electronic properties of the phenol and π-distance (4.35–4.45 Å) of phenols from each other. The variation of phenol moieties distance was achieved by utilizing naphthalene and biphenylene backbones. The variation on the hydrogen-bonding network was produced by external base pyridine titration and by synthesizing regiomers of phenol moiety. Without a proton acceptor, phenol oxidation in acetonitrile undergoes ET followed by PT. The proton transport occurs subsequently due to the low pK_a of the phenolic radical cation. With the addition of weak bases, the ETPT CV waves shift ~300 mV to lower positive potential and a single wave is observed, consistent with a CPET phenol oxidation pathway.[30] Transient laser spectroscopy shows that **DPX** and **FPX** radicals are phenolic radicals, although TA cannot distinguish the two radical

species. The bimolecular quenching experiments showed the dependence of bimolecular quenching rate on the driving force belongs to the normal region of Marcus-Hush ET analysis. ESE EPR data showed that **DPX**, **FPX** and **ADPX** radicals have different g_x values, indicative of the different electronic environment for each radical.

4.4 Experimental Details

4.4.1 Synthesis and Materials

Materials. 2,7-Di-tert-butyl-4,5-dibromo-9,9-dimethyl-xanthene, (4-hydroxyphenyl)boronic acid, (2-hydroxyphenyl boronic acid), (4-hydroxyphenyl)boronic acid pinacol ester, phenyl boronic acid pinacol ester, 5-indolylboronic acid, 4-nitrophenylboronic acid, N,N-dimethyl formamide (DMF), 1,4-dioxane, anhydrous copper chloride ($CuCl_2$), 9,9-dimethyl-xanthene, *n*-butyllithium (2.5 M in hexanes, ^nBuLi), 2,5-dibromoaniline, zinc bromide ($ZnBr_2$), tin chloride ($SnCl_2$), 1,8-dibromonaphthalene, sodium sulfate (Na_2SO_4), naphthalene, cesium fluoride (CsF) (Sigma Aldrich), tetrakis(triphenylphosphane) palladium(0) ($Pd(PPh_3)_4$), [1,1'-bis(diphenylphosphino)-ferrocene]palladium(II) dichloride ($Pd(dppf)Cl_2$) (Strem), sodium nitrite ($NaNO_2$), potassium iodide (KI), and potassium carbonate (K_2CO_3) (Mallinkrodt) were used as received. 4-bromophenol-2,3,5,6-D_4 was purchased from Alfa Chemistry.

Scheme 4.5 Synthesis of dyad model systems with biphenylene and naphthalene backbones. a) Biphenylene was synthesized following published methods.[16] b)–d) The yield of purified statistical mixture of cross-coupling products were higher than the yield of sequential asymmetric cross coupling products.

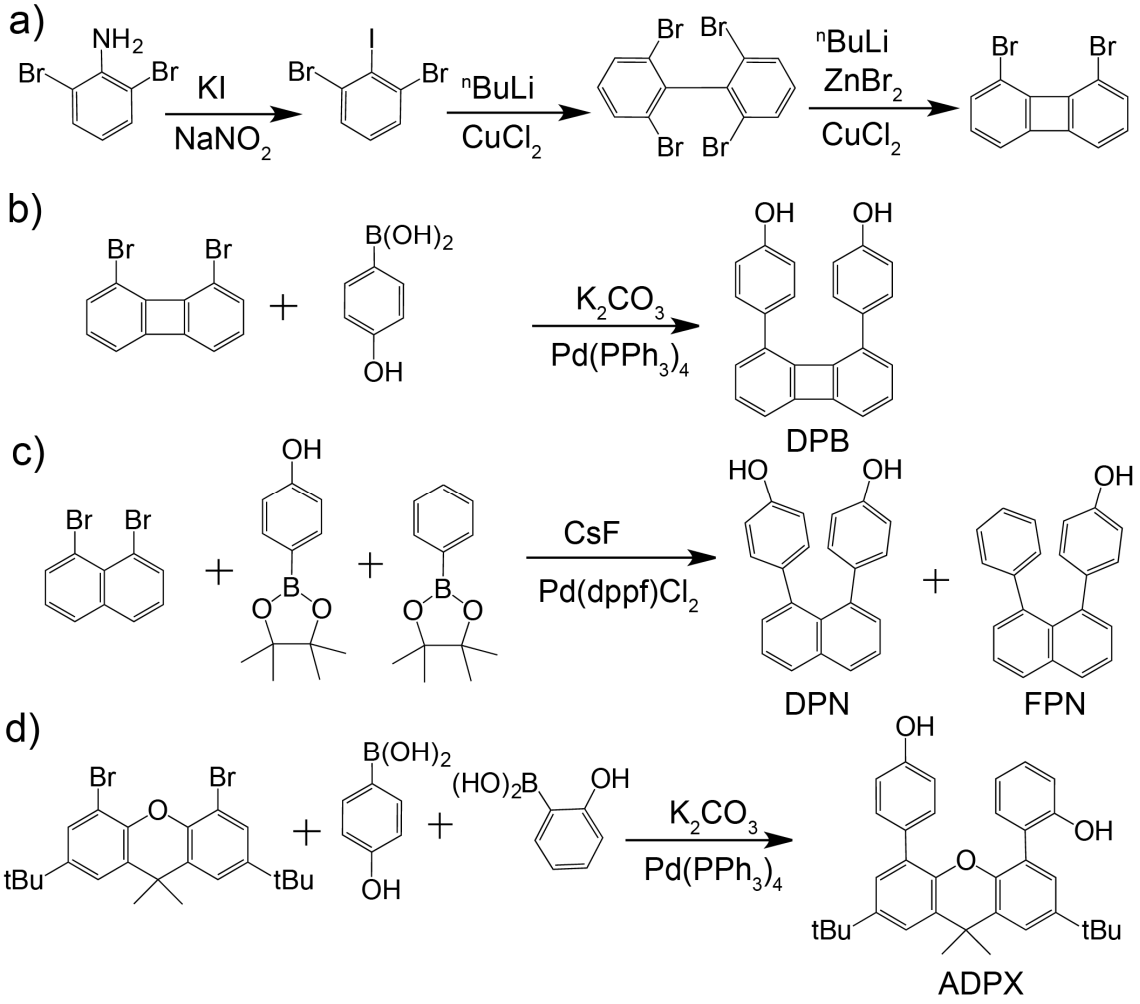

1,8-Dibromobiphenylene : Scheme 4.5a applies to this synthesis. 1,8-Dibromobiphenylene was prepared following published procedures.[16]

^{1}H NMR (500 MHz, d_1-$CDCl_3$): δ = 6.84 (m, 2H), 6.65 (dd, 2H), 6.58 (m, 2H).

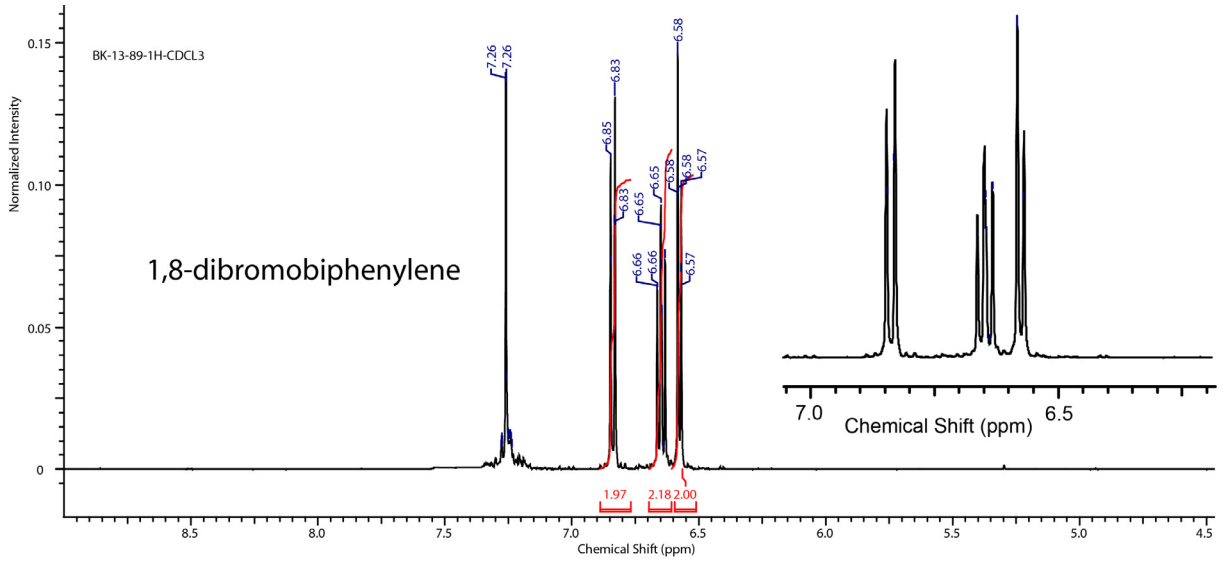

Figure 4.11 ^{1}H NMR spectrum of 1,8-dibromobiphenylene in d_1-$CDCl_3$. The peak at 7.26 ppm is a solvent peak ($CHCl_3$).

1,8-di(4-hydroxy)benzylbiphenylene (**DPB**): Scheme 4.5b applies to this synthesis. A sample of 1,8-dibromobiphenylene (100 mg, 0.324 mmol, 1.00 equiv.), 4-hydroxyphenyl boronic acid (150 mg, 1.27 mmol, 4.00 equiv.), K_2CO_3 (179.2 mg, 1.296 mmol, 4.00 equiv.), $Pd(PPh_3)_4$ (24.8 mg, 0.032 mmol, 0.1 equiv.) were added to 40.0 mL of 9:1 DMF: water mixture in a 100 mL Schlenk flask. The mixture was heated at reflux overnight under N_2 and then cooled to room temperature after which 100 mL of distilled water was added to the flask. The product was extracted with di-chloromethane (DCM), and a solid was obtained upon drying under vacuum. The products (**DPB**: R_f ~0.9) were purified by column chromatography (DCM: hexanes (1:4) → DCM → DCM: ethyl acetate (3:1)) and obtained as white solids (65 mg, 59 %).

DPB ^{1}H NMR (500 MHz, acetone-d^6): δ = 6.84 (m, 4H, bp), 6.78 (m, 4H, phenol), 6.68 (dd, 2H, bp), 6.45 (m, 4H, phenol).

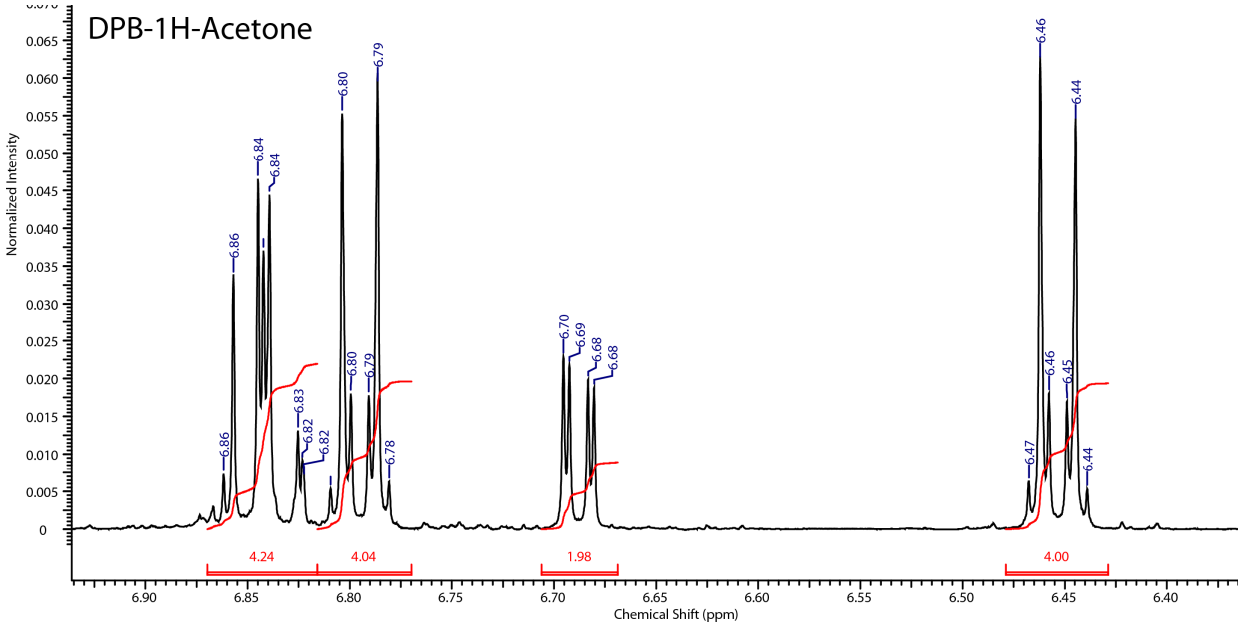

Figure 4.12 ^{1}H NMR spectrum of **DPB** in d_6-Acetone.

1,8-di(4-hydroxy)phenylnaphthalene (**DPN**) and 1-(4-hydroxy)phenyl-8-phenylnaphthalene (**FPN**): Scheme 4.5c applies to this synthesis. 1,8-Dibromonaphthalene (300 mg, 1.04 mmol, 1.00 equiv.), phenyl boronic acid pinacol ester (321 mg, 1.57 mmol, 1.50 equiv.), 4-hydroxyphenyl boronic acid pinacol ester (346 mg, 1.57 mmol, 1.50 equiv.), K_2CO_3 (580 mg, 4.19 mmol, 4.00 equiv.), $Pd(dppf)Cl_2 \bullet CH_2Cl_2$ (82.01 mg, 0.10 mmol, 0.1 equiv.) were added to 30.0 mL of a 9:1 mixture of 1,4-dioxane and water in a 250 mL Schlenk flask. The mixture was heated at reflux overnight under N_2 and then cooled to room temperature after which 400 mL of distilled water was added to the flask. The product was extracted with DCM, and a solid was obtained upon drying under vacuum. The products (**DPN**: $R_f \sim 0.9$, **FPN**: $R_f \sim 0.6$ DCM) were purified by column chromatography (DCM: hexanes (1:4) → DCM → DCM: ethyl Acetate (3:1)) and obtained as white solids (**DPN** 114 mg 35 % and **FPN** 74 mg 24%).

DPN ^{1}H NMR (500 MHz, d$_4$-MeOD): δ = 7.92 (dd, 2H, np), 7.52 (m, 2H, np), 7.35 (m, 2H, np), 6.77 (m, 4H, phenol), 6.42 (m, 4H, phenol).

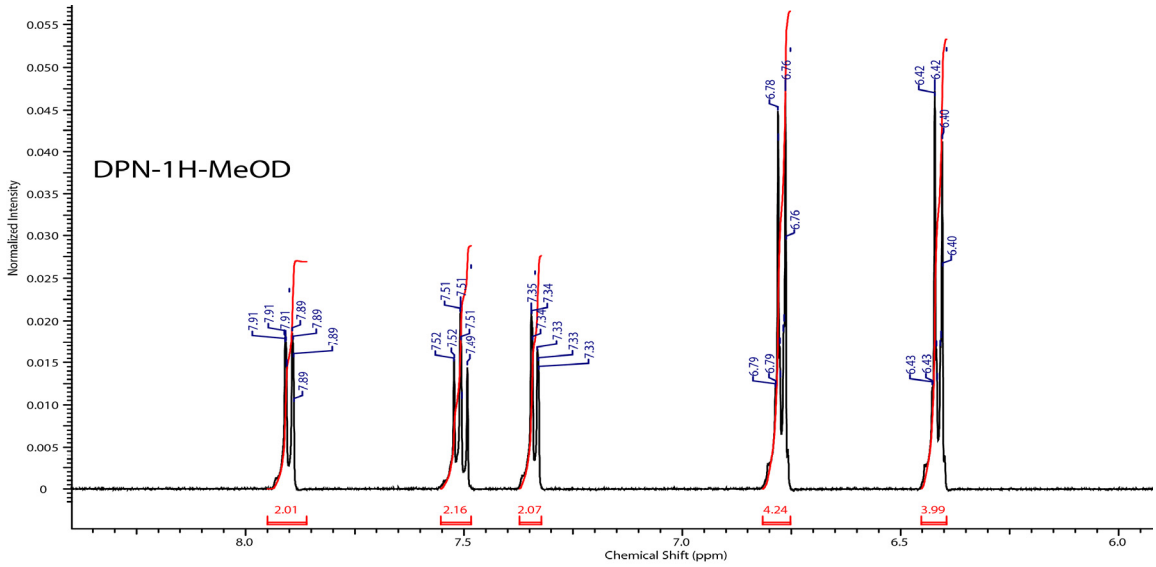

Figure 4.13 ^{1}H NMR spectrum of **DPN** in d$_4$-CD$_3$OD.

FPN ^{1}H NMR (500 MHz, d$_4$-MeOD): δ = 7.90 (m, 2H, np), 7.50 (m, 2H, np), 7.34 (m, 2H, np), 6.91 (m, 5H, benzyl), 6.72 (m, 2H, phenol), 6.35 (m, 2H, phenol).

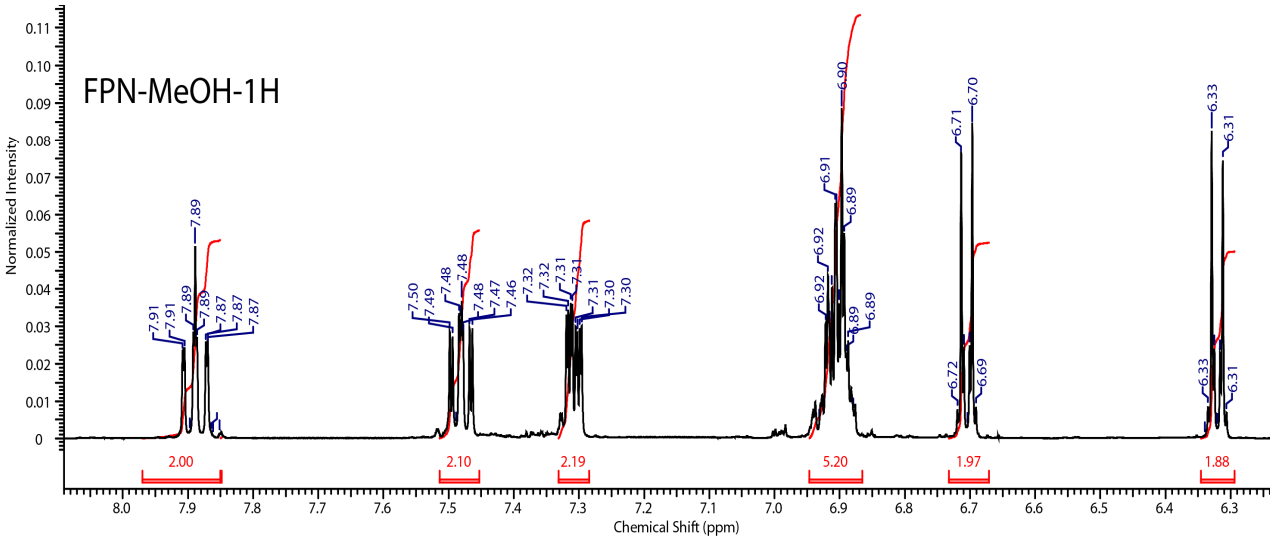

Figure 4.14 ^{1}H NMR spectrum of **FPN** in d$_4$-CD$_3$OD.

2,7-di-tert-butyl-4-(2-hydroxyphenyl)-5-(4-hydroxyphenyl)-9,9-dimethyl-xanthene (**ADPX**):

Scheme 4.5d applies to this synthesis. 2,7-Di-tert-butyl-4,5-dibromo-9,9-dimethyl-xanthene (550 mg, 1.15 mmol, 1.00 equiv.), 4-hydroxyphenyl boronic acid (151.96 mg, 2.30 mmol, 2.00 equiv.), 2-hydroxyphenyl boronic acid (151.96 mg, 2.30 mmol, 2.00 equiv.), K_2CO_3 (633 mg, 4.58 mmol, 4.00 equiv.) and $Pd(PPh_3)_4$ (132 mg, 0.114 mmol, 0.100 equiv.) were added to 200 mL of a 9:1 DMF:water mixture in a 500 mL round-bottom flask. The mixture was heated at reflux overnight under N_2 and then cooled to room temperature after which 300 mL of distilled water was added to the flask. The product was extracted with DCM, and a solid was obtained upon drying under vacuum. **DPX** (majority) and **ADPX** products were purified by column chromatography (hexanes/DCM) to deliver a white solid (310 mg, 73.5%).

DPX ^{1}H NMR (500 MHz, CD_2Cl_2): δ = 7.40 (d, 2H), 7.17 (d, 2H), 7.12 (m, 4H), 6.66 (m, 4H), 1.71 (s, 6H), 1.35 (s, 18H).

ADPX ^{1}H NMR (500 MHz, CD_3OD): δ = 7.48 (dd, 1H), 7.42 (dd, 1H), 7.14 (m, 6H), 7.07 (m, 1H), 6.98 (m, 1H), 6.75 (m, 2H), 6.47 (m, 2H), 1.70 (s, 6H), 1.34 (s, 18H). *m/z* (ESI) (Calc.) 507.2894 (found) 507.2871 $[M+H]^+$.

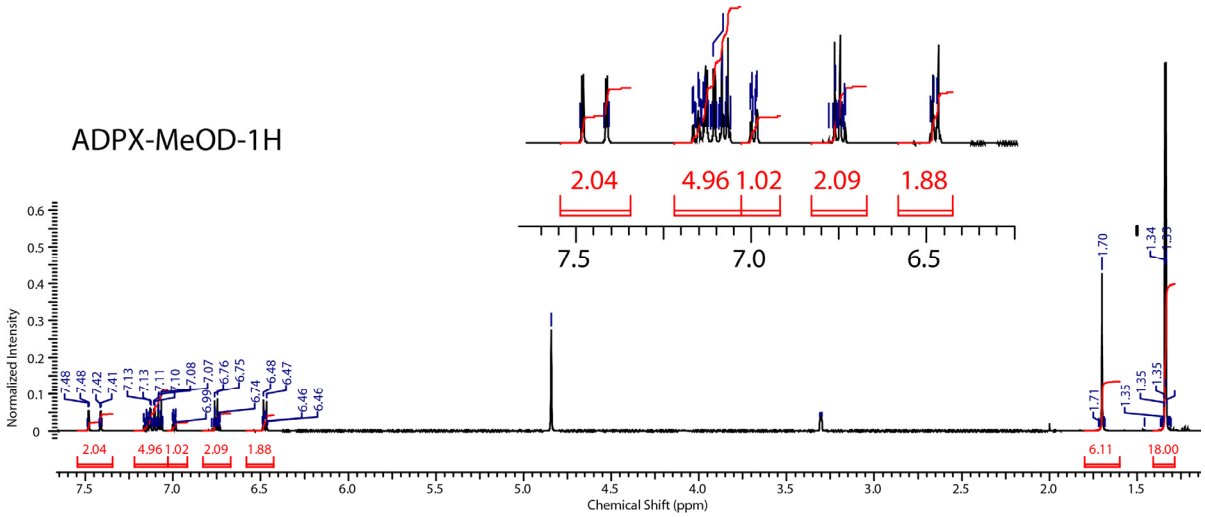

Figure 4.15 ^{1}H NMR spectrum of **ADPX** in d_4-CD_3OD. Peaks at 4.8 and 3.3 ppm are solvent peaks (MeOH).

4.4.2 X-ray Crystallographic Details

Diffraction quality crystals of **DPN** and **DPB** were obtained by slow evaporation of a 1:1 mixture of hexane and DCM, affording crystals as clear blocks; a single crystal was cut from a larger one for the X-ray diffraction study. Low temperature (100 K) X-ray diffraction data was collected on a Bruker three-circle platform goniometer equipped with an Apex II CCD detector and an Oxford cryostream cooling device, performing φ- and ω- scans. Radiation was generated from a graphite fine focus sealed tube Mo Kα (0.71073 Å) source. Crystals were mounted on a cryoloop using Paratone-*N* oil. Data were processed and refined using the program SAINT supplied by Siemens Industrial Automation. Structures were solved by intrinsic phasing methods in SHELXT and refined by standard difference Fourier techniques in the SHELXTL program suite. Hydrogen atoms were located in the difference map and were refined isotropically using a riding model; all non-hydrogen atoms were refined anisotropically. Unit cell parameters, morphology, and solution statistics for the structure are summarized in Table 4.3. Thermal ellipsoid plots are drawn at the 50% probability level with hydrogen atoms removed for clarity.

4.4.3 Electrochemical Methods

Electrochemical measurements were performed on compounds dissolved in acetonitrile in a nitrogen atmosphere glove box at room temperature. Voltammetric experiments were conducted with computer controlled CH Instruments 760D Electrochemical Workstation using CHI Version 10.03 software. A three-electrode cell with a 1 mm diameter planar platinum working electrode was used together with a platinum wire counter electrode. A platinum wire reference electrode was used as a pseudo-reference and all CVs were referenced to Fc^+/Fc. Acetonitrile (ACS, 99.95%, Aldrich) was purified on a Glass Contour Solvent Purification System manufactured by SG Water and kept over activated 3 Å molecular sieves overnight under nitrogen. The residual water in acetonitrile was less than ~2 ppm by Mettler Toledo C20 compact Karl-Fischer coulometer. For pyridine titration experiments, the concentrated stock solution of base (i.e. pyridine in MeCN, 0.5 M to 50 mM) was used to ensure less than ~1% of total analyte solution volume increase at the end of titration.

4.4.4 Laser Spectroscopy

Nanosecond timescale laser spectroscopy experiments utilized a system that has been reported.[31] For the experiments reported in this chapter, a few modifications were made. Firstly, the samples were freeze-pump-thaw degassed to 10^{-5} Torr. The 500 nm blaze grating (300 grooves/mm) was used for emission kinetics measurement for bimolecular quenching. All experiments were performed in room temperature. The entrance and exit slits for the monochromator were 0.2 mm for emission kinetics experiments and they correspond to a spectral resolution of 2.5 nm.

4.4.5 Absorption Measurements

UV-vis spectra were recorded on a Varian Cary 5000 UV-vis-NIR spectrophotometer using 1 cm path length 6Q quartz cell. For TBAOH titration, a 1.0 M methanol solution obtained from Sigma Aldrich was used as received. The analyte sample was made in a N_2-atmosphere glove box. For pyridine titration, the concentrated stock solution of base (i.e. pyridine in MeCN, 0.5 M to 50 mM) was used to ensure less than ~1% of total analyte solution volume increase at the end of titration.

4.4.6 Electron Paramagnetic Resonance

EPR experiments were performed in collaboration with the Bennati group[32] to characterize the **DPX** and **FPX** radicals. For these experiments, samples were illuminated for 40 minutes at 254 nm with a 4 W UV lamp under liquid nitrogen and spectra were recorded at 70 K. The hydroxyl groups of **FPX**, **DPX** and **ADPX** were exchanged with deuterium in the CD_3OD. Samples were dissolved in dry acetonitrile and 2-methyl THF to 4.0 mM concentration.

4.5 References

(1) Cozzi, F.; Cinquini, M.; Annuziata, R.; Siegel, J. S. *J. Am. Chem. Soc.* **1993**, *115*, 5330.

(2) Hobza, P. *Phys. Chem. Chem. Phys.* **2008**, *10*, 2581.

(3) Cadman, C. J.; Croft, A. K. *Beilstein J. Org. Chem.* **2011**, *7*, 320.

(4) Hwang, J.; Li, P.; Carrol, W. R.; Smith, M. D.; Pellechia, P. J.; Shimizu, K. D. *J. Am. Chem. Soc.* **2014**, *136*, 14060.

(5) Fieser, L. F. *J. Am. Chem. Soc.* **1930**, *52*, 5204.

(6) Izutsu, K. Acid-base dissociation constants in dipolar aprotic solvents; Blackwell Scientific Publications: Oxford, 1990.

(7) Kaljurand, I.; Kütt, A.; Sooväli, L.; Rodima, T.; Mäemets, V.; Leito, I.; Koppel, I. A. *J. Org. Chem.* **2005**, *70*, 1019.

(8) Chmurzyński, L. *J. Heterocycl. Chem.* **2000**, *37*, 71.

(9) Guin, P. S.; Das, S.; Mandal, P. C. *Int. J. Electrochem.* **2011**, *2011*, 1.

(10) Tessensohn, M. E.; Hirao, H.; Webster, R. D. *J. Phys. Chem. C* **2013**, *117*, 1081–1090.

(11) Richards, J. A.; Whitson, P. E.; Evans, D. H. J. *Electroanal. Chem. Interfacial Electrochem.* **1975**, *63*, 311.

(12) Reece, S. Y.; Nocera, D. G. *J. Am. Chem. Soc.* **2005**, *127*, 9448.

(13) Koo, B. J.; Huynh, M.; Halbach, R. L.; Stubbe, J.; Nocera, D. G. *J. Am. Chem. Soc.* **2015**, *137*, 11860.

(14) Drago, R. S. Physical Methods for Chemists; Surfside Scientific Publishers: Gainesville, FL, 1992.

(15) Lucarini, M.; Mugnaini, V.; Pedulli, G. F.; Guerra, M. *J. Am. Chem. Soc.* **2003**, *125*, 8318.

(16) Kilyanek, S. M.; Fang, X.; Jordan, R. F. *Organometallics* **2009**, *28*, 300.

(17) Soloducho, J.; Olech, K.; Świst, A.; Zajac, D.; Cabaj, J. *J. Chem. Educ.* **2013**, *2013*, 19.

(18) Sato, T.; Torizuka, K. *J. Chem. Soc. Perkin Trans. 2* **1978**, 1199.

(19) Ronlan, A.; Parker, V. D. *J. Chem. Soc. Chem. Commun.* **1974**, 33.

(20) a) Sioda, R. E.; Frankowska, B. *Annales. Uni. M. Curie-Sklodowska*, **2004**, *14*, 154. b) Eberson, L.; Hartshorn, M. P.; Persson, O. *J. Chem. Soc. Perkin Trans. 2* **1995**, 409.

(21) Moore, G. F.; Hambourger, M.; Kodis, G.; Michl, W.; Gust, D.; Moore, T. A.; Moore, A. L. *J. Phys. Chem. B* **2010**, *114*, 14450.

(22) Markle, T. F.; Mayer, J. M. *Angew. Chem. Int. Ed.* **2008**, *47*, 738.

(23) Bonin, J.; Costentin, C.; Robert, M.; Savéant, J.-M. *Org. Biomol. Chem.* **2011**, *9*, 4064.

(24) Pizano, A. A.; Yang, J. L.; Nocera, D. G. *Chem. Sci.* **2012**, *3*, 2457.

(25) Savéant, J.-M. *Elements of Molecular and Biomolecular Electrochemistry*: An Electro-chemical Approach to Electron Transfer Chemistrry; John Wiley: Hoboken, NJ, 2006.

(26) Cukier, R. I.; Nocera, D. G. *Annu. Rev. Phys. Chem.* **1998**, *49*, 337.

(27) Gray, H. B.; Winkler, J. R.; Wiedenfeld, D. *Coord. Chem. Rev.* **2000**, *875*, *200*.

(28) McCleskey, T. M.; Winkler, J. R.; Gray, H. B. *J. Am. Chem. Soc.* **1992**, *114*, 6935.

(29) Marcus, R. A.; Sutin, N. *Biochim. Biophys. Acta - Rev. Bioenerg.* **1985**, *811*, 265.

(30) Costentin, C.; Louault, C.; Robert, M.; Savéant, J.-M. *J. Am. Chem. Soc.* **2008**, *130*, 15817.

(31) Holder, P. G.; Pizano, A. A.; Anderson, B. L.; Stubbe, J.; Nocera, D. G. *J. Am. Chem. Soc.* **2012**, *134*, 1172.

(32) Nick, T. U.; Lee, W.; Koßmann, S.; Neese, F.; Stubbe, J.; Bennati, M. *J. Am. Chem. Soc.* **2015**, *137*, 289.

Table 4.3 Summary of Crystallographic Data for Compound **DPX, DPB** and **DPN**.

	DPX	**DPB**	**DPN**
Formula	$C_{35}H_{38}O_3$	$C_{24}H_{16}O_2$	$C_{22}H_{16}O_2$
Formula weight (g/mol)	506.65	336.37	312.12
Temperature (K)	100(2)	100(2)	100(2)
Crystal System	Orthorhombic	Triclinic	Monoclinic
Space Group	$Pna2_1$	$P\bar{1}$	$P2_1/c$
Color	Colorless	Colorless	Colorless
a (Å)	10.0579(15)	9.221(5)	15.3380(16)
b (Å)	25.425(4)	9.418(5)	10.6291(11)
c (Å)	22.169(4)	20.873(10)	12.0480(12)
α (°)	90	92.569	90.00
β (°)	90	99.044	92.6890(16)
γ (°)	90	116.130	90.00
V (Å ^{3})	5669.0(15)	1593.9(13)	1962.0(3)
Z	8	4	4
No. Reflections	11600	6441	4525
No. Unique Reflections	6587	4175	4041
R_{int}	0.141	0.0529	0.0609
$R1^a$ (all data)	0.1323	0.1918	0.0450
$wR2^b$ (all data)	0.1500	0.4448	0.1104
$R1$ [(I > 2σ)]	0.0607	0.1525	0.0407
$wR2$ [(I > 2σ)]	0.1235	0.4252	0.1061
GOF^c	0.971	1.075	1.042

^{a} $R1 = (\Sigma||F_o| - |F_c||)/\Sigma|F_o|$. ^{b} $wR2 = [\Sigma w(F_o^2 - F_c^2)^2/\Sigma wF_o^2]^{1/2}$. ^{c} GOF $= [\Sigma w(F_o^2 - F_c^2)^2/(n-p)]^{1/2}$ where n is the number of independent reflections and p is the number of refined parameters

Chapter 5 –

Polyprolines Peptide Model for the Long Distance PCET in the RNR β_2 Subunit

Pulse radiolysis experiments were performed at the Brookhaven National Laboratory with Dr. James F. Wishart (wishart@bnl.gov).

5.1 Introduction

Amino acid radicals play an essential role in the biochemistry of metabolism and catalysis.[1] In physiological conditions, the generation of amino acid radicals requires the coupling of a proton and an electron.[2] There are many examples of long distance radical transport in biology; Photosystems II[3], RNR[1], and DNA photolyases[4] are a few renowned examples. To understand the crucial long distance ET (PCET) process, many strategies employing peptides, proteins and other biological molecules have been explored. Gray and co-workers have investigated the long distance ET using metalloproteins labeled with redox-active molecules.[5] Barton and co-workers studied DNA charge transport property.[6] Stubbe, Nocera and co-workers utilized the unnatural amino acids incorporation and photo-oxidant appended RNR to probe 35 Å long PCET radical transport pathways.[1,7,23]

The model study approach assists in an understanding of PCET mechanism of radical transport. The design of PCET model studies should be tightly coupled to biological processes and systems of interest so that the connection of PCET theory to biology can improve. In Chapter 2, small molecules studies for the fundamental understanding of amino acid radical generation mechanism were introduced. Chapter 3 and 4 introduce the design and analysis on the dyad model systems to understand the PCET mechanism of unique structural motif in RNR. In this chapter, the design and analysis of the *synthetic peptide systems* to mimic the long distance radical transport in the β_2 subunit of RNR is presented.

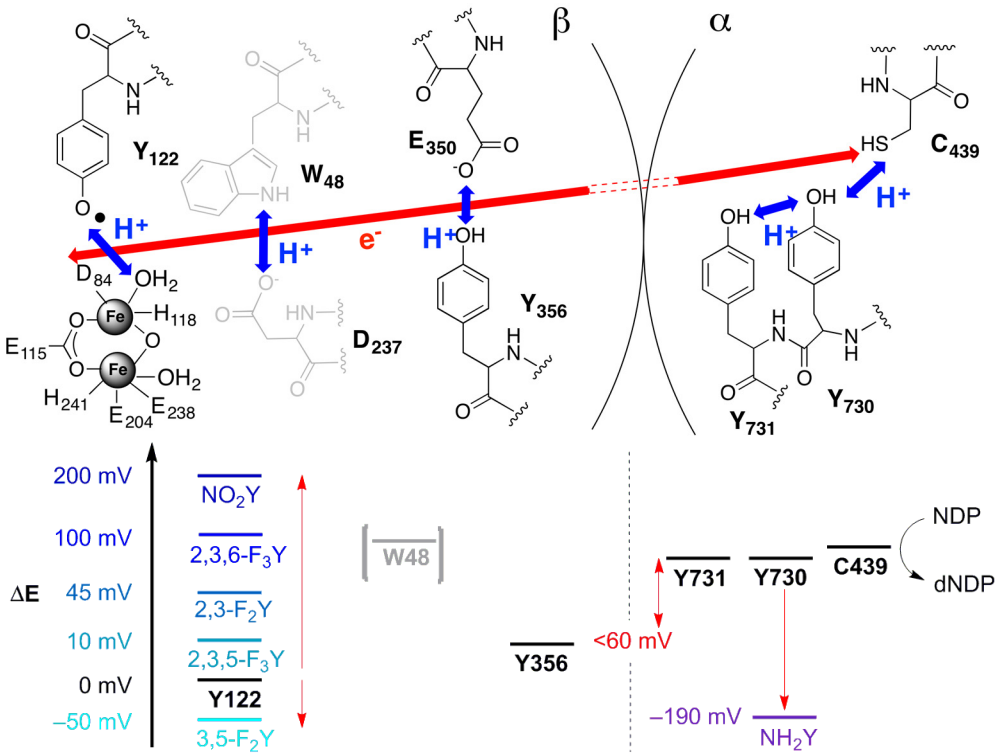

Figure 5.1 (top) Proposed pathway of long-range PCET in *E. coli* Class Ia RNR. Red arrow indicates electron transfer and blue arrows indicate proton transfer.[7] (bottom) The relative reduction potential of unnatural amino acids and on pathway amino acids radicals.[8]

The highlighted amino acids (Y_{122}→(W_{48})→Y_{356}, Figure 5.1) are proposed to compose the PCET pathway of the RNR β_2 subunit. The distances between radical sites in β_2 are too far for unidirectional PCET therefore a bidirectional PCET pathway has been proposed.[1] The proposed pathway is difficult to examine for several reasons. The distance between Y_{122} and W_{48} is long at 7.4 Å and Y_{356} is located on the labile region of the β_2 RNR protein and its position has not been determined crystallographically.[7,9,10] Moreover, point mutation experiments cannot test the involvement of W_{48} in radical pathway because W_{48} is required for the cofactor assembly; mutations block $Y_{122}^{\bullet}$ generation. For these reasons, a model of the pathway is appropriate to begin probing the kinetics of this PCET pathway.

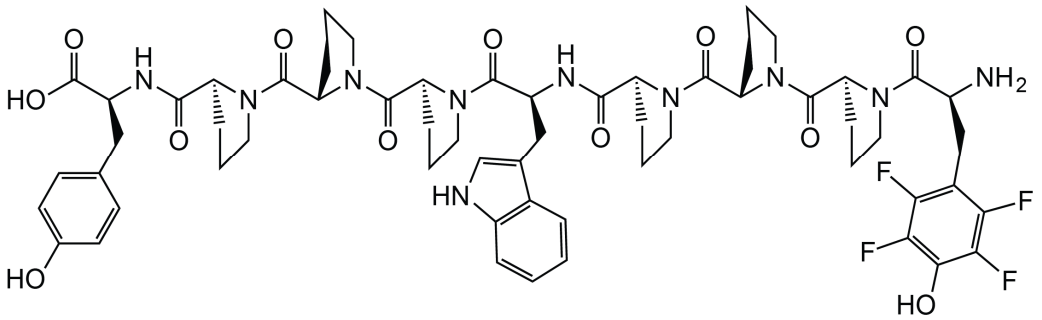

Figure 5.2 The bidirectional PCET radical transport Y_{122}-W_{48}-Y_{356} : polyproline peptide model

The polyproline peptide model shown in Figure 5.2 was designed to emulate the Y_{122}-W_{48}-Y_{356} pathway. The work builds on polyproline models that incorporate redox active amino acids or redox pairs spaced by proline units as implemented by Giese *et al.,*[11–13] Bobrowski *et al.*[14,15] and others.[16] The proline $(Pro)_n$ scaffold restricts the distance of redox active moieties. Intermolecular interaction can be excluded in dilute solutions thus the proline scaffold provides a good platform to study the proposed radical transport pathway in the β_2 subunit of RNR.[17] The polyproline peptide model was designed to hold each amino acid three prolines (~10 Å) apart. With these polyproline peptide models, we aim to (i) answer the effect of W_{48} within a tyrosine radical transport pathway and to (ii) furnish insight on how RNR manages both forward and reverse transport using the same radical pathway.

5.1.1 Polyproline Helix

Poly(proline)s have two different helical conformations, polyproline-I (PPI) and polyproline-II (PPII).[18] The PPI helix is a right-handed and has an axial translation of 1.90 Å composed of 3.3 residues per turn and its peptide bonds are in cis configuration.[19] The PPII helix is a left-handed and has an axial translation of 3.20 Å composed of 3 residues per turn and its peptide bonds are in trans configuration.[20] PPI is the favored conformation in aliphatic alcohols while PPII is favored in water, trifluoroethanol, benzyl alcohol and organic acids.

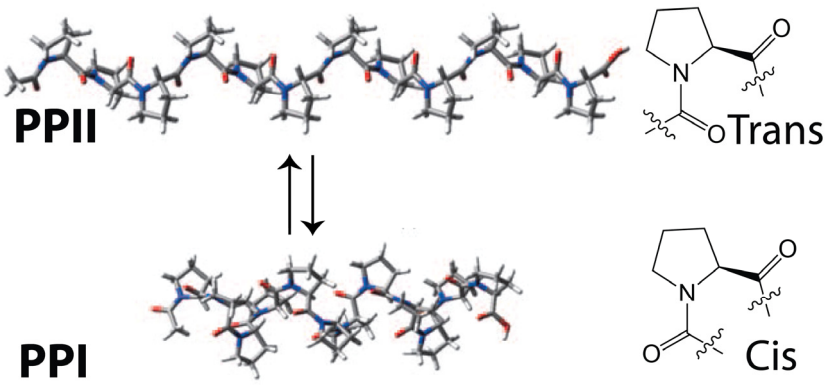

Figure 5.3 The PPI-PPII transition is much slower than the α-helix-coil transition in usual poly(amino acid)s and native proteins. Because the PPI-PPII transition occurs via the cis-trans isomerization of peptides bonds, while the latter is the formation and rupture of hydrogen bonds. Figure is adapted from reference 21.

5.1.2 Method of Radical Generation

In RNR, Y_{122} initiates the forward propagation of radical transport to the active site C_{439}. The reverse radical transport restores the Y_{122} radical. These processes are coupled with protein conformation changes.[22] The absorption features of tryptophan radical cation, tryptophan radical, and tyrosine radicals allow spectroscopic monitoring of their kinetics (Table 5.1).

Table 5.1 The characteristics of tyrosyl and tryptophanyl radicals.[23,24,25.]

Amino Acid	Radical	E^0/E_p	λ_{max}(nm)	ε_{max}($M^{-1}cm^{-1}$)	pK_a
Y	$Y^{\bullet}$	0.94[a]	410	2750 ± 200	9.9
W	$W^{\bullet}$	E_p 1.05[c]	510	1800 ± 50	17
	$WH^{+\bullet}$	1.15[a,b]	580	3000 ± 150	4.3
2,3-F_2Y	2,3-$F_2Y^{\bullet}$	E_p 0.85[c]	412		7.8
F_4Y	$F_4Y^{\bullet}$	E_p 0.97[c]	420		5.6
NO_2Y	$NO_2Y^{\bullet}$	E_p 1.02[c]	425		7.2

[a] E^0 standard reduction potential measured by pulse radiolysis, [b] pH 3, [c] E_p electrochemical peak potential at pH 7.

The Nocera/Stubbe collaboration has exploited these spectra features in the development of photoRNRs using Ru and Re polypyridyl complexes to examine the radical transport chain of

Figure 5.1. The same methods developed for the photoRNRs may be used in the study of the PP model systems of Figure 5.3.

Rhenium-based photo-oxidants, many developed in our group, offer a facile method to photogenerate radicals within the polyproline peptide model. Building on the small molecule PCET studies with [Re]-F_nY and [Re]-Y,[26,27] the kinetics of proton-coupled W oxidation was investigated by way of both bimolecular and unimolecular photo-oxidation with [$Re(CO)_3$(bpy-F)CN] ([Re]) and [Re]-W, respectively. The low yield for $W^{\bullet}$ generation and fast charge recombination between photooxidants and $F_nY^{\bullet}$s presents a potential roadblock that inhibits measurable production of radicals throughout sequential triad amino acid via hoping kinetics. To circumvent this potential roadblock, we explored the use of pulse radiolysis methods to generate the radical. These studies were carried out at the Brookhaven National Laboratory. We focused on the generation of W radical by $Y^{\bullet}$ analogs $F_4Y^{\bullet}$ and $NO_2Y^{\bullet}$ (used to vary the driving force of radical transport) to explore the contention that W_{48} serves as PCET stepping-stone between two distant tyrosines (Y_{356} and Y_{122}).

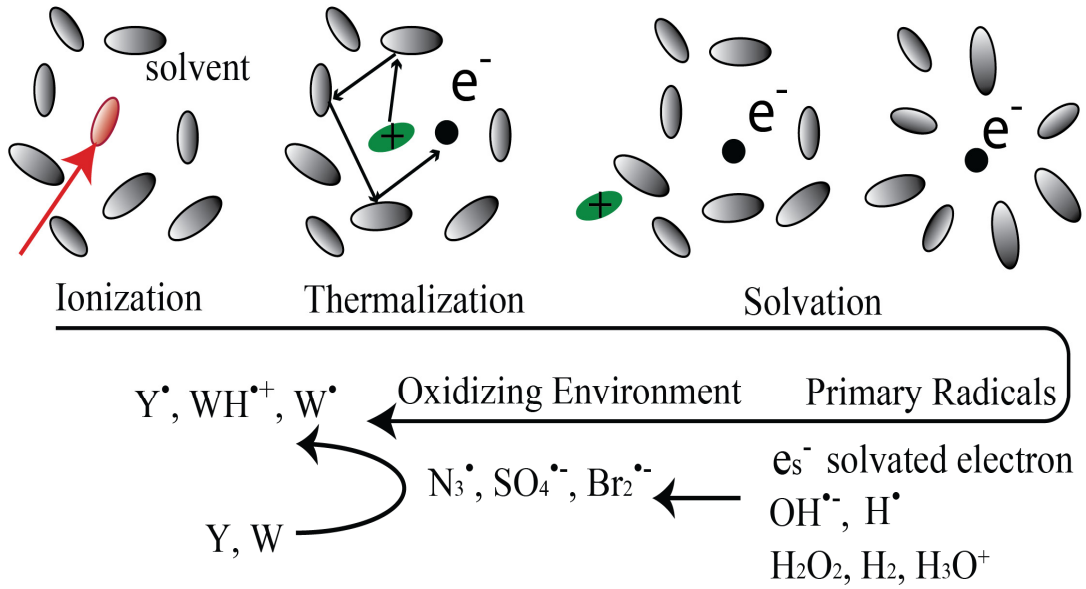

Figure 5.4 Basic concept of pulse radiolysis in water.

The general pulse radiolytic scheme used in this study is summarized in Figure 5.4. In pulse radiolysis, fast and highly energetic electrons ionize the condensed media (water) to form approximately equal yields of reducing (e_s^-, solvated electron and H$^\bullet$, hydrogen atom) and oxidizing ($^\bullet$OH: hydroxide radical) radicals.[28] All of these processes occur in femtosecond to picosecond time scale after the radiation.

To obtain totally oxidizing conditions, all the primary radicals can be converted into a single kind of secondary radical.[*29] In the saturated aqueous solution of NaN_3, the azide radicals are produced by $^\bullet$OH radicals. The azide radical ($^\bullet N_3$) has the standard reduction potential (E^0 = 1.33 V vs. NHE) that is potent enough to oxidize tryptophan and tyrosine. Some commonly used inorganic secondary radicals for generating amino acid radicals are $Br_2^{\bullet-}$ (E^0 = 1.66 V vs. NHE), $I_2^{\bullet-}$ (E^0 = 1.05 V vs. NHE), $(SCN)_2^{\bullet-}$ (E^0 = 1.33 V vs. NHE), $CO_3^{\bullet-}$ (E^0= 1.5 V vs. NHE), and $SO_4^{\bullet-}$ (E^0 =2.43 V vs. NHE) .

Scheme 5.1 illustrates the relevant kinetics of polypeptide model radical transport by pulse radiolysis. The secondary radicals (azide/sulfate) are very potent oxidants so they can react with tryptophan, tyrosine and unnatural tyrosines.[30] Generated amino acid radicals are then able to undergo subsequent radical transport and a follow-up chemistry (2nd order decomposition).

---

[*] There are three ways to achieve either totally reducing or oxidizing conditions: i) by interconversion of the primary radicals into a single kind; ii) by converting all the primary radicals into a single kind of secondary radical; or iii) by removing the unwanted primary radical by reaction to form a relatively inert secondary radical.

Scheme 5.1 Kinetics analysis of polyproline peptide model radical transport in W-P_3-Y. In W-P_3-F_4Y, the radical transport occurs from tyrosyl radical to tryptophanyl radical (the direction of k_3 is reversed).

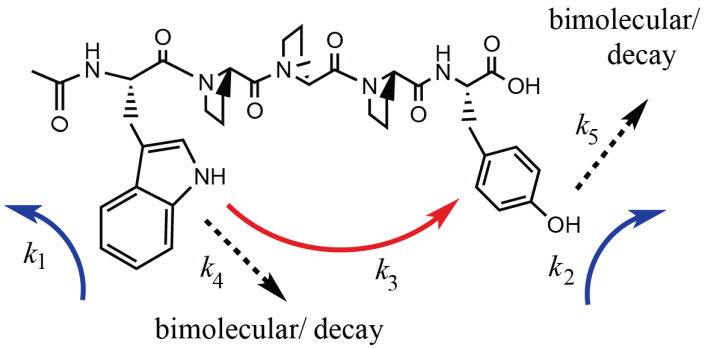

The measurement of the radical transport rate constant k_3 (= k_{ET}), depicted by the red arrow (Scheme 5.1), is the goal of the measurement. For k_3 to be measured, a few criteria must be met. Firstly, the initial amino acid radical generation by the secondary radicals needs to be faster than the radical transport rate. The relevant rate constants of amino acid oxidation by the secondary radicals ($^{\bullet}N_3$ and $SO_4^{\bullet-}$) are in the range of 10^8–10^9 s^{-1}, much faster than the expected radical transport rates (10^3–10^5 s^{-1}) (Table 5.2). The rate constants of F_4Y, 2,3-F_2Y and NO_2Y with the secondary radicals (azide/sulfate) are best measured at the LEAF (Laser-Electron Accelerator Facility) picosecond time scale pulse radiolysis system at Brookhaven National Laboratory. Secondly, the 2nd order decay of tryptophan (k_4) and tyrosyl radical (k_5) should be much slower than the radical transport rate. Otherwise, the observable quantity of radicals cannot build up. Lastly, each radical should provide a distinct spectroscopic handle to de-convolute complex kinetics. The absorbance change at 410 nm for tyrosyl radical can contain contributions of i) the decay of initial tyrosyl radical species and ii) new tyrosyl radical generation by radical transport from tryptophan radicals. Similarly, the absorbance change at 510 nm for tryptophanyl radical will contain contributions of i) the decay of initial trytophanyl radical species and ii) the decay resulted from oxidizing tyrosines via radical transport. Based on this primary assessment, the pulse

radiolysis offered a promising option for the radical transport measurements in the PP model systems. Accordingly, these studies were pursued at Brookhaven National Laboratory.

Table 5.2 The rate constants of amino acids with various secondary radical species in aqueous solutions.[30]

Azide Radical [$^{\bullet}N_3/N_3^- = 1.33$ V (vs. NHE)]		k (M^{-1} s^{-1})	
Tryptophan	$^{\bullet}N_3 + TrpH \rightarrow N_3^- + Trp^{\bullet} + H^+$	4.4×10^9	pH 12
		4.1×10^9	pH 7.4
		4×10^9	pH 6.1
Tyrosine	$^{\bullet}N_3 + TyrOH \rightarrow N_3^- + TyrO^{\bullet} + H^+$	3.6×10^9	pH 11.8
		3.1×10^9	pH 7
		1.0×10^8	pH 6.5
Sulfate radical [$SO_4^{\bullet -}/SO_4^{2-} = 2.43$ V (vs. NHE)]		k (M^{-1} s^{-1})	
Tryptophan	$SO_4^{\bullet -} + TrpH \rightarrow SO_4^{2-} + Trp^{\bullet} + H^+$	2.0×10^9	pH 7
Tyrosine	$SO_4^{\bullet -} + TyrOH \rightarrow SO_4^{2-} + TyrO^{\bullet} + H^+$	3.0×10^9	pH 6.8
		3.2×10^9	pH 7

5.2 Results

5.2.1 Synthesis and Purification

The syntheses of polyproline models were achieved by following a well-established solid phase peptide synthesis (SPPS) method using Fmoc-protected amino acids.[31] Details of the synthesis are provided in the Experimental section of this chapter. It was difficult to obtain crystals of the short peptides (5 – 9 mers) for x-ray crystallography so we compared the CD spectra of polyproline models for primary structure characterization. Fmoc coupling of proline was very inefficient and yielded many by-products. Thus, an extensive HPLC purification was needed to obtain pure peptides.

5.2.2 Circular Dichroism Spectroscopy

The circular dichroism (CD) spectra of the short peptide models showed the characteristics of a PPII helix. A strong negative band at 202 – 206 nm and a weak positive band at 225 – 229 nm (Figure 5.5) has been taken as a measure of PP helicity.[17] The stability of PPII structure was confirmed using CD across a range of pH and solvent compositions that were to be employed for kinetics measurements (0, 25, 50, 75, 100 % MeCN with aqueous buffer, in RT) (Figure 5.5–5.6).

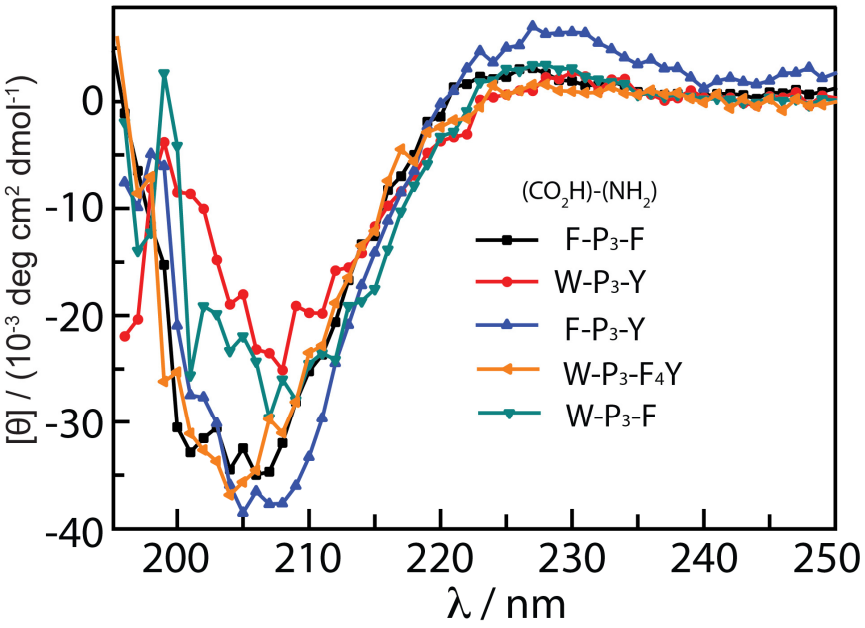

Figure 5.5 Circular dichroism spectra of polyproline peptide models for bidirectional PCET. The CD spectra were measured in a 1:3 acetonitrile:aqueous buffer mixture at room temperature.

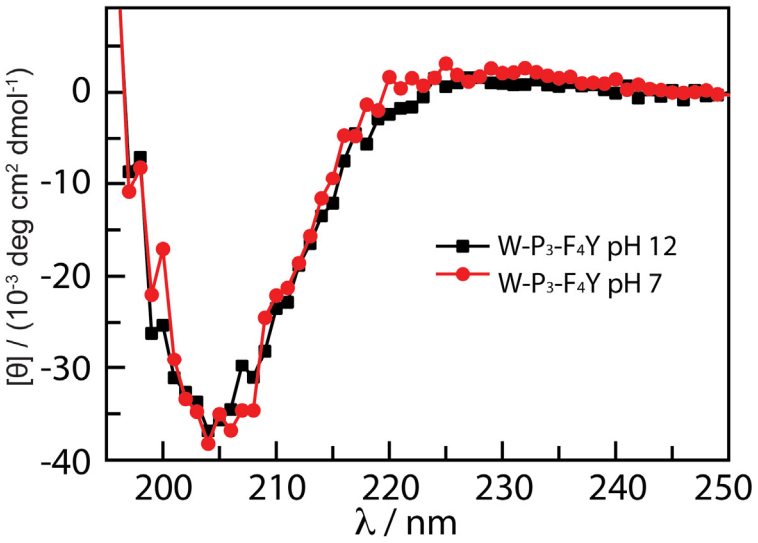

Figure 5.6 Circular dichroism spectra of **W-P$_3$-F$_4$Y** in a 1:3 acetonitrile:aqueous buffer mixture in room temperature. The peptide **W-P$_3$-F$_4$Y** sample was 30 μM in 50 mM phosphate buffer pH 12 (black) and pH 7 (red).

5.2.3 Rate Constant Measurements of Amino Acids Radical Generation

Azide and sulfate radicals were used as the secondary radical species to initiate and generate radicals in the polyproline peptide models. The rate constant of tryptophan oxidation by azide ($k_1 \sim 4.1 \times 10^9\ M^{-1}\ s^{-1}$) is slightly faster than that of tyrosine ($k_2 \sim 3.1 \times 10^9\ M^{-1}\ s^{-1}$) at pH 7.[32] The rate constants of 2,3-F$_2$Y and 2,3,5,6-F$_4$Y with azide radical were measured to be k_r (F$_2$Y) = $3.08 \pm 0.13 \times 10^9\ M^{-1}\ s^{-1}$ and k_r (F$_4$Y) = $3.20 \pm 0.02 \times 10^9\ M^{-1}\ s^{-1}$, accordingly.

Attempts to measure a rate constant for NO$_2$Y$^\bullet$ (all nitrotyrosines refer to 3-nitrotyrosine in this chapter) generation by azide and sulfate radicals failed. The reduction potential of NO$_2$Y is 200 mV higher than that of Y and the λ_{max} = 430 nm of NO$_2$Y$^\bullet$ is shifted from λ_{max} = 410 nm of Y$^\bullet$, by 20 nm. Since both azide and sulfate radicals are strong enough oxidants, the failure to observe NO$_2$Y$^\bullet$ is attributed to the spectral overlap between starting $^-$ tyrosinate NO$_2$Y species and the desired radical,NO$_2$Y$^\bullet$.[33]

The 2nd order decay rate of monomer amino acid radicals were obtained by fitting the single wavelength transient absorption traces to the following equations,

(Eq. 5.1) $$-\frac{d[A]}{dt} = k_d[A]^2$$

(Eq. 5.2) $$\frac{1}{[A]} = \frac{1}{[A]_0} + k_d t$$

where [A] is the concentration of the radical and $[A]_0$ is the initial concentration. The k_d of F_4Y radical (F_4Y-OMe, OMe refers to a methyl ester) and the k_d of tryptophanyl radical (W-OMe) were measured to be $4.94 \times 10^4\ M^{-1}\ s^{-1}$ and $7.64 \times 10^4\ M^{-1}\ s^{-1}$, accordingly. Tryptophan attains a maximum absorption amplitude faster than tyrosines (F_4Y, Y, F_2Y) due to its higher reactivity (Figure 5.7).

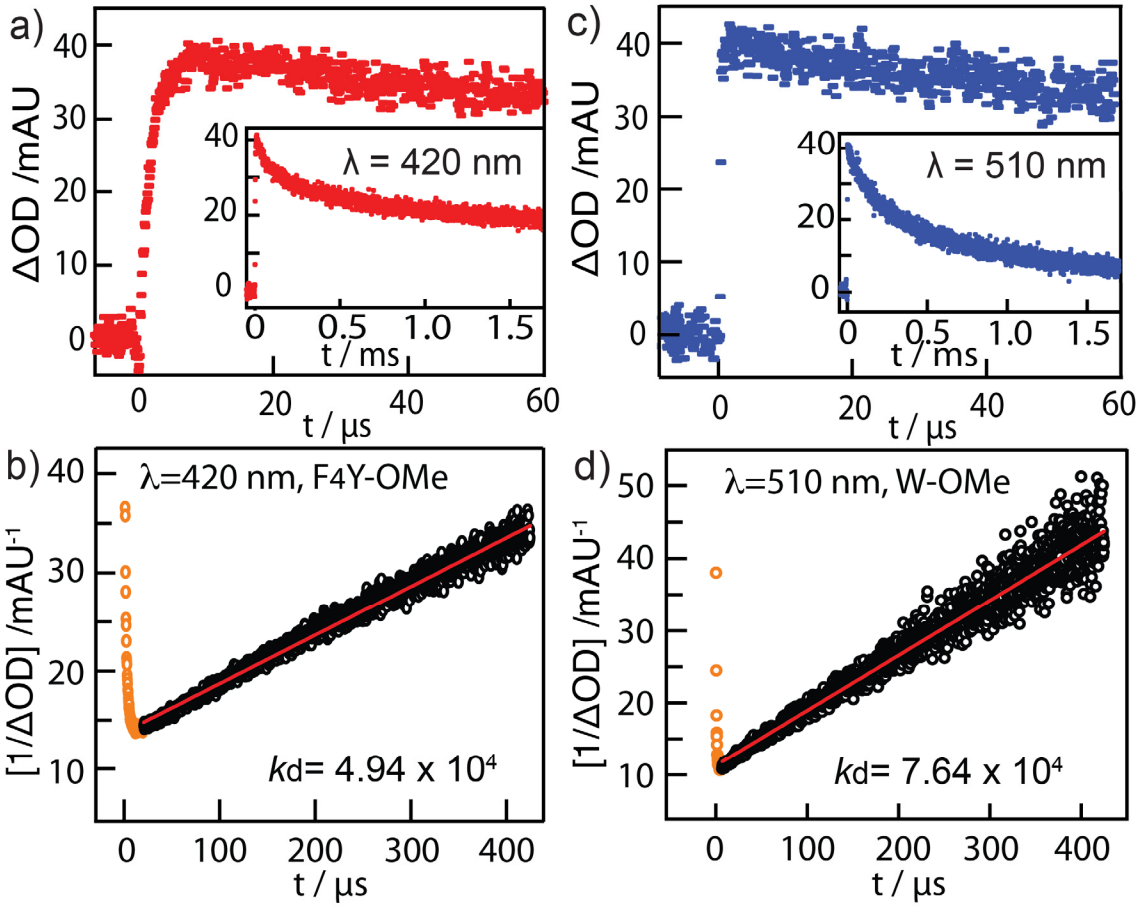

Figure 5.7 The 2nd order decay rate constants; the sample was dissolved 0.2 mM concentration in 50 mM pH 7 phosphate buffer 0.1 M NaN_3 solution. a) The TA of tyrosyl radical decay in F_4Y-OMe, monitored at 420 nm in room temperature. b) The inverse plot of (a) and the 2nd order decay fitting (red line). c) The TA of tryptophanyl radical decay in W-OMe, monitored at 510 nm in room temperature. d) The inverse plot of (c) and the 2nd order decay fitting (red line).

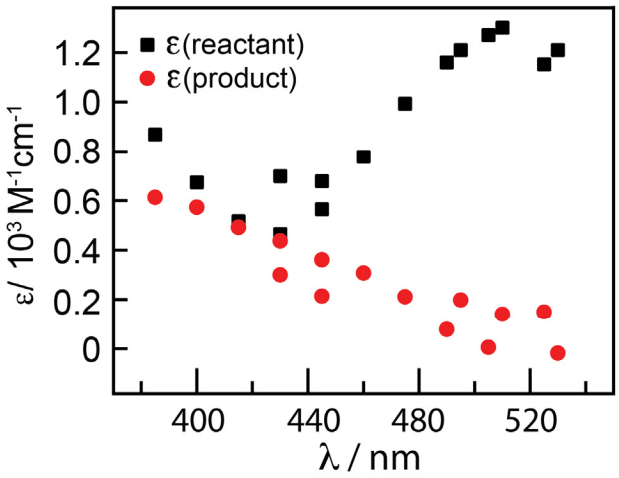

Figure 5.8 The molar absorptivity of the reactant radicals (W-OMe) at 5 μs (black squares) and 1.5 ms (red squares) after radiolytic excitation at room temperature. W-OMe was at 0.2 mM concentration in 50 mM pH 7 phosphate buffer 0.1 M NaN_3 solution.

The TA spectra of W-OMe were taken at 5 μs (black squares) and at 1.5 ms (red squares) after radiolytic excitation (Figure 5.8). The early time spectrum showed the absorption feature of W$^{\bullet}$ radical at λ_{max} = 510 nm. At 1.5 ms after the radiation, a significant absorption feature remained at λ = 410–420 nm, while the W$^{\bullet}$ absorption amplitude decreased. The absorption signal after 1.5 ms is attributed to the W$^{\bullet}$ dimeric decomposition products and no further identification was attempted.

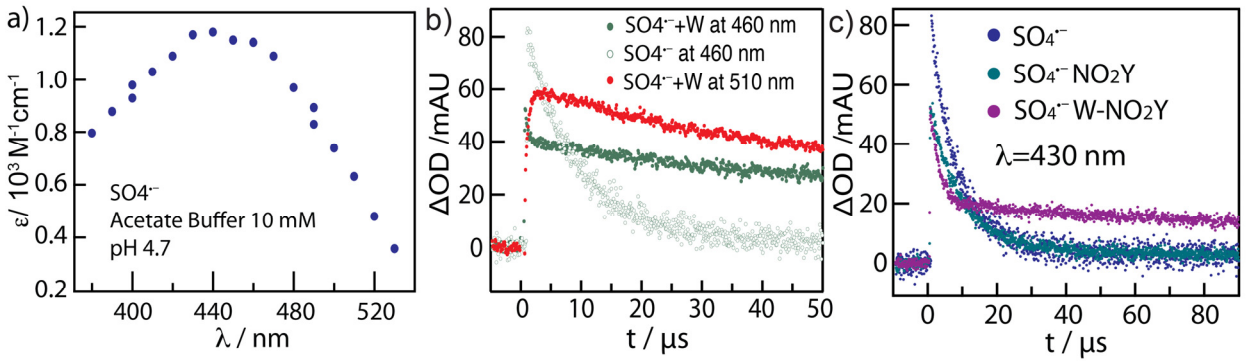

Figure 5.9 a) The sulfate radical (λ_{max} = 460 nm) molar absorptivity characterization, measured in 10 mM pH 4.7 acetate buffer, 5 μs after the radiation. b) Sulfate radical (λ_{max} = 460 nm) decays away within 30 μs with no substrate (green open circle, λ_{det} = 460 nm). With W-OMe, the sulfate radical decays within 5 μs (green solid circle, λ_{det} = 460 nm) as tryptophanyl radical grows (red solid circle, λ_{det} = 510 nm) concurrently, measured in 0.2 mM analyte concentration in 50 mM pH 7 phosphate buffer 2 mM $NaSO_4$ solution. c) Single wavelength kinetics trace monitored at 430 nm with: sulfate radical only (blue), NO_2Y (green), AcW-NO_2Y (violet). The samples were dissolved to the concentration of 50 μM in 0.1 mM $NaSO_4$, 50 mM pH 7 phosphate buffer solution.

The sulfate radical has an absorption feature at λ_{max} = 460 nm, (Figure 5.9a) that decays within 30 μs after excitation (green open circle, Figure 5.9b). In the presence of W-OMe, the sulfate radical decays within 5 μs (green solid circle, Figure 5.9b) as tryptophanyl radical grows (red solid circle, 510 nm) concurrently. This measurement confirms that the single wavelength kinetics of tyrosyl and tryptophanyl radicals does not have a contribution from "unreacted" sulfate radical, as sulfate radicals are quickly consumed in generating amino acid radicals.

As described earlier, the spectral overlap with NO_2Y^- may result in the failure to detect $NO_2Y^\bullet$. However, the generation of $NO_2Y^\bullet$ should be manifested in the generation of $W^\bullet$ by electron transfer within the in $AcNO_2Y$-W dimer since the apparent reduction potential E^0 of $NO_2Y^\bullet$ is 100 mV higher than the E^0 ($W^\bullet$/W) at pH 7. However, the tryptophan radical growth of AcW-NO_2Y monitored at 510 nm did not show any difference from W-OMe case, indicating no generation of $NO_2Y^\bullet$. Therefore, the kinetic analysis of polyproline models with NO_2Y was not pursued further.

5.2.4 The Radical Transport Rate Constant

As a reference for the polyproline peptide model measurements, the amino acids dimer AcWY was analyzed by pulse radiolysis. W-Y dyad has been studied in laser flash photolysis[25] and pulse radiolysis.[14,15] First, the burst phase (referring to the fast initial generation of amino acid radical by the secondary radical) kinetics of each amino acid radical was measured (Figure 5.10). After the first 10 μs, the tyrosyl radical (410 nm, green circle) in AcWY samples continues to grow and the tryptophan radical (510 nm, black circle) decays concurrently. The growth and decay kinetics are faster than observed for the monomer cases (Figure 5.9).

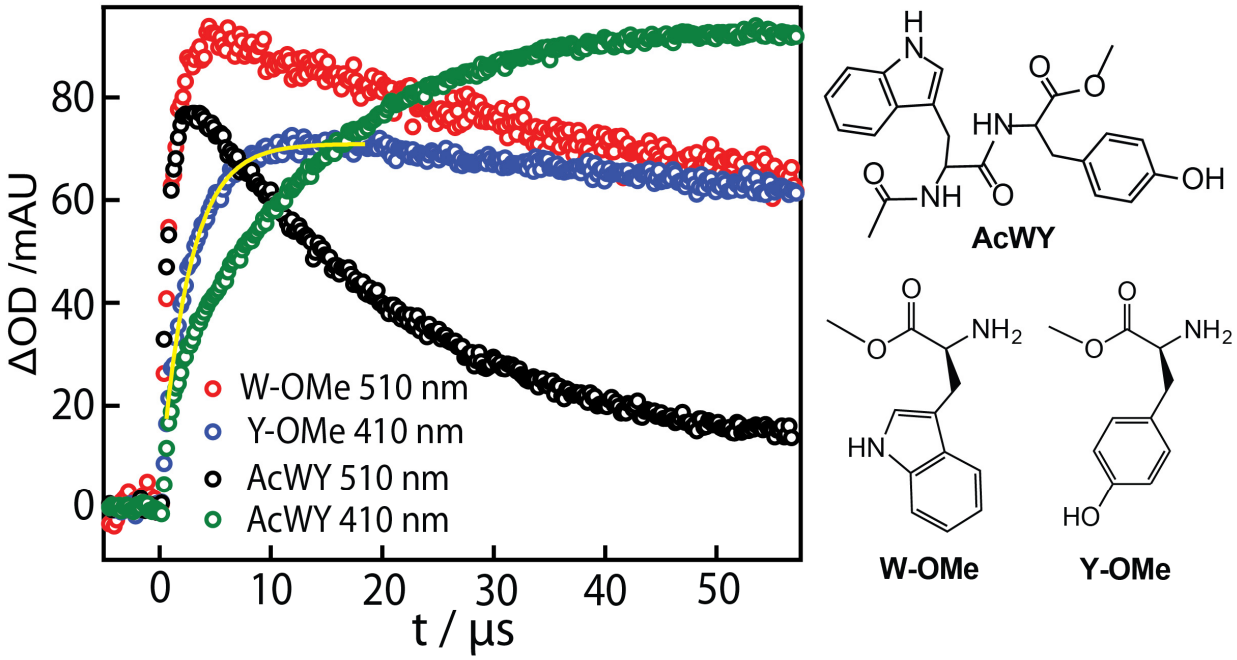

Figure 5.10 AcWY radical transport rate measurement: Samples for AcWY, W-OMe, and Y-OMe were dissolved to the concentration of 50 μM in 50 mM pH 7 phosphate buffer solution. The monomer Y-OMe (blue dot, traced at 410 nm) and W-OMe (red dot, 510 nm) achieved the absorption amplitude maximum within 10 μs. The tyrosyl radical trace (green dot, 410 nm) in AcWY has an initial burst growth phase till 10 μs, which overlaps with slower mono-exponential growth that reaches the maximum around 50 μs. The tryptophanyl radical trace (black dot, 510 nm) shows the same initial growth phase however decays much faster than the monomer tryptophan due to the radical transport. The tyrosyl and tryptophanyl radical reached equilibrium by 50 μs then both radicals decay away slowly in the ms time scale.

The single wavelength kinetics traces in the time range of 10 μs to 50 μs reflect mostly the radical transport between W and Y with the AcWY dimer. The 2nd order decay kinetics constants are much slower compared to the rate of intermolecular electron transfer (radical transport, Figure 5.7 and Figure 5.10). Each trace was fit with to a mono-exponential decay to yield $k_{ET}^{410\ nm} = 0.74 \times 10^4\ s^{-1}$ and $k_{ET}^{510\ nm} = 6.5 \times 10^4\ s^{-1}$. The electron transfer rate of tryptophan radical is faster than that of tyrosyl radical due to the 2nd order decay rate contribution. The rates are comparable to the laser flash photolysis results: $k_{ET}^{410\ nm} = 1.8 \times 10^4\ s^{-1}$ and $k_{ET}^{510\ nm} = 8.6 \times 10^4\ s^{-1}$.[25]

Note that the absorbance at 510 nm did not return to the baseline due to the finite equilibrium position of the reaction, W•-Y →W-Y•.

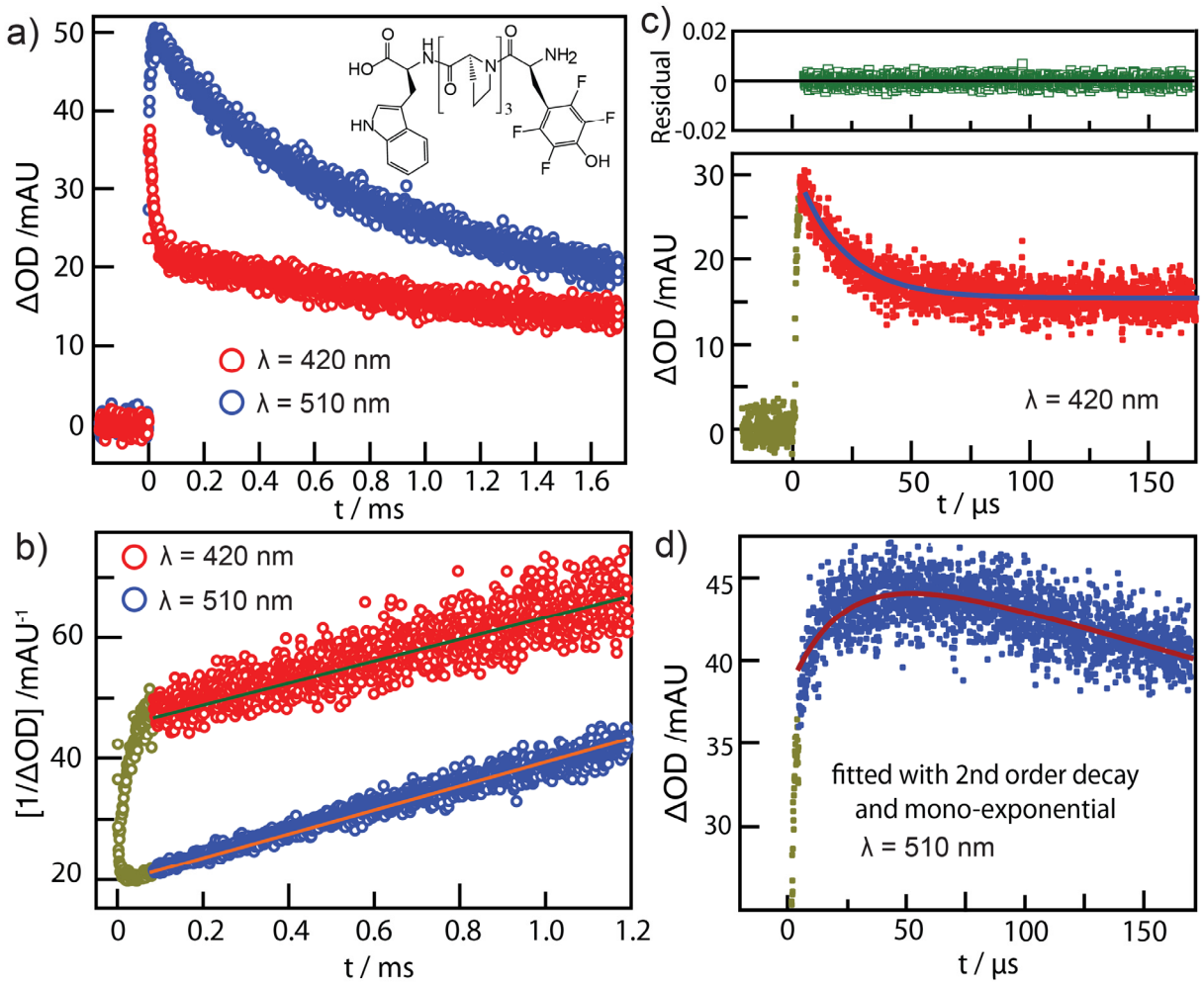

Figure 5.11 W-P$_3$-F$_4$Y radical transport rate measurement: sample was dissolved to 0.1 mM concentration in 50 mM phosphate buffer NaN_3 0.1 M pH 12 50 mM phosphate buffer solution at room temperature. a) Long time scale absorption traces of W-P$_3$-F$_4$Y polyproline model after radiolysis. Tryptophan radical signal was traced at λ_{max} of tryptophan (510 nm, blue circles) and tyrosyl radical was traced at λ_{max} of F$_4$Y (420 nm, red circles). b) Inverse plot of (a): The inverse traces at 420 nm and at 510 nm were linear thus show the second order dependence of the decay. These decay processes are much slower than the target ET process. c) The monoexponential fitting of F$_4$Y radical decay (red) and the residual of the fitting. d) The trace was fitted with 2nd order decay and exponential decay using the (PRWIN program).[34]

The AcWY kinetics aided in the analysis of the polyproline peptide models. The longer radical transport distance in the PP model inevitably slows down the intermolecular ET rate con-

stant compared to the dimeric AcWY. The single wavelength traces were obtained in the long (~ 1.7 ms) and the short (170 μs) time scales (Figure 5.12 and 5.13, pH 12 and pH 7, accordingly). The initial burst phase (0 –10 μs) is dominated by amino acid radical generation by the secondary radicals (Figure 5.12a). Follow-up time range (10 – 150 μs) was used to obtain k_{ET}. Lastly, the long time scale (1.7 ms) was used to obtain the 2nd order decay rate constants. The results are summarized in the Table 5.3 and the detailed calculation of k_{ET} is provided in the discussion.

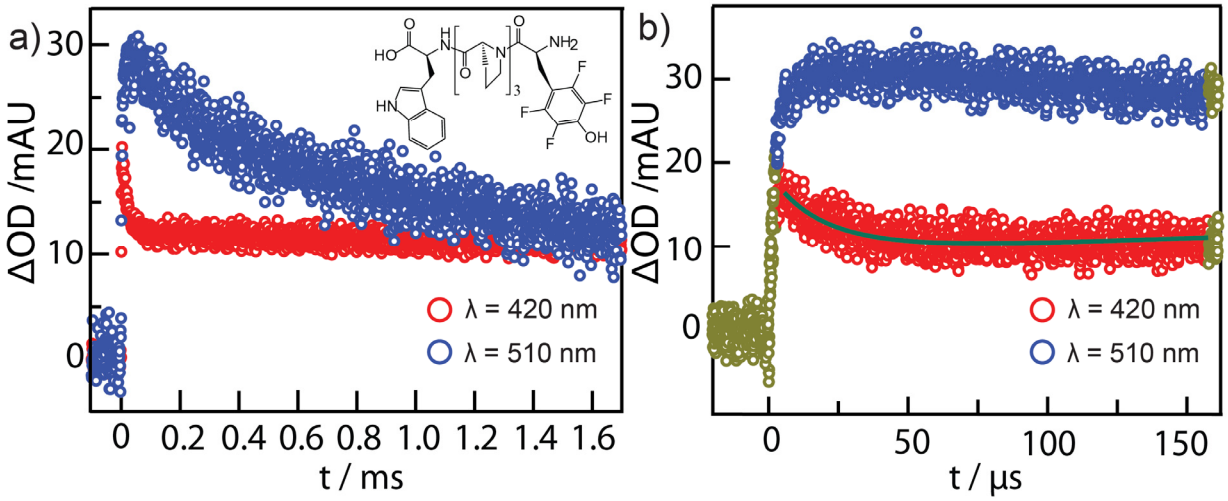

Figure 5.12 W-P$_3$-F$_4$Y radical transport rate measurement: sample was dissolved to 0.1 mM concentration in 50 mM phosphate buffer NaN_3 0.1 M pH 7 50 mM phosphate buffer solution at room temperature. a) The long time scale absorption traces of W-P$_3$-F$_4$Y polyproline model after radiolysis. The intramolecular radical transport occurs in the initial 10 ~200 μs after the pulse radiolysis. b) The short time scale single wavelength traces of W-P$_3$-F$_4$Y. Tryptophan radical signal was traced at λ_{max} of tryptophan (510 nm, blue circles) and tyrosyl radical was traced at λ_{max} of F$_4$Y (420 nm, red circles).

Table 5.3 Summary of k_{ET} of polyproline model systems and AcWY (unit: s^{-1})

Sample	pH 12	pH 7
W-P$_3$-F$_4$Y	$4.89 \pm 0.54 \times 10^4$	$4.74 \pm 0.44 \times 10^4$
Y-P$_3$-W[a]	$4.8 \pm 0.13 \times 10^4$	$2.0 \pm 0.13 \times 10^3$
AcWY	-	$7.4 \pm 0.04 \times 10^3$
AcWY[b]	1.2×10^{5}[c]	1.8×10^4

Azide radicals were used for all pulse radiolysis data presented in this table. [a] reported in ref. 14, 15. [b]Laser flash photolysis, ref 25.[c] reversed Y→W transport

5.3 Discussion

The radical generation rate constants for monomeric amino acid 2,3-F_2Y (3.08×10^9 M^{-1} s^{-1}) and 2,3,4,5-F_4Y (3.20×10^9 M^{-1} s^{-1}) by azide radical were nearly the same as the rate constant of tyrosine generation (3.1×10^9 M^{-1} s^{-1}). The similar reactivity toward the secondary radicals implies similar reorganization energies among tyrosine analogues. The fast radical generation of both W and Ys by the secondary radical dominates the early time points (burst phase, 0 – 10 μs, Figure 5.10). Excluding the early time points (0 –10 μs) simplifies the rate equation of each amino acid radical population as following:

(Eq. 5.3) $$\frac{d[W\cdot]}{dt} = -k_{d,W}[W\cdot]^2 + k_{ETf}[F_4Y\cdot] - k_{ETb}[W\cdot]$$ W radical

(Eq. 5.4) $$\frac{d[F4Y\cdot]}{dt} = -k_{d,F4Y}[F_4Y\cdot]^2 - k_{ETf}[F_4Y\cdot] + k_{ETb}[W\cdot]$$ F_4Y radical

where k_{ETf} denotes the forward ET rate constant (W-P_3-F_4Y$^\bullet$→W$^\bullet$-P_3-F_4Y) and k_{ETb} denotes the reverse ET (W-P_3-F_4Y$^\bullet$←W$^\bullet$-P_3-F_4Y) rate constant. Both 1st order ET transport and 2nd order decay are accounted for in the rate equation Eq. 5.3 and 5.4. The dilute solutions of polyproline peptide models discouraged intermolecular ET: the k_{ET} (4.89×10^4 s^{-1}, pH 12) and the k_d^{F4Y} (4.94×10^4 M^{-1} s^{-1}) did not change in the varying concentration range of 0.1 mM – 2 mM. Thus, the intermolecular ET reaction was excluded from the kinetics analysis.

The radical transport rates between amino acids determine the dynamic equilibrium coefficient, K_{eq}, which can be expressed in terms of the driving force (ΔG).[14]

(Eq. 5.5) $$K_{eq} = \frac{k_{ETb}}{k_{ETf}} = e^{-\Delta G/RT}$$

(Eq. 5.6) $$\Delta G = -nF\Delta E$$

(Eq. 5.7) $$\Delta E = E_p\,(F_4Y^\bullet/F_4Y) - E_p\,(W^\bullet/W)$$

where R is the universal gas constant (8.314 J K^{-1} mol^{-1}), F is the Faraday constant (9.648×10^4 C mol^{-1}), and n is the molar number of charges. The ΔEs were calculated to be ~60 mV (pH 7) and ~360 mV (pH 12) from the Pourbaix diagram (Figure 5.13). With the RT/nF value of 25.693 mV (n=1, T=25 °C), K_{eq} at each pH is as follows;

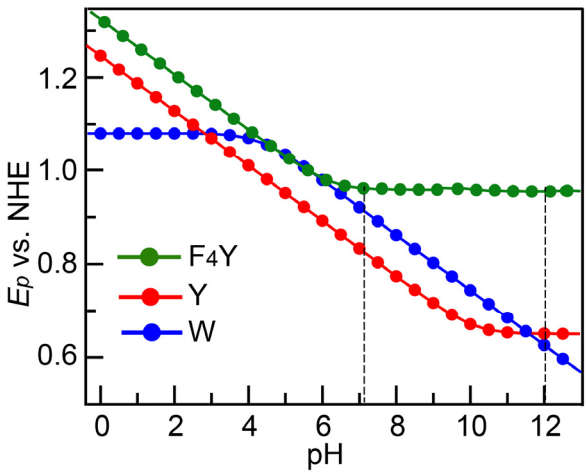

Figure 5.13 The Pourbaix diagram of F_4Y, Y and W.[8,23] W: pK_a~17, F_4Y: pK_a ~5.6 and Y: pK_a ~10.

$$K_{eq} = e^{(60\ mV/\ 25.693\ mV)} = 10.33,\ pH\ 7$$

$$K_{eq} = e^{(360\ mV/\ 25.693\ mV)} = 1.22 \times 10^6,\ pH\ 12$$

The equilibrium constants imply that the forward ET reaction rate (k_{ETf}) in the polyproline model W-P_3-F_4Y is much faster than the backward ET rate (k_{ETb}) at both pHs. The concentrations of radicals, [$F_4Y^{\bullet}$] and [$W^{\bullet}$], are much lower than the dilute solution concentration (0.1 mM), thus the bimolecular decay contribution is fairly small during the time period of 10–150 μs after the radiation. From the assessed equilibrium constants and small 2nd order decay contribution within the time range of interest, the kinetic law (Eq. 5.3 and Eq. 5.4) can be further simplified as following;

$$\text{(Eq. 5.8)} \qquad \frac{d[W\cdot]}{dt} = +k_{ET}[F_4Y\cdot] \quad \text{W radical}$$

$$\text{(Eq. 5.9)} \quad \frac{d[F4Y\cdot]}{dt} = -k_{ET}[F_4Y\cdot] \qquad F_4Y \text{ radical,}$$

for the kinetics for the time range of 10–150 μs.

The simplified rate law was also used for the reported analogous system ($W^{\bullet}$-P_3-Y → W-P_3-$Y^{\bullet}$). The calculated rates of radical transport in $F_4Y^{\bullet}$-P_3-W → F_4Y-P_3-$W^{\bullet}$ are 4.89×10^4 s^{-1} at pH 12 and 4.74×10^4 s^{-1} at pH 7. These rates are comparable to the rate observed in the analogous $W^{\bullet}$-P_3-Y → W-P_3-$Y^{\bullet}$ system. With 300 mV larger apparent potential difference at pH 12 to

pH 7, the k_{ET} increase of only ~ 3% from pH 7 to pH 12 suggests that an ETPT pathway is operative for radical transport. The F_4Y radical generation is a pure ET process throughout the measurements because F_4Y exists as deprotonated tyrosinate F_4Y^-(pK_a^{F4Y} ~ 5.6). Thus, the observed ETPT pathway is indicative of the radical generation pathway of W in the polyproline model system.

In RNR, conformational gating will assist redox potential "tuning" of the radical transport pathway. Thus, the transport of radical (Y_{122}→(W_{48})→Y_{356}) occurs forward and backward by utilizing the same pathway. Therefore, the ability of W to communicate with Y at ~ 10 Å shown by this work is important in evaluating W48 involvement in the radical transport pathway.

5.4 Conclusion

The polyproline peptide models were designed to mimic the bidirectional PCET radical pathway (Y_{122}→W_{48}→Y_{356}) in the β_2 subunit. The kinetic constants for 2,3-$F_2Y^\bullet$ and 2,3,4,5-$F_4Y^\bullet$ generation by azide radical were measured and the subsequent oxidation of W was explored by pulse radiolysis. The rate constants of radical transport in ($F_4Y^\bullet$-P_3-W → F_4Y-P_3-W$^\bullet$) was measured to be 4.89×10^4 s^{-1} (pH 12) and 4.74×10^4 s^{-1} (pH 7), comparable to the rate constants observed in the analogous system (W$^\bullet$-P_3-Y → W-P_3-Y$^\bullet$: 4.8×10^4 s^{-1} and 2.0×10^3 s^{-1} pH 12 and 7, accordingly) for the reverse process. With the caveat that drastic differences between bulk water and the protein environment exist, the results from these model studies show that the β-W_{48} in RNR may be competent for mediating reversible radical translocation between β-$Y_{122}^\bullet$ and β-Y_{356}. Relative to TA spectroscopy, pulse radiolysis afforded us with larger radical yields to

observe this transport. These data provide a way to reasonably approximate the total radical transport rate across the triad system, F_4Y-P_3-W-P_3-Y; analogous to Y_{122}→W_{48}→Y_{356} in RNR.

5.5 Experimental Details

5.5.1 Synthesis and Materials

Materials. Piperidine, diisopropylethylamine (DIPEA), triisopropylsilyl ether (TIPS), hydrochloric acid (HCl), sodium carbonate (Na_2CO_3) and ethyl acetate (EtOAc) were purchased from Fluka. L-Tryptophan-*tert*-butyl ester (W-OtBu), L-tryptophan-methyl ester hydrochloride (W-OMe•HCl), *N*-acetyl-L-tryptophan (Ac-W), *N*-acetyl-L-tryptophan-methyl ester (Ac-W-OMe), O-(1H-6-chlorobenzotriazole-1-yl)-1,1,3,3-tetramethyluronium hexafluorophosphate (HCTU), 4-benzoyl-N-[(9H-fluoren-9-ylmethoxy)carbonyl](Fmoc)-L-trytophan (Fmoc-Trp), Fmoc-L-phenylalanine (Fmoc-Phe), Fmoc-L-proline (Fmoc-Pro), Fmoc-L-tyrosine (Fmoc-Tyr), Fmoc-L-3-nitro-tyrosine (Fmoc-NO_2Y), N_α-(*tert*-butoxycarbonyl)-L-tryptophan (Boc-Trp), N_α-(*tert*-butoxycarbonyl)-L-phenylalanine (Boc-Phe), N_α-(*tert*-butoxycarbonyl)-L-tyrosine (Boc-Tyr), were purchased from NovaBiochem. Tetrakis(triphenylphosphine)palladium ($Pd(PPh_3)_4$) was purchased from Strem. *N,N*-Dimethylformamide (DMF), triethylamine (TEA), dichloromethane (CH_2Cl_2), trifluoroacetic acid (TFA), andhydrous tetrahydrofuran (THF), triisopropylsilanes (TIPS), sodium (Na, metal in hexanes), allyl alcohol, diethyl ether, and hexanes were purchased from Sigma Aldrich. Boc-L-pentafluorophenylalanine (Boc-L-f_5F) was purchased from Peptech (Burlington, MA). Wang-resins loaded with corresponding starting monomer resins were purchased from Applied Biosystems. Fmoc-L-tetrafluorotyrosine (Fmoc-F_4Y) and Boc-L-tetrafluorotyrosine (Boc-F_4Y) were synthesized by following the literature procedure with a

small modification.[35] AcWY[25] and 2,3-F_2Y-OMe[23] were available from a previous study. All chemicals were used as received.

Synthesis. Polyproline model peptides were synthesized by SPPS as described in Scheme 5.2. Each coupling step (i) was repeated 3 times per one monomer unit to ensure a high yield of the targeted peptide. Deprotection of Fmoc group (ii) was also repeated twice and the resins with peptides were washed with DMF and DCM in between the coupling and deprotection steps. Fmoc coupling of proline was very inefficient thus each amino acid extension was repeated 3 times. Some of peptide synthesis used Wang resins with pre-coupled triprolines and with tryptophan or tyrosine terminal (Purchased from Peptide 2.0). After synthesis, the synthesized peptides were cleaved off of the resin by using TFA: TIPS: H_2O= 95%: 2.5%: 2.5% solution. TFA was carefully blown off and the peptides were triturated out of the residual mixture with diethyl ether. The peptide was dried then dissolved in minimal amount of water with acetonitrile as a co-solvent. Polyproline Model peptides are fairly insoluble in water but using co-solvent (methanol/acetonitrile) can dissolve peptides to make dilute aqueous solution for pulse radiolysis experiments.

Scheme 5.2 Solid Phase Peptide Synthesis.

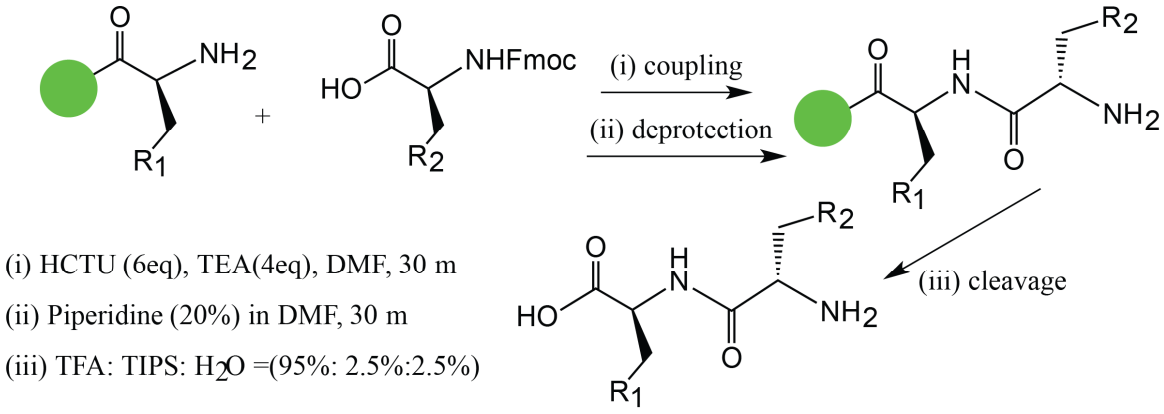

(i) HCTU (6eq), TEA(4eq), DMF, 30 m
(ii) Piperidine (20%) in DMF, 30 m
(iii) TFA: TIPS: H_2O =(95%: 2.5%:2.5%)

Scheme 5.3 Polyproline Peptide models systems and control small molecules for Pulse Radiolysis. For small molecules (amino acid monomer), amino acid -methyl ester (CO_2H protected) or -acetylated (NH_2 protected) was used.

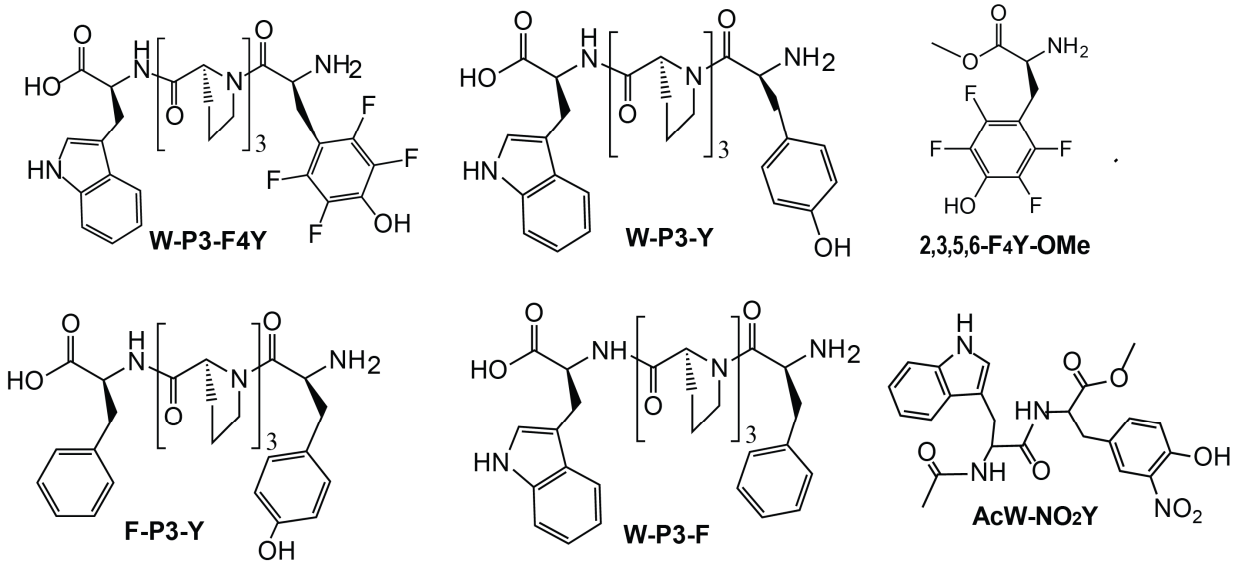

2,3,5,6-F_4Y-OMe: 2,3,5,6-F_4Y-OMe was prepared as published except that F_4Y was prepared as described.[23,24,35]

^{1}H NMR (400 MHz, CD_3OD, 25 °C): δ = 4.22 (m, 1H, Cα-H), 3.72 (s, 3H, OCH_3), 3.16 (m, 2H, Cβ-H).

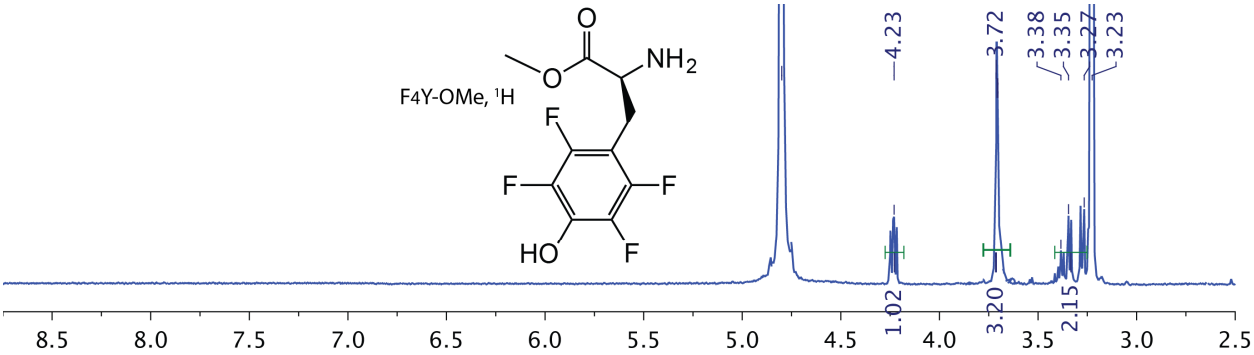

Figure 5.14 ^{1}H NMR of 2,3,4,5-F_4Y-OMe in d$_4$-CD_3OD. Peaks at 3.23 and 4.85 ppm are the solvent (CH_3OH) and water peaks.

^{19}F NMR (400 MHz, D_2O, 25 °C): δ = 155.59 (2F), 172.43 (2F).

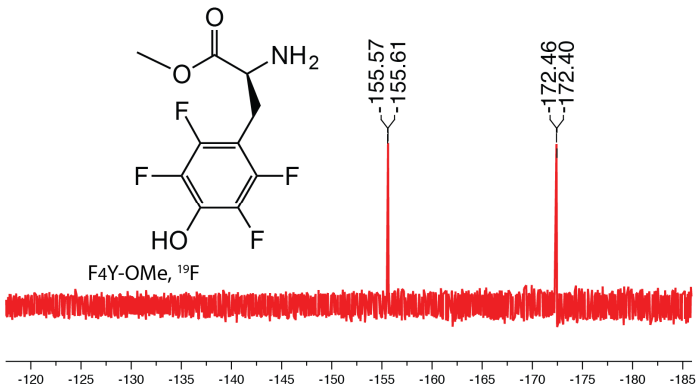

Figure 5.15 ^{19}F NMR of 2,3,4,5-F_4Y-OMe in D_2O.

AcW-NO_2Y was prepared the same way as AcWY[25] except that NO_2Y-OMe were used instead of Y-OMe accordingly.

AcW-NO_2Y ^{1}H NMR (400 MHz, CD_3OD, 25 °C): δ = 8.86 (d, 1H, N-H), 7.87 (d, 1H, indole-H), 7.64 –7.30 (m, 3H, indole-H, NO_2Y), 7.19 – 6.85 (m, 4H, indole-H, NO_2Y), 4.68 (m, 1H, W-CH), 4.24 (m, 1H, NO_2Y-H), 3.54 (s, 3H, OCH_3), 3.05–3.02 (m, 4H, Cβ-H), 1.84 (s, 3H, Ac-CH_3).

Peptide: All polyproline model peptides were purified by HPLC with eluent solution (0.1 % TFA aqueous solution: acetonitrile = 0 –100 %). For the analytical HPLC traces below, the peak at 1.461 is an artifact.

W-P_3-F_4Y ^{19}F NMR (400 MHz, CD_3OD, 25 °C): δ = 145.67 (2F), 158.74 (2F).

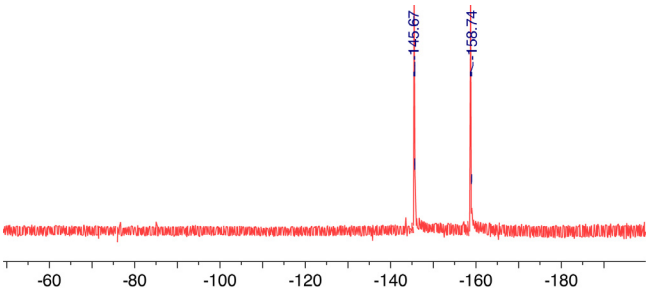

Figure 5.16 ^{19}F NMR spectrum of **W-P_3-F_4Y** in d_3-CD_3OD.

Chemical Formula: $C_{35}H_{38}F_4N_6O_7$ MW: 730.72. ESI-MS found: m/z = 731.2719, ($M+H^+$), z=1.

F isotope pattern Calcd: m/z = 731.28 (100%), 732.28 (37.9%), 733.29 (7.0%), 732.28 (2.2%).

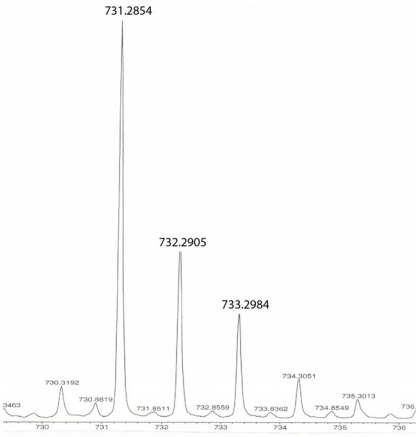

Figure 5.17 W-P_3-F_4Y: ESI-MS

HPLC retention time, t_R: 17.2 m (0.1 % TFA and acetonitrile).

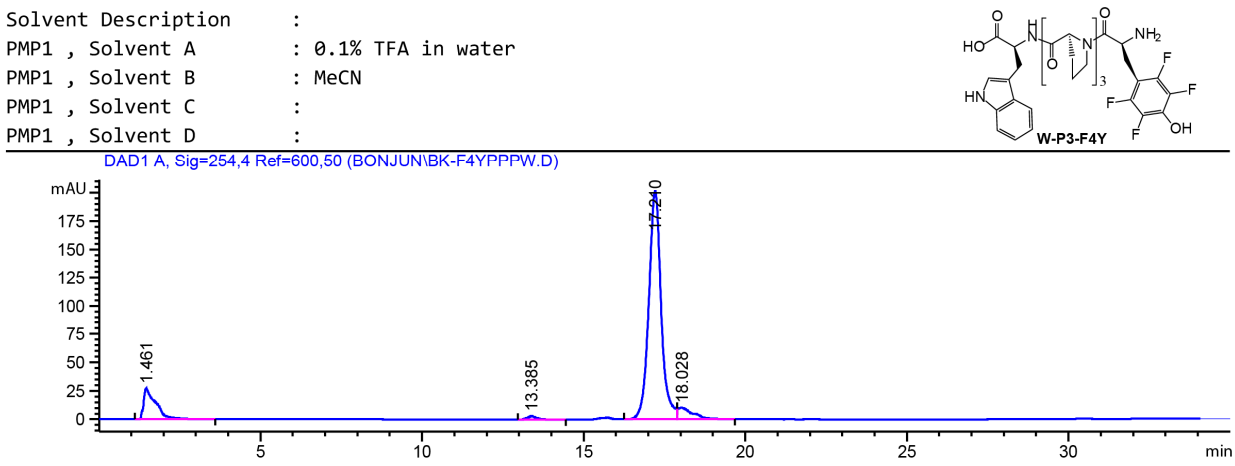

W-P_3-Y Chemical Formula: $C_{35}H_{42}N_6O_7$ MW: 658.31. ESI-MS found: m/z = 659.31 ($M+H^+$).

HPLC retention time, t_R: 16.8 m (0.1 % TFA and acetonitrile).

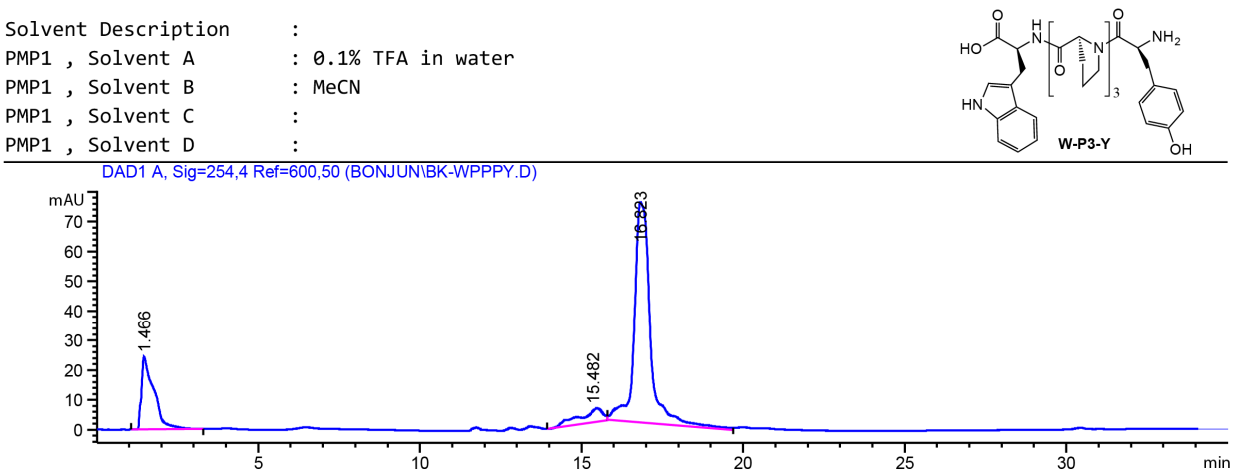

F-P$_3$-Y Chemical Formula: $C_{33}H_{41}N_5O_7$ MW: 619.30. ESI-MS found: m/z = 620.44 ($M+H^+$).

HPLC retention time, t_R: 17.3 m (0.1 % TFA and acetonitrile).

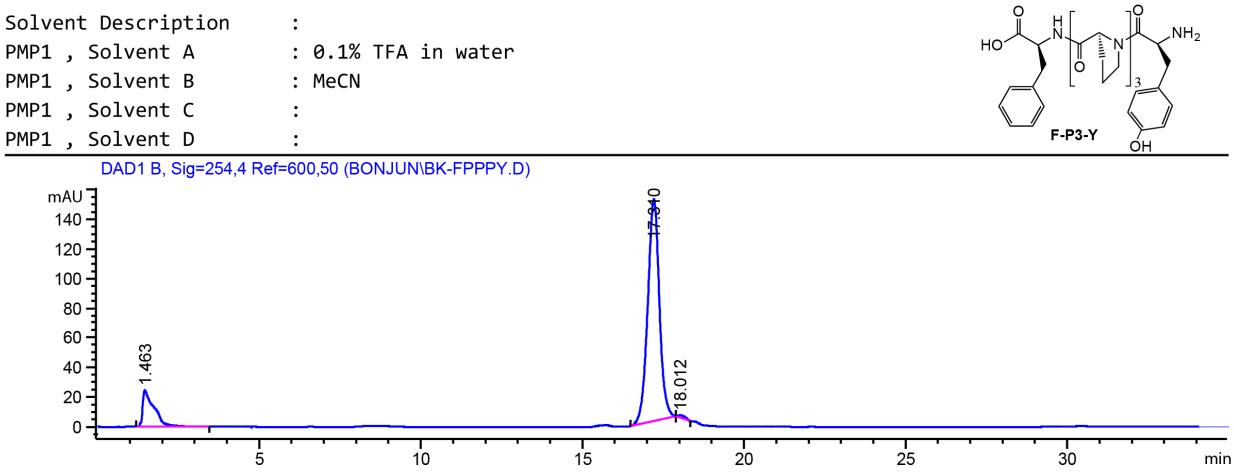

W-P$_3$-F Chemical Formula: $C_{35}H_{42}N_6O_6$ MW: 642.32. ESI-MS found: m/z = 664.52 ($M+Na^+$).

HPLC retention time, t_R: 14.5 m (0.1 % TFA and acetonitrile).

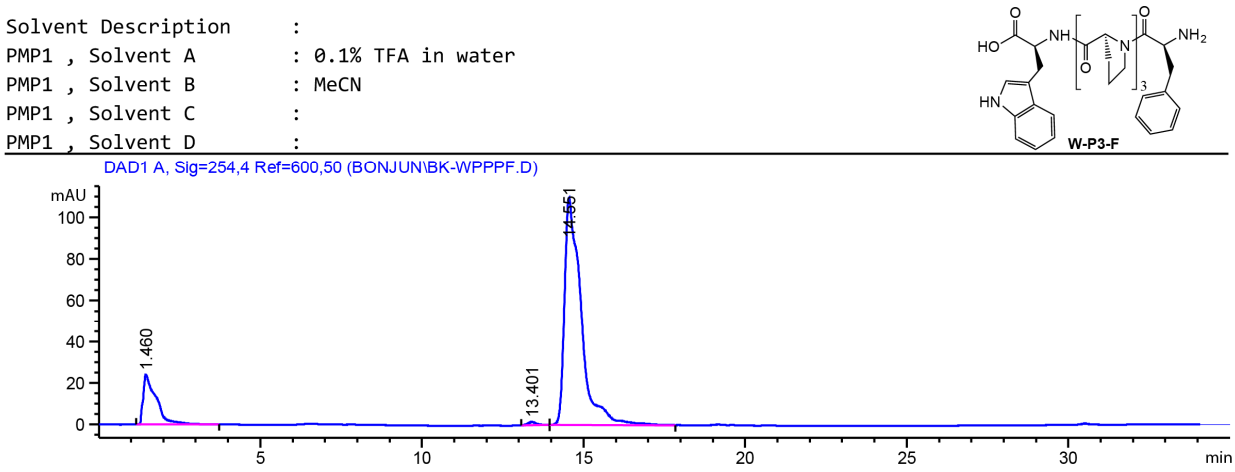

5.5.2. Circular Dichroism Spectra

Circular Dichroism spectra of polyproline peptide models were obtained on an Aviv Model 202 Circular Dichroism Spectrometer at The Biophysical Instrument Facility of MIT CSBi (computational and systems biology). Quarts spectroscopy cell of 1 mm path length was purchased from Hellma Cells.

To confirm the stability of PPII structure, CD spectra were obtained across a range of pH and solvent compositions that would be employed for various physical methods (0, 25, 50, 75, 100 % MeCN with aqueous buffer). CD spectra of all model peptides were obtained in room temperature. The model peptide dissolves to 30 μM to avoid the saturation of CD spectra (A_{280} <1.0).

5.5.3 Pulse Radiolysis

Pulse Radiolysis experiments was performed at The Accelerator Center for Energy Research (ACER), Chemistry Division, Brookhaven National Laboratory. Most experiments were performed on a 2 MeV electron Van de Graaff instrument and a few kinetics measurements were

performed on the picosecond Laser-Electron Accelerator Facility (LEAF). Bon Jun Koo performed Van de Graaff pulse radiolysis experiment under the supervision of Dr. Wishart.

Pulse widths were in the range of 60 – 300 ns. Three passes of analyzing light through a 2 cm cell (quartz, specially designed in-house for sample bubbling and dispensing) were used in the detection optical path. For the kinetics recorded on a time scale of less than 100 μs, the analyzing xenon arc light source was pulsed.[36]

The aqueous solution was prepared with deionized water and recrystallized salts. The solution of pH 7 and pH 12 were prepared with phosphate 50 mM, the solution of pH 9 aqueous with borate 50 mM and the solution of pH 4.5 was acetate 10 mM. For sulfate radical, $NaSO_4$ 2 mM solution was made and for azide radical, NaN_3 0.1 M solution was made with aqueous buffer of the chosen pH. The analyte (polyproline peptide models/ amino acid monomers) were dissolved to 0.1 mM/0.2 mM concentrations except for the concentration dependence study: 0.1 mM ~1 mM for the reaction rate constant measurement for amino acids and 0.1 ~ 2 mM for polypeptide concentration dependence study. All VDG experiments were performed at 25 ± 1 °C in Ar-purged solutions (sulfate/ azide radicals). Dosimetry was performed with N_2O-saturated 10 mM KSCN aqueous solution using $G\epsilon = 4.87 \times 10^4$ ions $(100\ eV)^{-1}M^{-1}cm^{-1}$ for the $(SCN)_2^{\bullet-}$ radical at 472 nm.[37] The rate constants of unnatural amino acids with azide radicals were measured with 0.1 M N_3 solution pH 7 phosphate buffer. The detail of the instrument set up is beyond the scope of this chapter and can be found in ref. 38. Portion of pulse radiolysis data analysis was performed using BNL PRWIN software.[34]

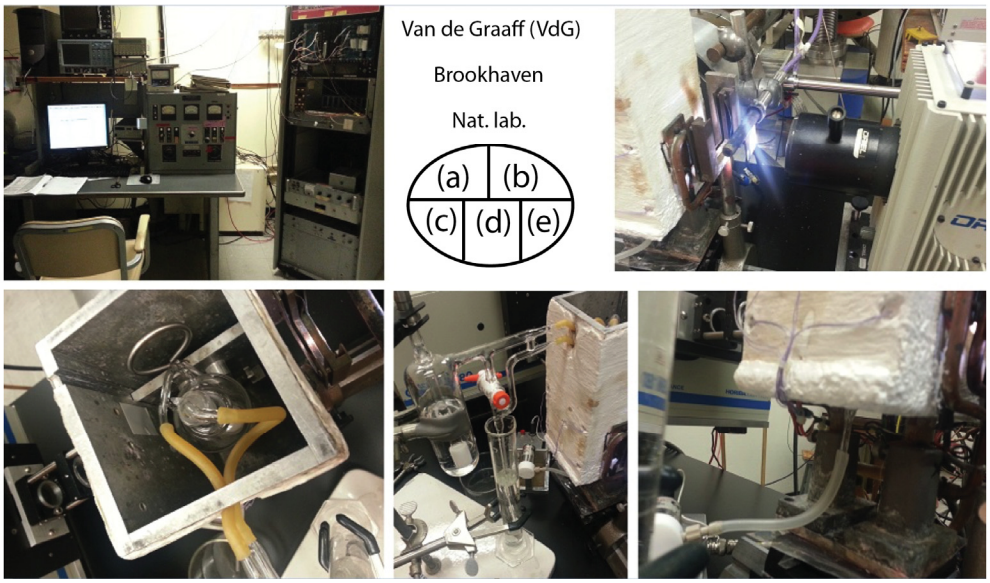

Figure 5.18 Van de Graaff Pulse Radiolysis; a) control vault b) probe lamp c) sample cell holder with thermostat d) bubbler for gas e) sample discharge.

5.6 References

(1) Stubbe, J.; Nocera, D. G.; Yee, C. S.; Chang, M. C. Y. *Chem. Rev.* **2003**, *103*, 2167.

(2) a) Winkler, J. R.; Gray, H. B. *J. Am. Chem. Soc.* **2014**, *136*, 2930. b) Gray, H. B.; Winkler, J. R. *Chem. Phys. Lett.* **2009**, *483*, 1.

(3) a) Durrant, J. R.; Klug, D. R.; Kwa, S. L. S.;Van Grondelle, R.; Porter, G.; Dekker, J. P. *Proc. Natl. Acad. Sci. USA* **1995**, *92*, 4798. b) Voet, D.; Voet, J. G. *Biochemistry*, 2nd ed., John Wiley & Sons, Inc.: New York, NY, **1995**.

(4) a) Li, Y. F.; Heelis, P. F.; Sancar, A. *Biochemistry* **1991**, *30*, 11262. b) Aubert, C.; Vos, N. H.; Eker, A. P. M.; Brettel, K. *Nature* **2000**, *405*, 586. c) Cheung, M. S.; Daizadeh, I.; Stachebrukhov, A. A.; Heelis, P. F. *Biophys. J.* **1999**, *76*, 1241.

(5) a) Gray, H. B.; Winkler, J. R. *Chem. Phys. Lett.* **2009**, *483*, 1. b) Dempsey, J. L.; Winkler, J. R.; Gray, H. B. *Chem. Rev.* **2010**, *110*, 7024.

(6) Genereux, J. C.; Barton, J. K. *Chem. Rev.* **2010**, *110*, 1642.

(7) Minnihan, E. C.; Ando, N.; Brignole, E. J.; Olshansky, L.; Chittuluru, J.; Asturias, F. J.; Drennan, C. L.; Nocera, D. G.; Stubbe, J. *Proc. Natl. Acad. Sci.* **2013**, *110*, 3835.

(8) Minnihan, E. C.; Nocera, D. G.; Stubbe, J. *Acc. Chem. Res.* **2013**, *46*, 2524.

(9) Seyedsayamdost, M. R.; Chan, C. T. Y.; Mugnaini, V.; Stubbe, J.; Bennati, M. *J. Am. Chem. Soc.* **2007**, *129*, 15748.

(10) Nordlund, P.; Eklund, H. *J. Mol. Biol.* **1993**, *232*, 123.

(11) Cordes, M.; Köttgen, A.; Jasper, C.; Jacques, O.; Boudebous, H.; Giese, B. *Angew. Chemie Int. Ed.* **2008**, *47*, 3461.

(12) Giese, B.; Wang, M.; Gao, J.; Stoltz, M.; Müller, P.; Graber, M. *J. Org. Chem.* **2009**, *74*, 3621.

(13) Giese, B.; Eckhardt, S.; Lauz, M.; Gao, J.; Wang, M. *Chim. Int. J. Chem.* **2012**, *66*, 364.

(14) Bobrowski, K.; Poznański, J.; Holcman, J.; Wierzchowski, K. L. *J. Phys. Chem. B* **1999**, *103*, 10316.

(15) Bobrowski, K.; Holcman, J.; Poznanski, J.; Ciurak, M.; Wierzchowski, K. L. *J. Phys. Chem.* **1992**, *96*, 10036.

(16) a) Faraggi, M.; DeFelippis, M. R.; Klapper, M. H. *J. Am. Chem. Soc.* **1989**, *111*, 5141. b) Vassilian, A.; Wishart, J. F.; Van Hemelryck, B.; Schwarz, H.; Isied, S. S. *J. Am. Chem. Soc.* **1990**, *112*, 7278.

(17) Schuler, B.; Lipman, E. A.; Steinbach, P. J.; Kumke, M.; Eaton, W. A. *Proc. Natl. Acad. Sci.* **2005**, *102*, 2754.

(18) Woody, R. W. *J. Am. Chem. Soc.* **2009**, *131*, 8234.

(19) Kakinoki, S.; Hirano, Y.; Oka, M. *Polym. Bull.* **2005**, *53*, 109.

(20) Wilhelm, P.; Lewandowski, B.; Trapp, N.; Wennemers, H. *J. Am. Chem. Soc.* **2014**, *45*, 15629.

(21) Nagel, Y. A.; Kuemin, M.; Wennemers, H. *Chim. Int. J. Chem.* **2011**, *65*, 264.

(22) Minnihan, E. C.; Ando, N.; Brignole, E. J.; Olshansky, L.; Chittuluru, J.; Asturias, F. J.; Drennan, C. L.; Nocera, D. G.; Stubbe, J. *Proc. Natl. Acad. Sci. U. S. A.* **2013**, *110*, 3835.

(23) Seyedsayamdost, M. R.; Reece, S. Y.; Nocera, D. G.; Stubbe, J. *J. Am. Chem. Soc.* **2006**, *128*, 1569.

(24) Reece, S. Y.; Seyedsayamdost, M. R.; Stubbe, J.; Nocera, D. G. *J. Am. Chem. Soc.* **2006**, *128*, 13654.

(25) Reece, S. Y.; Stubbe, J.; Nocera, D. G. *Biochim. Biophys. Acta* **2005**, *1706*, 232.

(26) Reece, S. Y.; Nocera, D. G. *J. Am. Chem. Soc.* **2005**, *127*, 9448.

(27) Reece, S. Y.; Seyedsayamdost, M. R.; Stubbe, J.; Nocera, D. G. *J. Am. Chem. Soc.* **2006**, *128*, 13654.

(28) Rodgers, M. A. J. *Radiation Chemistry: Principles and Applications*; VCH: Weinheim, **1987**.

(29) Stanbury, D. M. *Adv. Inorg. Chem.* **1998**, *33*, 6.

(30) Neta, P.; Huie, R. E.; Ross, A. B. *J. Phys. Chem. Ref. Data* **1988**, *17*, 1027.

(31) a) El-Faham, A.; Albericio, F. *Chem. Rev.* **2011**, *111*, 6557. b) Isidro-Llobet, A.; Alvarez, M.; Albericio, F. *Chem. Rev.* **2009**, *109*, 2455.

(32) Solar, S.; Getoff, N.; Surdhar, P. S.; Armstrong, D. A.; Singh, A. *J. Phys. Chem.* **1991**, *95*, 3639.

(33) Yokoyama, K.; Uhlin, U.; Stubbe, J. *J. Am. Chem. Soc.* **2010**, *132*, 15386.

(34) The PRWIN program was written by Harold Schwarz. The non-linear least squares routines used here are the mrqmin, mrqcof, and gaussf routines from Numerical Recipes Omnibus File, Copyright (C) 1986,1987,1989 by Numerical Recipes Software, P.O. Box 243, Cambridge, MA 02238, U.S.A.

(35) Wang, F.; Qin, L.; Wong, P.; Gao, J. *Org. Lett.* **2011**, *13*, 236.

(36) Funston, A. M.; Lymar, S. V.; Saunders-Price, B.; Czapski, G.; Miller, J. R. *J. Phys. Chem. B* **2007**, *111*, 6895.

(37) Wishart, J. F.; Nocera, D. G. Eds. *In Photochemistry and Radiation Chemistry. Complementary Methods for the Study of Electron Transfer*; American Chemical Scoiety: Washington, DC, **1998**.

(38)Van de Graaff, R. J.; Compton, K. T.; Van Atta, L. C. *Phys. Rev.* **1933**, *43*, 149.